

See discussions, stats, and author profiles for this publication at: <https://www.researchgate.net/publication/277554632>

Microscopes

Chapter · January 2010

CITATIONS

6

READS

24,889

2 authors, including:



[Michael Shribak](#)

Marine Biological Laboratory

151 PUBLICATIONS 1,667 CITATIONS

SEE PROFILE

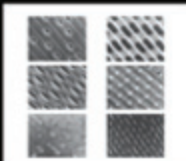
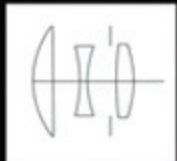
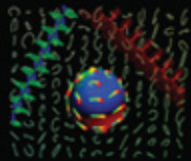
Third Edition

Sponsored by the Optical Society of America

HANDBOOK OF OPTICS

Volume I

*Geometrical and Physical Optics, Polarized Light,
Components and Instruments*



Editor-in-Chief:
Michael Bass

Associate Editors:
Casimer M. DeCusatis
Jay M. Enoch
Vasudevan Lakshminarayanan
Guifang Li
Carolyn MacDonald
Virendra N. Mahajan
Eric Van Stryland

OSA[®]

MICROSCOPES

Rudolf Oldenbourg

*Marine Biological Laboratory
Woods Hole, Massachusetts, and
Physics Department
Brown University
Providence, Rhode Island*

Michael Shribak

*Marine Biological Laboratory
Woods Hole, Massachusetts*

28.1 GLOSSARY

f	focal length
M	magnification
n	refractive index
NA	numerical aperture
z	distance along optical axis
λ	wavelength of light
I	irradiance, sometimes called intensity

28.2 INTRODUCTION

The optical principles and basic lens design needed to generate a diffraction-limited, highly magnified image with the light microscope were already essentially perfected a century ago. Ernst Abbe demonstrated how a minimum of two successive orders of diffracted light had to be captured in order for a particular spacing to be resolved (see historical sketch about Abbe principle¹). Thus, he explained and demonstrated with beautiful experiments the role of the wavelength of the imaging light and the numerical aperture ($\text{NA} = n \sin \Theta$, Fig. 1)² of the objective and condenser lenses on the resolving power of the microscope. In general, the minimum spacing δ for line gratings that can just be resolved cannot be smaller than

$$\delta = \frac{\lambda}{2 \text{NA}} \quad (1)$$

when the NA of the condenser is equal to the NA of the objective.

For generating an image, contrast is just as important as resolution. Much of the early use of the light microscope depended on the relatively high image contrast that could be generated by differential absorption, scattering, reflection, birefringence, and the like due to specimen composition

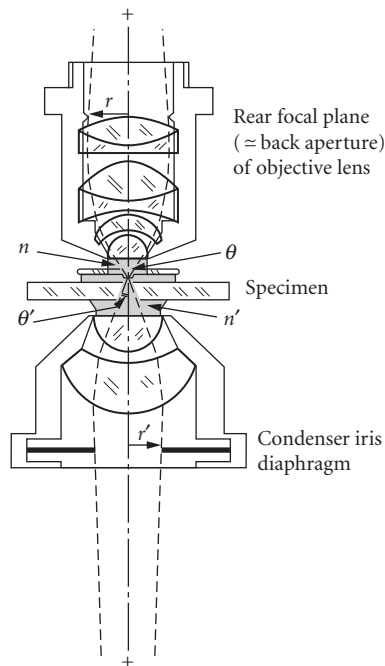


FIGURE 1 Definition of numerical aperture of objective ($NA_{\text{obj}} = n \sin\theta$) and condenser ($NA_{\text{cond}} = n' \sin\theta'$).²

or structure. Specimens, such as unstained living cells and other transparent objects introducing small optical path differences, were generally not amenable to direct microscopic observation for they would not produce detectable image contrast when brought to exact focus.

These impediments were removed by Zernike who showed how contrast in the microscope image is generated by interference between the light waves that make up the direct rays (that are undeviated by the specimen) and those that were scattered and suffered a phase difference by the presence of the specimen. Using this principle, Zernike invented the phase-contrast microscope.³ For the first time it became possible to see, in focus, the image of small, nonabsorbing objects. Zernike's revelations, together with Gabor's further contributions,⁴ not only opened up opportunities for the design of various types of interference-dependent image-forming devices but, even more importantly, improved our understanding of the basic wave optics involved in microscope image formation.

About the same time as Zernike's contributions, perfection of the electron microscope made it possible to image objects down to the nanometer range, albeit necessitating use of a high-vacuum environment and other conditions compatible with electron imaging. Thus, for four decades following World War II, the light microscope in many fields took a back seat to the electron microscope.

During the last decades, however, the light microscope has reemerged as an indispensable, powerful tool for investigating the submicron world in many fields of application. In biology and medicine, appropriate tags, such as fluorescent tags, are used to signal the presence and location of selected molecular species with exceptionally high sensitivity. Dynamic behaviors of objects far below the limit of resolution are visualized by digitally enhanced video microscopy directly in their natural (e.g., aqueous) environment. Very thin optical sections are imaged by video microscopy, and even more effectively with confocal optics. Quantitative measurements are made rapidly with the aid of digital image analysis.

At the same time, computer chips and related information-processing and storage devices, whose availability in part has spurred the new developments in light microscopy, are themselves miniaturized to microscopic dimensions and packaged with increasingly higher density. These electronic and photonic devices in turn call for improved means for mass manufacturing and inspection, both of which require advanced microscope optics.

Driven by the new needs and aided in part by computerized ray tracing and the introduction of new optical materials, we see today another epochal advance in the quality of lens design. The precision and remote control capabilities of mechanical components are also steadily improving. Furthermore, we may expect another surge of progress, hand-in-hand with development of improved electro-optical and electromechanical devices, in regulated image filtration, contrast-generating schemes, as well as in optical manipulation of the specimen employing microscope optics.

There are a number of excellent review articles and books discussing the optical principles of light microscopes^{1,5,6} and microscopic techniques,^{2,7-10} and their applications.¹¹⁻¹⁴ Among the many resources on microscopy available on the Internet, the Molecular Expressions website (<http://www.microscopy.fsu.edu/index.html>) stands out for its comprehensive treatment, beautiful illustrations, and interactive tutorials on the subject.

The present chapter is intended in part to bridge the territories of the manufacturer and the user of the microscope, including those who incorporate microscope optics into other equipment or apply them in unconventional ways. In this revision for the third edition of the *Handbook of Optics*, we reorganized the material, expanded the description of techniques that are typically covered only in passing by recent reviews and books on microscopy (e.g. interference and polarization microscopy), and added brief descriptions of imaging modes that are based on new optical concepts or new approaches to extract quantitative information from traditional imaging modes.

Many of the optical concepts and techniques, which are introduced here in the context of microscopy, are discussed in more detail in other chapters of this *Handbook*. On general optical considerations consult the *Handbook* chapters in this volume, “General Principles of Geometrical Optics” (Chap. 1) and on optical elements, such as “Lenses” (Chap. 17), “Polarizers” (Chap. 13), as well as chapters on physical optics for wave phenomena such as “Interference” (Chap. 2), “Diffraction” (Chap. 3), “Coherence Theory” (Chaps. 5 and 6), and “Polarization” (Chap. 12) which, as phenomena, are essential to the workings of the various contrast modes of the microscope. Material on image detection and processing can be found in *Handbook* chapters on vision in Vol. III, imaging detectors in Vol. II, and optical information and image processing in Chap. 11 of this volume.

28.3 OPTICAL ARRANGEMENTS, LENSES, AND RESOLUTION

Optical Arrangements

Geometric Optical Train, Magnification, Conjugate Planes In the optical train of a compound microscope (Fig. 2) invented by Galileo around 1610, the objective lens L_{ob} projects an inverted, real, magnified image O' of the specimen O (or object plane) into the intermediate image plane (or primary image plane). The intermediate image plane is located at a fixed distance $f' + z'$ behind L_{ob} , where f' is the back focal length of L_{ob} and z' is the optical tube length of the microscope. In general, O' is an aerial image for which an ocular L_{oc} (or the eyepiece) acts as a magnifier in front of the eye. Since L_{oc} , coupled with the corneal surface and lens of the eye, produces an erect image O'' of O on the retina, the object appears inverted to the observer. The ocular may also be used to project the image onto a screen. The aerial image at O' can also be exposed directly onto conventional film or an electronic sensor.

Continuing with the schematic diagram in Fig. 2, using thin-lens approximations, O is placed at a short distance z just outside of the front focal plane of L_{ob} , such that $z + f = a$, where f is the front focal length of L_{ob} and a is the distance between O and L_{ob} . O' is formed at a distance $b = (z' + f')$ behind L_{ob} . For a height y of O , the image height $y' = y \times b/a$. Thus, L_{ob} magnifies O by $M_{ob} = b/a$.

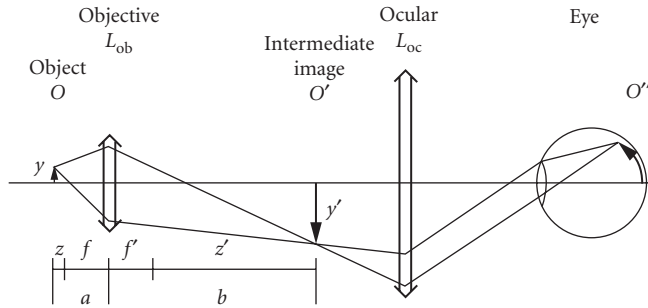


FIGURE 2 Ray path in the microscope from object to observer's eye (see text).

Also, $M_{ob} = f/z = z'/f'$. M_{ob} is the transverse or lateral magnification of L_{ob} . In the case of an infinity-corrected objective (Fig. 3), M_{ob} is the ratio f_{tb}/f , with f_{tb} the focal length of the specific tube lens L_{tb} . In turn, y' is magnified by L_{oc} by a factor $M_{oc} = 25 \text{ cm}/f_{oc}$, where f_{oc} is the focal length of the ocular (in cm) and 25 cm is the so-called near distance from the observer's eye (see Vol. II of this *Handbook*). Thus, the total transverse magnification of the microscope $M_{tot} = M_{ob} \times M_{oc}$.

Note that most microscope objectives are corrected for use only within a narrow range of image distances, and, in case of older style objectives, only in conjunction with specific groups of oculars. M_{ob} , which is the magnification inscribed on the barrel of the objective lens, is defined for its specified tube length (for high-power objectives, $M_{ob} = z'/f$) or, in case of infinity-corrected objectives, when used together with its specified tube lens. These factors, as well as those mentioned under "Microscope Lenses, Aberrations," must be kept in mind when a microscope objective is used as a magnifying lens, or in reverse as a high-numerical-aperture reducing lens, to form a truly diffraction-limited image.

Continuing the optical train back to the light source in a transilluminating microscope, Fig. 4a shows the ray paths and foci of the waves that focus on an on-axis point in the specimen. In Köhler illumination, the distance between the specimen and the condenser are adjusted so that the image of the field diaphragm in the illuminator is superimposed with the focused region of the specimen, and the lamp collector lens is adjusted so that the source image is focused in the plane of the condenser aperture diaphragm. Thus, \bar{O} , O , O' and O'' all lie in image planes that are conjugate with each other.

Tracing the rays emitted from a point in the light source (Fig. 4b), the rays are parallel between the condenser and the objective lenses. This situation arises because in Köhler illumination the light

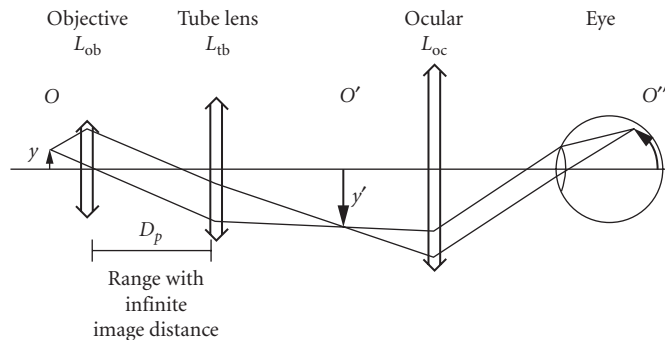


FIGURE 3 Ray path in microscope with infinity-corrected objective and tube lens.

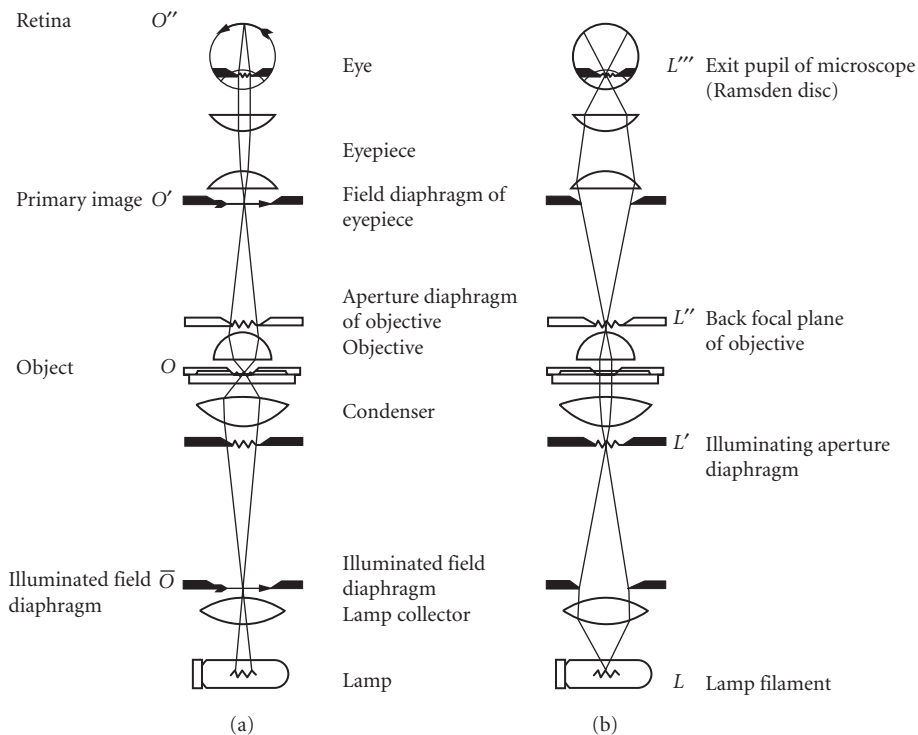


FIGURE 4 Ray paths in a transmitted light microscope adjusted for Köhler illumination. Two sets of conjugate planes are shown: set O in (a) is conjugate with the object O and with the field diaphragm planes; set L in (b) is conjugate with the lamp filament L and with aperture diaphragm planes.¹⁵

source (the filament of an incandescent bulb or the bright arc of a discharge lamp) is projected into the front focal plane of the condenser. Also, since the pupil of an (experienced) observer's eye is placed at the eyepoint or back focal plane of the ocular, the four aperture planes L , L' , L'' , and L''' are again conjugate to each other.

As inspection of Fig. 4a and b¹⁵ shows, the field planes and aperture planes are in reciprocal space relative to each other throughout the whole optical system. This reciprocal relationship explains how the various diaphragms and stops affect the cone angles, paths, and obliquity of the illuminating and image-forming rays, and the brightness, uniformity, and size of the microscope field. More fundamentally, a thorough grasp of these reciprocal relationships is needed to understand the wave optics of microscope image formation and for designing various contrast-generating devices and other microscope optical systems.

Transillumination The full impact of the illumination system on the final quality of the microscope image is often not appreciated by the microscope user or designer. Undoubtedly, part of this neglect arises from a lack of understanding of the roles played by these components, in particular the condenser, and the common practice of closing down the condenser iris diaphragm to adjust image contrast for comfortable viewing. Regardless of the conventional view, critical examination of the microscope image or point spread function reveals the importance of the alignment, focus, tilt, NA, and effective aperture function of the condenser. The effects are especially noticeable when contrast is enhanced, e.g., by video microscopy. A further illustration of the importance of the illumination on the resolving power of the light microscope can be found in the section on "Structured Illumination."

Ernst Abbe was the first to systematically analyze the resolving power of microscope optics by fabricating precision line gratings and imaging them in the microscope. As indicated earlier, a grating is resolved if the objective lens captures at least two successive diffraction orders which are typically the zero- and first-order diffraction. Abbe summarized his results in a simple expression, relating the minimum resolvable pitch δ to the numerical aperture of the objective and condenser lens:

$$\delta = \frac{\lambda}{\text{NA}_{\text{obj}} + \text{NA}_{\text{cond}}} \quad (2)$$

with λ the wavelength of light used. This formula can be derived by considering the diffraction of linear gratings that are illuminated obliquely. In the limiting case of zero condenser NA, the grating is illuminated coherently by a collimated beam of light that is parallel to the microscope's optical axis. The minimum resolvable pitch is proportional to the wavelength and inversely proportional to the objective NA. By increasing the condenser NA, oblique rays are added to the illuminating light, increasing the angular span between diffraction orders captured by the same objective lens, and thus decreasing the minimum resolvable pitch. By making the condenser and objective NA equal, the grating is effectively illuminated incoherently and Eq. (2) reduces to Eq. (1).

The influence of the condenser NA on resolving two nearby point objects was considered by Hopkins and Barham.¹⁶ They applied the Rayleigh criterion for resolving two pinholes that are equally bright and illuminated incoherently ($\text{NA}_{\text{cond}} = \text{NA}_{\text{obj}}$) and found a minimally resolved distance $d = 0.61\lambda/\text{NA}_{\text{obj}}$ (Fig. 5, $m = 1$).¹⁷ Distance d is a factor 1.22 larger than the limiting pitch of a grating illuminated and imaged by the same condenser and objective lens [Eq. (1)]. However, for the case of coherent illumination ($\text{NA}_{\text{cond}} = 0$), the minimal distance of two resolved points only increases by 40 percent instead of 100 percent, as is the case for gratings. Hopkins and Barham calculated a maximum resolution (minimal d) for $\text{NA}_{\text{cond}} = 1.5 \times \text{NA}_{\text{obj}}$. Such high NA_{cond} is usually not achievable for high-NA objective lenses, and, in addition, with most objectives, flare due to internal reflection would reduce image contrast to an extent possibly unsalvageable even with video contrast enhancement. Again, reduction of NA_{cond} , generally achieved by closing down the condenser iris diaphragm, tends

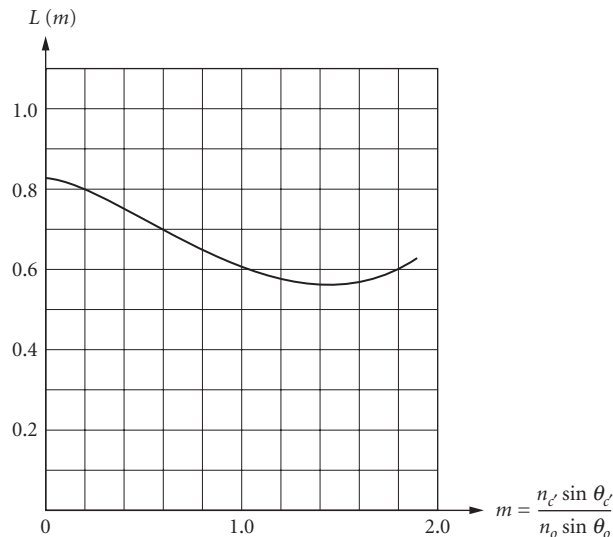


FIGURE 5 Effect of the condenser aperture on the resolution of two pinholes of equal brightness. m is the ratio of the numerical apertures of condenser to objective. L is the minimum resolved distance between the pinholes (Rayleigh criterion) in units of the wavelength divided by the objective aperture.¹⁷

to raise image contrast so that even experienced microscopists tend to use an $NA_{\text{cond}} \approx (0.3, \dots, 0.5) \times NA_{\text{obj}}$ to obtain a compromise between resolution and visibility. With video and other modes of electronic enhancement, the loss of contrast can be reversed so that improved lateral, and especially axial, resolution is achieved by using an NA_{cond} that equals, or nearly equals, the NA_{obj} .

Under optimum circumstances, the light source and condenser should be focused for Köhler illumination (Fig. 4) to minimize flare and to improve the homogeneity of field illumination. Alternately, image brightness, especially in the middle of the field, can be maximized by *critical illumination* where the condenser is somewhat defocused from Köhler illumination to produce an image of the source rather than the field diaphragm superimposed on the specimen. Either mode of illumination can yield resolution approximately as given by Eq. (2).

The aperture function of the microscope can become nonuniform, or limited, for a number of reasons. These include misalignment between the objective and condenser lenses; misalignment of the condenser iris (relative to the condenser lens elements); misalignment of the illuminator and condenser axes; tilted objective or condenser lenses or lens elements; nonuniform illumination of the condenser aperture; limited source size; nonuniform intensity distribution in the source; and improper choice, or focusing, of the condenser or source collector. Whether intentional or accidental, these conditions can reduce the effective NA_{cond} and/or induce oblique illumination, thus sacrificing resolution and image quality. An improvement, using a single optical fiber light scrambler, which allows the filling of the full condenser aperture with uniform illumination and little loss of field brightness (especially when using concentrated arc lamps) was introduced by Ellis¹⁸ (also see Figs. 3-13, 3-14 in Ref. 2).

Epi-Illumination In the epi-illumination mode, a beam splitter, part-aperture-filling mirror, or wavelength-discriminating dichromatic (unfortunately often called dichroic) mirror, placed behind the objective lens diverts the illuminating beam (originating from a light source placed in the side arm of the microscope) into the objective lens, which also acts as the condenser (Fig. 6).¹⁹ Alternatively, a second set of lenses and a beam-diverting mirror (both of whose centers are bored out and are arranged coaxially around the objective lens) can provide a larger NA-illuminating beam, much as in dark field illumination in the transillumination mode.

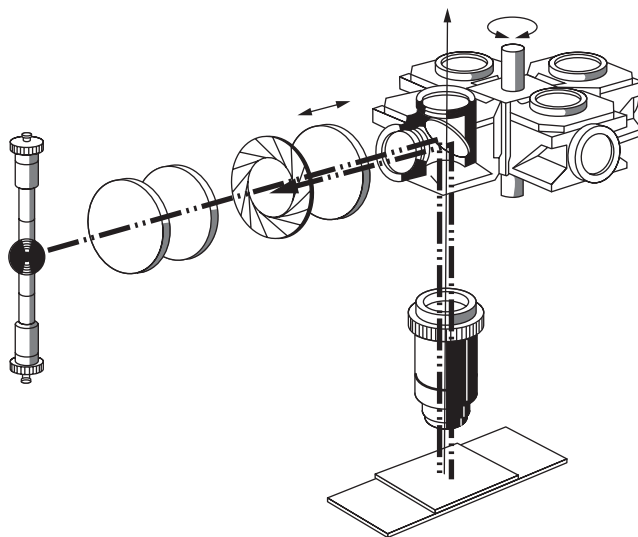


FIGURE 6 Schematic of epi-illuminating light path. The rotatable set of filter cubes with excitation filters, dichromatic mirrors, and barrier filters matched to specific fluorochromes are used in epifluorescence microscopy.¹⁹

This latter approach limits the maximum NA of the objective lens to around 1.25, but has the advantage that the illuminating beam traverses a path completely isolated from the image-forming beam. When the two beams do pass through the same objective lens, as is the case with most epi-illuminating systems, the lens elements must be carefully designed (by appropriate choice of curvature and use of highly efficient antireflection coating) to reduce hot spots and flare introduced by (multiple) reflection at the lens surfaces. Modern microscope objectives for metallurgical and industrial epi-illuminating systems in particular are designed to meet these qualities. In addition, circular polarizers (linear polarizer plus $\lambda/4$ wave plate) and appropriate stops are used to further exclude light reflected from the surfaces of lens elements, cover glass, and the like. For epi-illumination fluorescence microscopy, dichromatic beam splitters, and barrier filters can reduce background contamination that arises from the exciting beam to less than one part in 10^4 .

Orthoscopic versus Conoscopic Imaging The common mode of observation through a microscope is by orthoscopic observation of the focused image. For certain specific applications, particularly with polarizing microscopes, examination of the aperture plane, or conoscopic observation, sheds valuable complementary information.

Conoscopic observation can be made either by replacing the regular ocular with a telescope that brings the aperture plane into focus or by inserting a Bertrand lens (that serves as a telescope objective) in front of a regular ocular. Conversely, one can observe the aperture plane simply by removing the ocular and looking down the microscope body tube (in the absence of a Bertrand lens) or by examining the Ramsden disk above the ocular with a magnifier. Levoy and Oldenbourg used a microlens array for generating a hybrid image that consists of an array of small conoscopic images, each sampling a different object area.^{20,21}

The polar coordinates of each point in the aperture plane, that is the radius r and azimuth angle α are related to the rays traversing the specimen by: $r = \sin \theta$ and $\alpha =$ azimuth orientation of the ray projected onto the aperture plane (Fig. 7). Thus, conoscopic observation provides a plane projection of all of the rays traversing the specimen in three-dimensional space. For specimens, such as single crystal flakes or polished mineral sections in which a single crystal is illuminated (optically isolated)

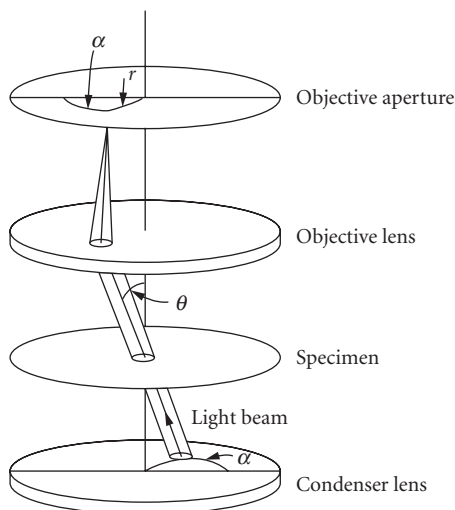


FIGURE 7 Parallel rays with inclination θ and azimuth orientation α traversing the specimen plane, and focused by the objective lens at a point with radius r and same azimuth angle α in the aperture plane.

by closing down the field diaphragm, the conoscopic image reveals whether the crystal is uniaxial or biaxial, its optic axis angle and directions, as well as sign and strength of birefringence and other anisotropic or optically active properties of the crystal.²²

Conoscopic observation also reveals several attributes of the condenser aperture plane and its conjugate planes (e.g., in Köhler illumination, the plane of the condenser iris diaphragm and the illuminating source). Thus, conoscopic observation can be used for checking the size, homogeneity, and alignment of the illuminating light source as well as the size and alignment of the condenser iris diaphragm and phase-contrast annulus (located at the front focal plane of the condenser) relative to the objective exit pupil or the phase ring (located at the back focal plane of the objective). It also reveals the state of extinction in polarized light and interference-contrast microscopy and provides a visual estimate of the aperture transfer function for the particular optical components and settings that are used.

The aperture plane of the microscope is also the Fourier plane of the image, so that diffraction introduced by periodic textures in the specimen can be visualized in the aperture plane by conoscopic observation. Depending on the NA of the objective and the spatial period in the specimen, the pattern of diffraction up to many higher orders can be visualized in the aperture plane when the condenser iris is closed down to illuminate the specimen with a parallel beam of light. Closing down the condenser iris restricts the zero-order light to a small area in the aperture plane and higher-order diffraction maxima produce additional images of the diaphragm displaced in the directions of the periodic texture in the specimen.

Microscope Lenses, Aberrations

Objective Lenses With few exceptions, microscope objective lenses are designed to form a diffraction-limited image in a specific image plane that is located at a fixed distance from the objective lens (or from the tube lens in the case of an infinity-focus system). The field of view is often quite limited, and the front element of the objective is placed close to the specimen with which it must lie in optical contact through a medium of defined refractive index n , usually air ($n = 1$, dry objectives), water ($n = 1.33$, water immersion objectives), oil ($n = 1.52$, oil immersion objectives) or other high refractive index media.

Depending on the degree of correction, objectives are generally classified into achromats, fluorites, and apochromats with a plan designation added to lenses with low curvature of field and distortion (Table 1). Some of these characteristics are inscribed on the objective lens barrel, such as Plan Apo 60/1.40 oil 160/0.17, meaning 60 power/1.40 NA Plan Apochromatic objective lens designed to be used with oil immersion between the objective front element and the specimen, covered by a 0.17-mm-thick coverslip, and used at a 160-mm mechanical tube length. Another example might be Epiplan-Neofluar 50 \times /0.85 ∞ /0, which translates to Plan “Fluorite” objective designed for epi-illumination (i.e., surface illumination of specimen through the objective lens rather than through a separate condenser) with a 50 \times magnification and 0.85 NA to be used in air (i.e., without added immersion medium between the objective front element and coverslip or specimen), with no coverslip, and an (optical) tube length of infinity. “Infinity-corrected” objectives require the use of

TABLE 1 Objective Lens Types and Corrections

Type	Spherical	Chromatic	Flatness
Achromat	*	2λ	No
F-achromat	*	2λ	Improved
Neofluar	3λ	$< 3\lambda$	No
Plan-neofluar	3λ	$< 3\lambda$	Yes
Plan apochromat	4λ	$> 4\lambda$	Yes

* = corrected for two wavelengths at two specific aperture angles.

2λ = corrected for blue and red (broad range of visible spectrum).

3λ = corrected for blue, green, and red (full range of visible spectrum).

4λ = corrected for dark blue, blue, green, and red.

Source: Zeiss publication #41-9048/83.

TABLE 2 Common Abbreviations Designating Objective Lens Types

DIC, NIC	Differential (Nomarski) interference contrast
L, LL, LD, LWD, ELWD, ULWD	Long working distance (extra-) (ultra-)
FL, FLUOR, NEOFLUOR, FLUOTAR	With corrections as with "fluorite" objectives but no longer implies the inclusion of fluorite elements
PHASE, PHACO, PC, PH 1, 2, 3, etc.	Phase contrast, using phase condenser annulus 1, 2, 3, etc.
DL, DM, PLL, PL, PM, PH, NL, NM, NH	Phase contrast: dark low, dark medium, positive low low, low, medium, high contrast (regions with higher refractive index appear darker); negative low, medium, high contrast (regions with higher refractive index appear lighter)
PL, PLAN; EF	Flat field; extended field (larger field of view but not as high as with PLAN, achromats unless otherwise designated)
PLAN APO	Flat field apochromat
NPL	Normal field of view plan
P, PO, POL	Low birefringence, for polarized light
UV	UV transmitting (down to approx. 340 nm), for UV-excited epifluorescence
ULTRAFLUAR	Fluorite objective for imaging down to approx. 250 nm in UV as well as in the visible range
CORR, W/CORR	With correction collar
I, IRIS, W/IRIS	Adjustable NA, with iris diaphragm built into back focal plane
M	Metallographic
NC, NCG	No coverslip
EPI	Surface illumination (specimen illuminated through objective lens), as contrasted to dia- or transillumination
BD, HD	For use in bright or darkfield (hell, dunkel)
CF	Chrome-free (Nikon: objective independently corrected longitudinal chromatic aberrations at specified tube length)
ICS	Infinity color-corrected system (Carl Zeiss: objective lens designed for infinity focus with lateral and longitudinal chromatic aberrations corrected in conjunction with a specified tube lens)
OIL, HI, H; WATER, W; GLY	Oil immersion, Homogeneous immersion, water immersion, glycerol immersion
U, UT	Designed to be used with universal stage (magnification/NA applies for use with glass hemisphere; divide both values by 1.51 when hemisphere is not used)
DI; MI; TI Michelson	Interferometry: noncontact; multiple-beam (Tollanski)
ICT; ICR	Interference contrast: in transillumination; in reflected light

a designated tube lens to eliminate residual aberrations and to bring the rays to focus into the image plane. Several other codes are inscribed or color-coded on microscope objectives (Tables 2 and 3).

Older style objective lenses are designed to be used with a specified group of oculars or tube lenses that are placed at specific distances in order to remove residual errors. For example, compensation oculars were used in conjunction with apochromatic and other high-NA objectives to eliminate lateral chromatic aberration and improve flatness of field. However, modern style objectives together with their tube lenses are typically fully corrected so as not to require additional chromatic or other type corrections.

Coverslip Correction For objective lenses with large NAs, the optical properties and thicknesses of the media lying between its front element and the specimen critically affect the calculations

TABLE 3 Color-Coded Rings on Microscope Objectives

Color code (narrow colored ring located near the specimen end of objective)	
Black	Oil immersion
Orange	Glycerol immersion
White	Water immersion
Red	Special
Magnification color code (narrow band located further away from specimen than immersion code)	
Color	Magnification
Black	1, 1.25, 1.5
Brown	2, 2.5
Red	4, 5
Yellow	10
Green	16, 20
Turquoise blue	25, 32
Light blue	40, 50
Cobalt (dark) blue	60, 63
White (cream)	100 and higher

needed to satisfy the aplanatic and sine conditions and otherwise to correct for image aberrations. For homogeneous immersion objectives (that are designed to be used with the refractive indices and dispersion of the immersion oil, coverslip, and medium imbibing the specimen, all matched to that of the objective lens front element), the calculation is straightforward since all the media can be considered an extension of the front lens element.

However, with nonimmersion objectives, the cover glass can become a source of chromatic aberration, which is worse the larger the dispersion and the greater the thickness of the cover glass. The spherical aberration is also proportional to the thickness of the cover glass. In designing objectives not to be used with homogeneous immersion, one assumes the presence of a standard cover glass and other specific optical media between the front lens element and the specimen. As one departs from these designated conditions, spherical aberration (and also coma) increases with the NA of the lens, since the difference between the tangent and sine of the angle of incidence is responsible for departure from the needed sine condition.

It should also be noted that oil immersion objectives fail to provide full correction, or full NA, when the specimen is mounted in an imbibing medium with a different refractive index, for example aqueous media, even with the objective and cover glass properly oil-contacted to each other. With such an arrangement, the diffraction image can degrade noticeably as one focuses into the specimen by as little as a few micrometers.²³ Special water immersion objectives (e.g., Nikon Plan Apo 60×/1.2 NA and short-wavelength transmitting Fluor 40×/1.0 NA, both with collar to correct coverslip thickness deviation from 0.17 mm) overcome such aberrations, even when the specimen is imaged through an aqueous medium of 200- μm thickness.

For lenses that are designed to be used with a standard coverslip of 0.17-mm thickness (and $n_D = 1.515$), departure from standard thickness is not overly critical for objectives with NA of 0.4 or less. However, for high-NA, nonhomogeneous immersion lenses, the problem becomes especially critical so that even a few micrometers' departure of the cover glass thickness degrades the image with *high-dry objectives* (i.e., nonimmersion objectives with high NA) of NA above 0.8 (Fig. 8).²⁴ To compensate for such error, well-corrected, high-dry objectives are equipped with correction collars that adjust the spacing of their intermediate lens elements according to the thickness of the cover glass. Likewise, objective lenses that are made to be viewed through layers of silicon or plastic, or of different immersion media (e.g., water/glycerol/oil immersion lenses), are equipped with correction collars.

The use of objective lenses with correction collars does, however, demand that the observer is experienced and alert enough to reset the collar using appropriate image criteria. Also, the focus tends to shift, and the image may wander, during adjustment of the correction collar. Figure 9 shows an

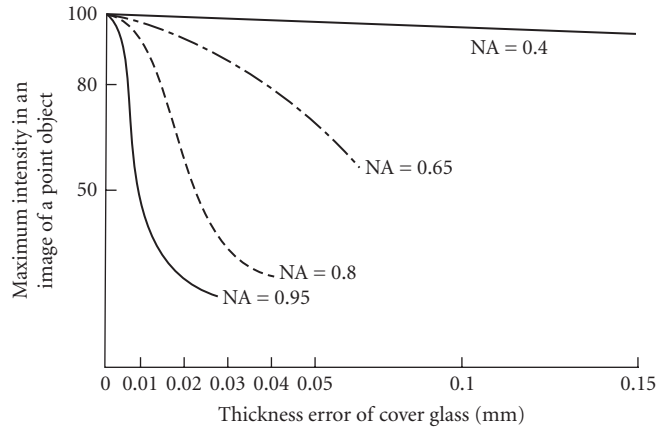


FIGURE 8 Calculated maximum intensity in the image of a point object versus the deviation of the coverglass thickness from the ideal thickness.²⁴

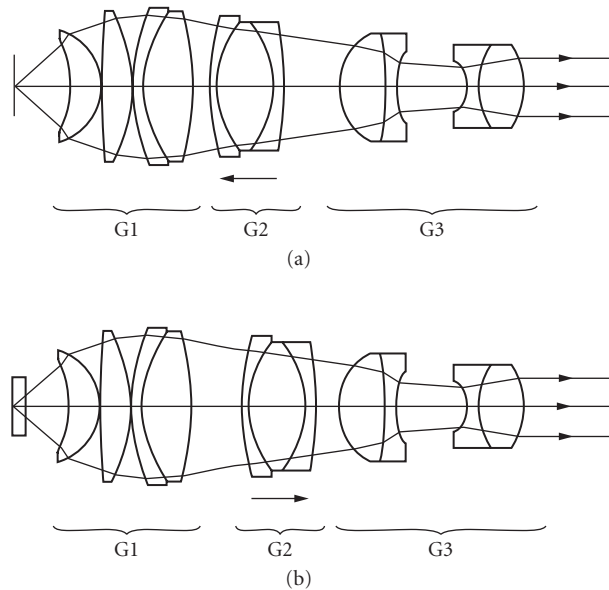


FIGURE 9 High-dry objective lens ($60\times/0.7$ NA) equipped with a correction collar for (a) focusing at the surface or (b) through plane glass of up to 1.5-mm thickness. The lens group G_2 is moved forward to enhance the spherical and chromatic correction by G_1 and G_2 when focused on the surface, while it is moving backward to compensate for the presence of the glass layer when focusing deeper through the glass.²⁴ (U.S. Patent 4666256.)

TABLE 4 Reference Focal Lengths for Infinity-Focused Objective Lenses

Leica	200 mm	B, M
Olympus	180 mm	B, M
Carl Zeiss	164.5 mm	B, M
Nikon	200 mm	B, M

B = biological, M = metallurgical.

example of a 60/0.7 objective lens equipped with a correction collar for focusing at the surface or through a cover glass of up to 1.5-mm thickness without altering the focal setting of the lens.

Tube Lengths and Tube Lenses for Which Microscope Objectives Are Corrected For finite-focused “biological” objective lenses, most manufacturers had standardized the mechanical tube length to 160 mm. More recently most manufacturers have switched to infinity focus for their biomedical and metallurgical microscopes.

For infinity-focused objective lenses, the rays emanating from a given object point are parallel between the objective and tube lens. Since the physical distance (D_p , Fig. 3) and optical path length between the objective and tube lens are not critical, optical plane-parallel components, such as compensators, analyzers, and beam splitters, can be inserted in this space without altering the objective’s corrections. The tube lens focuses the parallel rays onto the intermediate image plane.

The magnification of an infinity-focused objective lens is calculated by dividing the focal length of the tube lens (also called reference focal length) by the focal length of the objective lens. The reference focal lengths adopted by several manufacturers are listed in Table 4.

Working Distance Microscope objectives are generally designed with a short free working distance, that is the distance from the front element of the objective lens to the surface of the cover glass or, in the case of lenses that are designed to be used without cover glass, to the specimen surface. For some applications, however, a long free working distance is indispensable, and special objectives are designed for such use despite the difficulty involved in achieving large numerical apertures and the needed degree of correction.

Field Size, Distortion The diameter of the field in a microscope is expressed by the field-of-view number, or simply field number, which is the diameter of the field in millimeters measured in the intermediate image plane. The field size in the object plane is obviously the field number divided by the magnification of the objective. While the field number is often limited by the magnification and field stop of the ocular, there is clearly a limit that is also imposed by the design of the objective lens. In early microscope objectives, the maximum usable field diameter tended to be about 18 mm or considerably less, but with modern plan apochromats and other special flat field objectives, the maximum usable field can be as large as 28 mm or more. The maximum useful field number of objective lenses, while available from the manufacturers, is unfortunately not commonly listed in microscope catalogs. Acknowledging that these figures depend on proper combination with specific tube lenses and oculars, we should encourage listing of such data together with, for example, UV transmission characteristics (e.g., as the wavelength at which the transmission drops to 50 percent, or some other agreed upon fraction).

Design of Modern Microscope Objectives Unlike earlier objective lenses in which the reduction of secondary chromatic aberration or curvature of field were not stressed, modern microscope objectives that do correct for these errors over a wide field tend to be very complex. Here we shall examine two examples, the first a 60/1.40 Plan Apochromat oil-immersion lens from Nikon (Fig. 10).²⁴

Starting with the hyperhemisphere at the front end (left side of Fig. 10) of the objective, this aplanatic element is designed to fulfill Abbe’s sine condition in order to minimize off-axis spherical aberration and coma, while providing approximately half the total magnifying power of the objective (Fig. 11). In earlier designs, the hyperhemisphere has been made with as small a radius

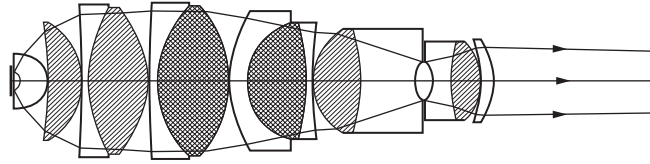


FIGURE 10 Design of Nikon Plan Apochromat oil-immersion objective with 60 \times magnification and 1.40 NA.²⁴

as possible in order to maximize its magnifying power and to minimize its spherical and chromatic aberrations, since these aberrations increase proportionally with the focal length of the lens. Modern demands for larger field size and reduced curvature of field, however, introduce a conflicting requirement, namely, the need to maintain as large a radius as practical in order to minimize the hyperhemisphere's contribution to the Petzval sum (the algebraic sum of the positive and negative curvatures multiplied by the refractive indices of the lens elements).²⁵ The hyperhemisphere in these Plan Apochromats is made with a high-index, low-dispersion material to compensate for the greater radius. Additionally, a negative meniscus is generated in the front surface of the hyperhemisphere to which is cemented a minute, plano-convex lens. The negative curvature in the hyperhemisphere contributes to the reduction of the Petzval sum. At the same time the minute plano-convex lens protects the material of the hyperhemisphere which is less resistant to weathering. Index matching between the minute plano-convex lens and immersion oil eliminates or minimizes the refraction and reflection at the lens-oil interface and provides maximum transmission of the all-important high-NA rays into the objective lens. The index matching also reduces the influence of manufacturing errors of this minute lens element on the performance of the objective.

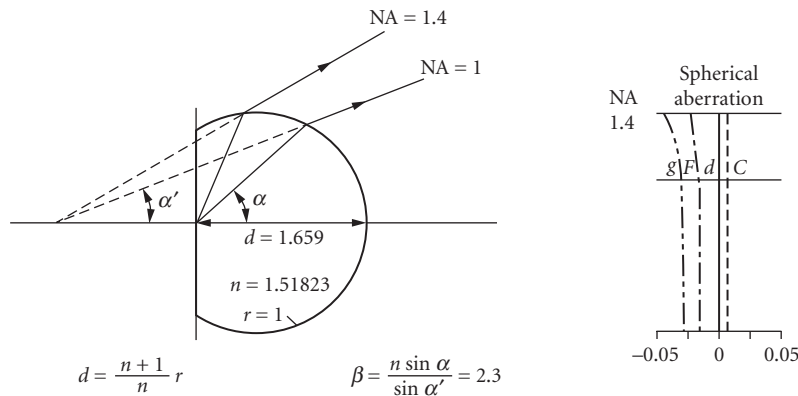


FIGURE 11 Aplanatic condition of the hyperhemisphere placed at the front end of an oil-immersion objective. The front lens has the same refractive index as the coverglass and immersion oil. The aplanatic condition describes the necessary relationship between refractive index n , distance d between object and spherical surface, and radius r of the spherical surface, in order to make all rays emanating from an object point on the axis leave the hemispherical surface after refraction without introducing spherical aberration. According to the sine condition, the magnification β has to be constant for all angles α . On the right, the small amount of longitudinal spherical aberration and chromatic deviation due to dispersion from the ideal focus point of the hyperhemisphere is shown for different wavelengths ($\lambda_C = 656$ nm, $\lambda_d = 588$ nm, $\lambda_F = 486$ nm, $\lambda_g = 436$ nm). Abscissa: longitudinal deviation on lens axis. Ordinate: numerical aperture from 0 (lens axis) to 1.4 NA.²⁴

The low-dispersion-glass singlet behind the aplanatic hyperhemisphere further reduces the cone angle of the rays entering the doublets that follow, allowing these and the subsequent lenses to concentrate on correcting axial and lateral chromatic aberration as well as curvature of field. These errors, as well as residual spherical aberrations, are corrected by inclusion of low-dispersion positive and high-dispersion negative lens elements, use of thick-lens elements, appropriate placement of positive and negative lens curvatures, and through extensive ray tracing. Near the exit pupil, the height of the ray paths through the concave surfaces is reduced in order to generate additional negative values that minimize the Petzval sum (to complement the inadequate negative contribution made by the concave surface in the hyperhemisphere), so that field flatness can be improved without overly reducing the objective lens' magnifying power or adding to its spherical aberration.

In reality, the Petzval sum of the objective as a whole is made somewhat negative in order to compensate for the inevitable positive Petzval sum contributed by the ocular. Thus, the image at the intermediate image surface, especially the sagittal surface of modern objectives, bows away from the object. Unless the image area is relatively small, one needs to use specified oculars in order to attain maximum field flatness combined with optimum correction otherwise.

Unlike earlier objective lenses whose design did not appreciably vary from one manufacturer to another, the design of lenses in modern microscope objectives can vary considerably. For example, compare the Nikon Chrome Free 60/1.4 Plan Apo objective discussed above and the Zeiss Infinity Color-Corrected Systems 63/1.4 Plan Apo objective in Fig. 12. Both are excellent, state-of-the-art lenses. But in addition to general design philosophy, including the decision to avoid or to use tube lenses to achieve full chromatic corrections, other factors such as choice of optical elements with special dispersion characteristics; degrees of UV transmission; freedom from fluorescence, birefringence, aging loss of transmittance, and the like all affect the arrangement of choice.

While a modern research-grade microscope is corrected to keep the aberrations from spreading the image of a point source beyond the Airy disk, geometrical distortion of the image formed by microscope objectives tends not to be as well-corrected (e.g., compared to photographic objectives at the same picture angle). Thus, in objectives for biological use, pincushion distortions of up to 1 percent may be present. However, in objectives that are designed for imaging semiconductors, the distortion may be as low as 0.1 percent and they can be considered nearly distortion-free. To reduce stray light and flare, modern microscope objectives contain lens elements with carefully tuned, antireflection coatings, and lens curvatures are selected to minimize ghost images arising from multiple reflections.

Given the sophisticated design to provide a wide flat field, with spherical aberrations corrected over a broad wavelength range, and with low longitudinal as well as chromatic aberrations corrected at high NA, the aberration curves of these modern microscope objectives no longer remain simple cubic curves, but turn into complex combinations of higher-order curves (Fig. 13).

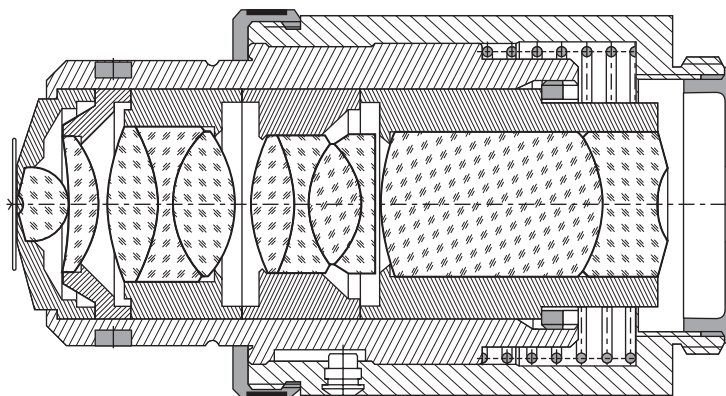


FIGURE 12 Carl Zeiss Infinity Color-Corrected 63/1.4 Plan Apo objective. (Courtesy of E. Keller, Carl Zeiss, N.Y.)

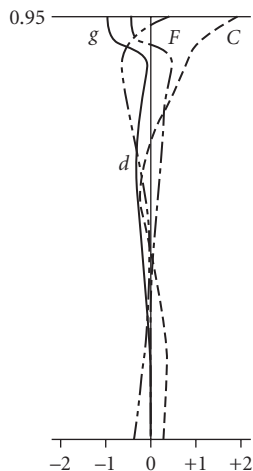


FIGURE 13 Spherical aberration curves for spectral lines (*C*, *d*, *F*, and *g*) of a highly corrected modern microscope objective with a high numerical aperture.²⁴ Ordinate: numerical aperture from 0 (lens axis) to NA = 0.95. Abscissa: longitudinal deviation of focal distance on lens axis indicated in millimeters. (The depth of focus for a 40×/0.95 NA apochromatic objective is approximately 1 mm which corresponds to a depth of field of 0.6 μm in specimen space.)

Oculars As conventionally illustrated, the ocular in a light microscope further magnifies the primary (intermediate) image formed by the objective lens (Figs. 2 and 3). The ocular can also be viewed as the front elements of a macro (relay) lens system made up of the ocular plus the refractive elements of the viewer's eye (Fig. 4a) or a video or photographic camera lens. Special video and photo oculars combine these functions of the ocular plus the video or photo lenses into single units.

The intermediate image plane (that lies between the lenses in many ocular types or precedes the lens elements in the Ramsden-type oculars), or its conjugate plane is used to place field-limiting stops, iris diaphragms, reticles, micrometer scales, comparator beam splitters, and the like that need to appear in the same focal plane as the specimen.

The Ramsden disk, the exit pupil of the objective lens imaged by the ocular, generally appears a short distance above the ocular (Fig. 4b). Since the Ramsden disk should lie in the observer's pupil, special high-eye-point oculars are provided for the benefit of observers wearing corrective eye glasses (especially those for astigmatism). High-eye-point oculars are also used for inserting beam-deviating devices (such as the scanning mirrors in laser scanning confocal microscopes) or aperture-modifying devices (such as aperture occluders for stereo viewing through single objective binocular microscopes²).

The magnification of an ocular is defined as 25 cm divided by the ocular's focal length. On the ocular, the magnification and field number are inscribed (e.g., as 10×/20, meaning 10-power or 25-mm focal length with a field of view of 20-mm diameter), together with manufacturer's name and special attributes of the ocular such as chromatic-aberration-free (CF), wide-field (W, WF, EWF), plan (P, Pl), compensation (Comp, C, K), high-eye-point (H, picture of glasses), with cross hair and orientation stub for crystallography (pol), projection (pro), photographic (photo), video (TV), and the like. Also, special oculars provide larger and flatter fields of view (designated wide field, extra wide field, plan, periplan, hyperplan, etc., some with field numbers ranging up to 28 mm).

Compared to microscope objective lenses, fewer design standards have been adopted and fewer standard abbreviations are used to designate the performance or function of the oculars. Two physical parameters of the oculars have, however, become more or less standardized. The outside diameter of the ocular is either 23.2 mm or 30.0 mm, and the reference distance, or the parafocalizing distance of the ocular (i.e., the location of the intermediate image plane below the flange of the ocular) is now generally set to 10 mm.

In the past, oculars with wide ranges of incremental magnifications were provided to adjust the total image magnification of the microscope, but this practice is now replaced by the use of much fewer, better-corrected oculars coupled with a telan magnification changer in the microscope's body tube, or a zoom projection ocular.

Factors affecting choice of ocular focal length and magnification include optimizing the microscope total magnification and image resolution to match the MTF characteristics of the detector and to adjust the available field coverage. In video-enhanced fluorescence, differential interference contrast, polarizing, dark field, and the like microscopy, the total magnification often needs to be raised beyond the classical "empty magnification" limit, in order to be able to visualize minute objects whose diameters lie well below the limit of microscope resolution.² However, depending on the MTF characteristics, sensitivity, and total pixels available in the sensor, conflicts may arise between the need for greater magnification, image brightness, and field coverage. To optimize the total image magnification, fine trimming of the ocular magnification may be needed, in addition to choosing an objective with the appropriate magnification and NA-to-magnification ratio. Zoom oculars are especially suited for fine-tuning the magnification to optimize S/N ratio and image integration time in video microscopy. For very low light level images, for example in photon-counting imaging, ocular magnifications of less than one may be needed in order to sufficiently elevate the S/N ratio, albeit at a sacrifice to spatial resolution.

In addition to adjusting image magnification and placing the microscope's exit pupil at a convenient location, the ocular compensates for the aberrations that have not been adequately corrected in the objective and tube lens. Huygens oculars combined with lower-power achromatic objectives, and compensating oculars combined with higher-NA achromatic and apochromatic objectives, correct for lateral chromatic aberration. Some higher-NA achromatic objectives are purposely designed to provide residual aberrations (including field curvature) that are similar to those in the apochromats, so that the same compensation oculars can be used to compensate for both types of objectives.

Modern objectives used with the appropriate tube lens are sufficiently well corrected to require minimum or no compensatory correction by the oculars. In research-grade microscopes, the image projected by the objective and tube lens is often recorded directly by placing an electronic image sensor into the intermediate image plane. With objectives that are designed to produce well-corrected intermediate images, oculars themselves are made independently free of lateral and longitudinal chromatic and some spherical aberrations. Regardless of the degree of correction relegated to the ocular, modern microscopes provide images with color corrections, fields of view, and flatness of field much superior to earlier models.

Resolution

Airy Disk and Lateral Resolution Given a perfect objective lens and an infinitely small point of light residing in the specimen plane, the image formed in the intermediate image plane by the objective lens is not another infinitely small point, but a diffraction image with a finite spread (Fig. 14a). This Airy diffraction image is the Fraunhofer diffraction pattern formed by the exit pupil of the objective lens from which spherical waves converge to the focal point. The distribution of irradiance of the diffraction image (Fig. 14b)²⁶ is given by an expression containing the first-order Bessel function $J_1(v)$:

$$I(v) = I_0 \left(\frac{2J_1(v)}{v} \right)^2 \quad (3)$$

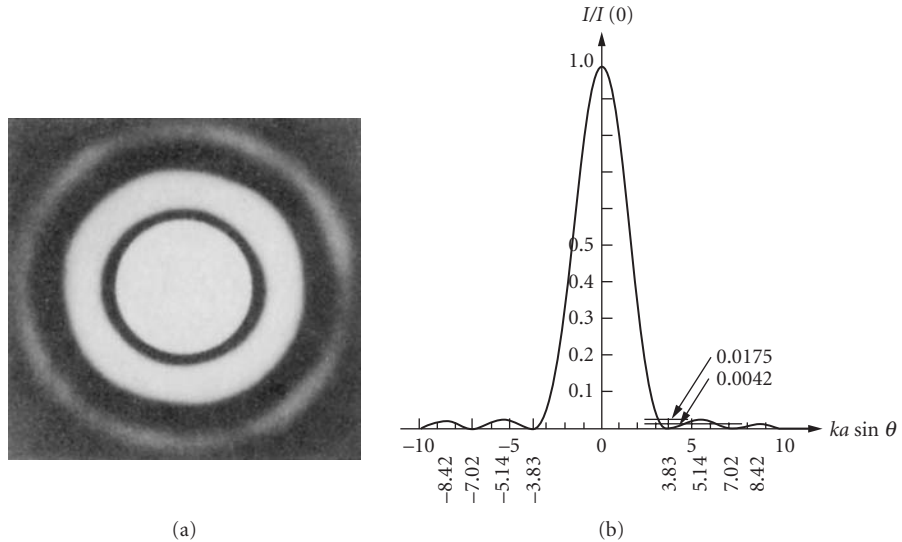


FIGURE 14 Airy pattern of circular aperture: image (a) of central Airy disk, first dark ring and subsidiary maximum and graph (b) of radial intensity distribution.²⁶

with v proportional to the diffraction angle. If the irradiance is calculated as a function of radius measured from the center of the Airy diffraction pattern located in the intermediate image plane, v takes on the form

$$v = 2\pi \frac{\text{NA}}{M\lambda} r_i \quad (4)$$

where NA is the numerical aperture and M the magnification of the objective lens, λ the wavelength of light, and r_i the radial distances measured in the intermediate image plane. If we express r_i as a distance r_o in the object plane, with $r_i = M r_o$, we obtain the more familiar relationship:

$$v = 2\pi \frac{\text{NA}}{\lambda} r_o \quad (5)$$

The central bright disk of the diffraction image is known as the Airy disk, and its radius (the radius from the central peak to the first minimum of the diffraction image) in object plane units is given by

$$r_{\text{Airy}} = 0.61 \frac{\lambda}{\text{NA}} \quad (6)$$

When there exist two equally bright, self-luminous points of light separated by a small distance d in object space, that is the specimen plane, their diffraction images lie side by side in the image plane. The sum of the two diffraction images, assuming the two points of light were mutually incoherent, appears as in Fig. 15a. As d becomes smaller so that the first minimum of one diffraction image overlaps with the central maximum of the neighboring diffraction image ($d = r_{\text{Airy}}$, Fig. 15b),²⁶ their sum (measured along the axis joining the two maxima) still contains a dip of 26.5 percent of the peak intensities that signals the twoness of the source points (the Rayleigh criterion). Once d becomes less than this distance, the two diffraction images rapidly pass a stage where instead of a small dip, their sum shows a flat peak (the Sparrow criterion) at $d = 0.78 r_{\text{Airy}}$, and thereafter the sum of the diffraction images appears essentially indistinguishable from one arising from a single point source instead of two. In other words, we can no longer resolve the image of the two points once they are closer than the Rayleigh criterion, and we lose all cues of the twoness at spacings below

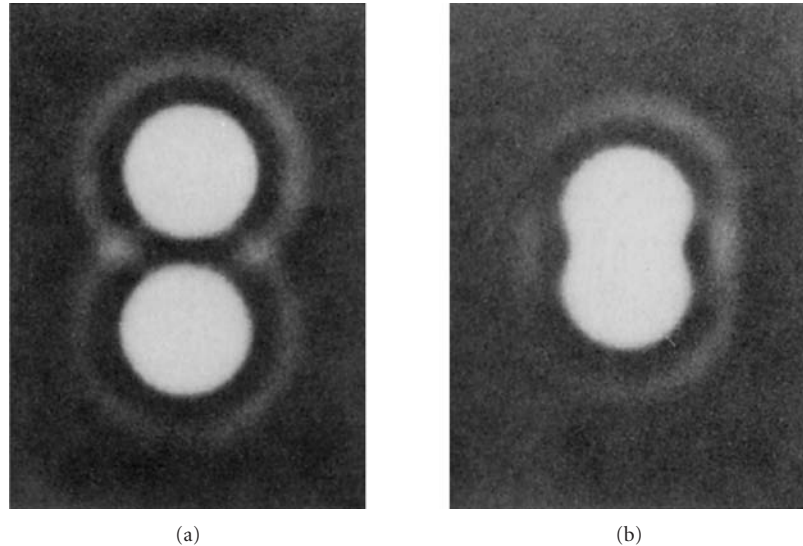


FIGURE 15 Overlapping Airy patterns: (a) clearly resolved and (b) center of Airy patterns separated by $d = r_{\text{Airy}}$, Rayleigh criterion.²⁶

the Sparrow criterion. Since the diameter of the Airy diffraction image is governed by NA_{obj} and the wavelength of the image-forming light λ , this resolution limit normally cannot be exceeded (for exceptions, see the section “Beyond the Diffraction Limit” later in this chapter).

The consideration given here for two-point sources of light applies equally well to two absorbing dots, assuming that they were illuminated incoherently. (Note, however, that it may, in fact, be difficult or impossible to illuminate the two dots totally incoherently since their spacing may approach the diameter of the diffraction image of the illuminating wave. For the influence of the condenser NA on resolution in transillumination, refer to the section on “Transillumination” earlier in this chapter. Also, the contrast of the diffraction images of the individual absorbing dots diminishes rapidly as their diameters are decreased, since the geometrical size of such small dots would occupy a decreasing fraction of the diameter of their diffraction images. For further detail see.)²⁷

The image of an infinitely small point or line thus acquires a diameter equal to that of the Airy disk when the total magnification of the image becomes sufficiently large so that we can actually perceive the diameter of the Airy disk. In classical microscopy, such a large magnification was deemed useless and defined as empty magnification. The situation is, however, quite different when one is visualizing objects smaller than the limit of resolution with video microscopy. The location of the Airy disk can, in fact, be established with very high precision. Distances between lines that are clearly isolated from each other can, therefore be measured to a precision much greater than the resolution limit of the microscope. Also, minute movements of nanometer or even Ångstrom steps have been measured with video-enhanced light microscopy using the center of gravity of the highly magnified diffraction image of marker particles (see “Beyond the Diffraction Limit” later in this chapter).

Three-Dimensional Diffraction Pattern, Axial Resolution, Depth of Focus, Depth of Field The two-dimensional Airy pattern that is formed in the image plane of a **point object** is, in fact, a cross section of a three-dimensional pattern that extends along the optical axis of the microscope. As one focuses an objective lens for short distances above and below exact focus, the brightness of the central spot periodically oscillates between bright and dark as its absolute intensity also diminishes. Simultaneously, the diameters of the outer rings expand, both events taking place symmetrically above and below the plane of focus in an aberration-free system (Fig. 16).²⁸

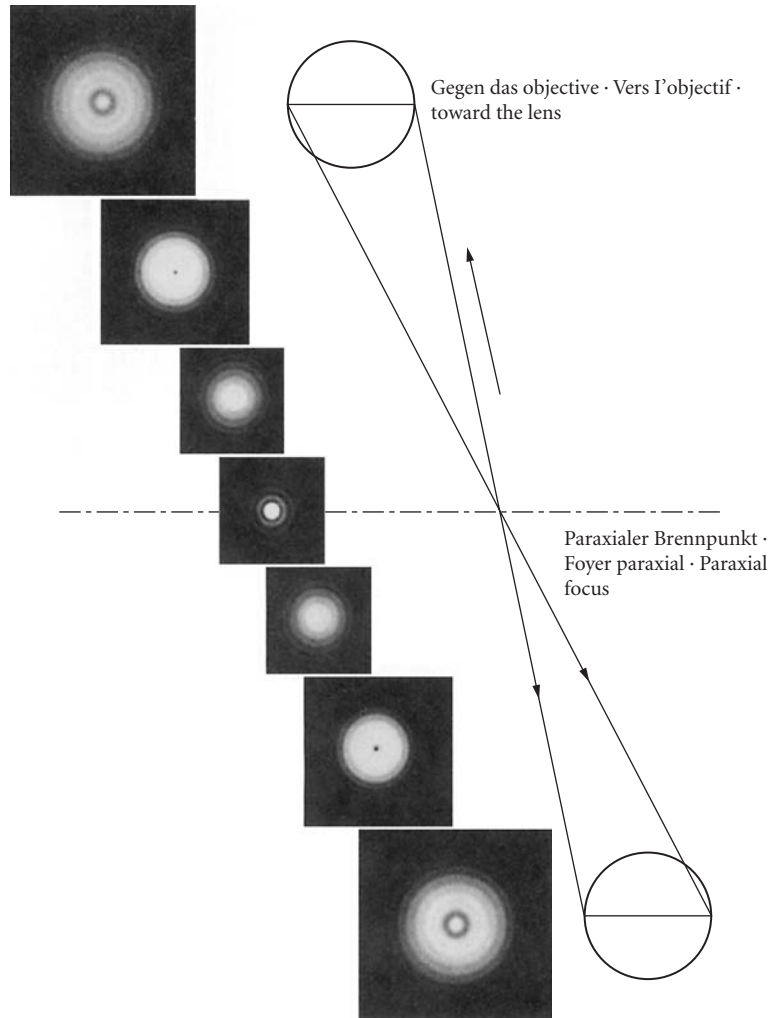
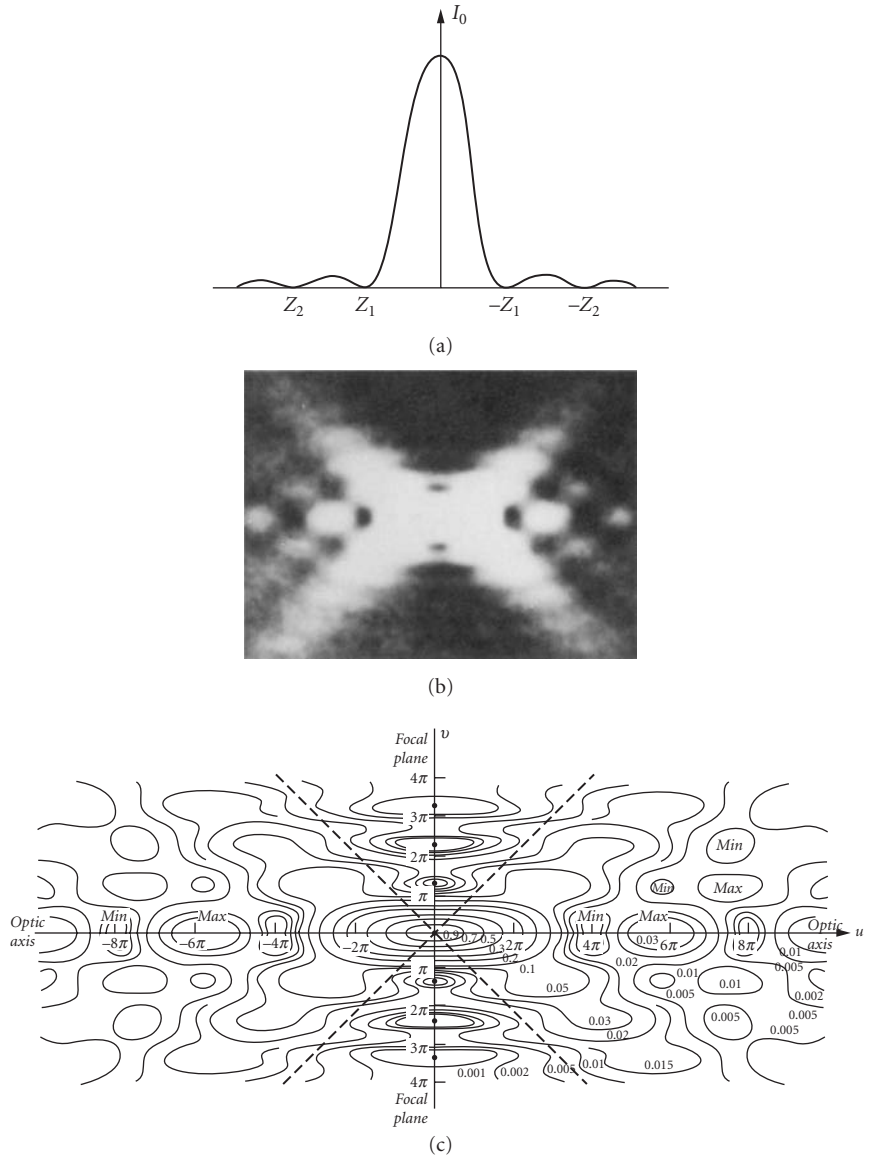


FIGURE 16 The evolution of the diffraction image of a circular aperture with differing planes of focus in an aberration-free system.²⁸

Figure 17 shows an isophote (lines of equal brightness) of the longitudinal section of this three-dimensional diffraction image. The relationship between v and the lateral distance r_i is given by Eq. (4). The axial distance z_i , oriented perpendicular to the image plane, is related to u by

$$u = 2\pi \frac{\text{NA}^2}{M^2 \lambda} z_i \quad (7)$$

In the graph we recognize at $v = 1.22\pi$ (and $u = 0$, focal plane) the first minimum of the Airy pattern which we discussed in the preceding section. The intensity distribution along u perpendicular to the focal plane has its first minima at $u = \pm 4\pi$ and $v = 0 (\pm z_i$ in Fig. 17a). To find the actual extent of the three-dimensional diffraction pattern near the intermediate plane of the microscope, we express the dimensionless variables v and u of Fig. 17c as actual distances in image space.



The first minimum ($u = 4\pi$) is at a distance $z_1 = (2M^2\lambda)/\text{NA}^2$. To transfer distance z_i in image space to distance z_o in object space, we use the relationship $z_i = z_o M^2/n$. (Note that for small axial distances, to a close approximation, the axial magnification is the square of the lateral magnification M divided by the refractive index n of the object medium.) The distance from the center of the three-dimensional diffraction pattern to the first axial minimum in object space is then given by:

$$z_{\min} = 2 \frac{\lambda n}{\text{NA}^2} \quad (8)$$

z_{\min} corresponds to the distance by which we have to raise the microscope objective in order to change from exact focus of a small pinhole to the first intensity minimum in the center of the observed diffraction pattern (see Fig. 16).

In correspondence to the lateral resolution limit, which is taken as the Airy disk radius r_{Airy} [Eq. (6)], we can use z_{\min} as a measure of the limit of *axial resolution* of microscope optics. Note that the ratio of axial to lateral resolution ($z_{\min}/r_{\text{Airy}} = 3.28 n/\text{NA}$) is inversely proportional to the numerical aperture of the objective lens.

The axial resolution of the microscope is closely related to the depth of focus, which is the axial depth on both sides of the *image* plane within which the image remains acceptably sharp (e.g., when a focusing screen at the image plane is displaced axially without moving the object or objective). The *depth of focus* D is usually defined as 1/4 of the axial distance between the first minima above and below focus of the diffraction image of a small pinhole. In the intermediate image plane, this distance is equal to $z_1/2$, with z_1 defined earlier. The depth of focus defined by z_1 is the *diffraction-limited*, or physical, depth of focus.

A second and sometimes dominating contribution to the total depth of focus derives from the lateral resolution of the detector used to capture the image. This geometric depth of focus depends on the detector resolution and the geometric shape of the light cone converging to the image point. If the detector is placed in the intermediate image plane of an objective with magnification M and numerical aperture NA, the geometrical depth of focus D is given by

$$D = \frac{M}{\text{NA}} e \quad (9)$$

with e the smallest distance resolved by the detector (e is measured on the detector's face plate).

The depth in *specimen* space that appears to be in focus within the image, without readjustment of the microscope focus, is the depth of field (unfortunately often also called the depth of focus). To derive expressions for the depth of field, we can apply the same arguments as outlined above for the depth of focus. Instead of moving the image plane in and out of focus, we keep the image plane in the ideal focus position and move the small pinhole in object space. Axial distances in object space, however, are a factor n/M^2 smaller than corresponding distances in image space. Therefore, we apply this factor to the expression for the geometrical depth of focus [Eq. (9)] and add the physical depth of field [derived from Eq. (8)] for the total depth of field d_{tot} :

$$d_{\text{tot}} = \frac{\lambda n}{\text{NA}^2} + \frac{n}{M\text{NA}} e \quad (10)$$

Notice that the diffraction-limited depth of field shrinks inversely proportionally with the square of the NA, while the lateral limit of resolution is reduced inversely proportionally to the first power of the NA. Thus, the axial resolution and thinness of optical sections that can be attained are affected by the system NA much more so than is the lateral resolution of the microscope.

These values for the depth of field, and the distribution of intensities in the three-dimensional diffraction pattern, are calculated for incoherently illuminated (or emitting) point sources (i.e., $\text{NA}_{\text{cond}} \geq \text{NA}_{\text{obj}}$). In general, the depth of field increases, up to a factor of 2, as the coherence of illumination increases (i.e., as $\text{NA}_{\text{cond}} \rightarrow 0$). However, the three-dimensional point spread function with partially coherent illumination can depart in complex ways from that so far discussed when

the aperture function is not uniform. In a number of phase-based, contrast-generating modes of microscopy, the depth of field may turn out to be unexpectedly shallower than that predicted from Eq. (9) and may yield extremely thin optical sections.³⁰

Beyond the Diffraction Limit In recent years the microscope's limit of resolution, as stated in Eq. (1), has been exceeded by different means, relying either on optical, photophysical, photochemical, or computational methods, or a combination thereof. Here we briefly refer to some of the schemes that rely on photonic properties of the specimen, while later in this chapter we will touch on schemes that rely on far-field optical methods, such as structured illumination and confocal microscopy.

Driven by the success of fluorescence microscopy in biomedical research and the need for higher resolution to understand the molecular machinery of the living cell, several methods were devised that exploit the photophysical and photochemical nature of fluorescent molecules. Most of these "super-resolving" methods take advantage of the fact that the position of a single fluorescent molecule (or point of light) can be determined to a much higher precision than the optical resolution of an imaging system. While the resolution of a traditional microscope, as described by Eq. (1), typically does not exceed 200 nm, the same microscope can be used to determine the position of a single fluorophore to 20 nm or better, depending on the number of photons captured and the mobility of the fluorescent molecule.^{31,32} Here we briefly describe those methods that have become prominent and are recognized by their acronyms. For a more detailed discussion we refer to a number of excellent reviews^{33–36} and to the original publications cited below.

Fluorescence imaging with one nanometer accuracy (FIONA) was introduced to measure the detailed stepping motion of a molecular motor (myosin V) along an immobilized track (filamentous actin).³⁷ The detailed, hand-over-hand motion was determined by measuring the location of a single fluorophore, attached to the motor-protein, with a spatial resolution of 1.5 nm and a temporal resolution of 0.5 s. The challenge here included the recording of a sufficient number of photons, within the 0.5 s time window, to localize a single fluorophore that also needed to be photostable enough to allow its observation over several minutes.

Photo-activated localization microscopy (PALM) was introduced to localize immobilized fluorophores at nanometer spatial resolution.³⁸ To this end, fluorophores are used that have to be photoactivated to become fluorescent. A low dose of typically short wavelength light activates a small, random subset of fluorophores that are spaced far enough for their point spread functions to not overlap. The locations of activated fluorophores are measured at nanometer precision and during the measurement process fluorophores become irreversibly bleached. The cycle of low-dose activation and subsequent position measurements is repeated many times and the aggregate position information from all cycles is assembled into a single, super-resolution image.

Stochastic optical reconstruction microscopy (STORM) uses similar principles as PALM but exploits photo-switchable fluorophores that can be turned on and off by exposing them to light pulses of differing wavelengths.³⁹

Single molecule high-resolution colocalization (SHREC) takes advantage of separating the fluorescence of two or more single fluorophores by their spectral characteristics.⁴⁰ By using chromatically differing fluorescent molecules as probes, the probes can approach each other closer than the Rayleigh limit and still be distinguished. The technique is typically used to measure intramolecular distances of 10 nm or more in doubly labeled macromolecules or molecular complexes.

Fluorescence resonance energy transfer or Förster resonance energy transfer (FRET) refers to a photophysical effect that transfers the excitation energy of a fluorescent donor molecule to a nearby fluorescent acceptor molecule. The appropriately chosen donor and acceptor molecules have to be less than 10 nm apart for the radiationless transfer to be effective. For example, FRET can be used to analyze the conformational change of a protein that brings two molecular subunits closer together or farther apart, resulting in enhanced or reduced acceptor fluorescence, respectively. Hence, FRET is a ratiometric method that allows measurement of the internal distance in the molecular frame rather than in the laboratory frame, which makes it largely immune to instrumental noise and drift. While regular FRET reveals the population distributions of interdye distances, single molecule FRET is used to monitor single molecules for long stretches of time.^{41,42}

Stimulated emission depletion (STED) provides a means of point spread function engineering to improve the optical resolution beyond the diffraction limit. A typical single-point scanning STED microscope uses a regularly focused excitation beam that is superimposed by a doughnut-shaped STED beam that instantly quenches excited molecules at the periphery of the excitation spot, thus confining fluorescence emission to the doughnut zero. Saturated quenching results in a fluorescent spot far below diffraction whose scanning across the sample yields a subdiffraction-resolution image.^{34,43}

All the above methods rely on fluorescence microscopy. A general approach to improve resolution was proposed by Harris⁴⁴ who argued that the diffraction pattern in the Fourier plane can be extrapolated beyond the spatial frequency that is cut off by the NA of the objective lens—in other words, that the limit of resolution can be exceeded by computational extrapolation of the diffraction orders as long as the specimen is illuminated in a narrowly limited field.

The field of illumination can be reduced beyond that defined by diffraction by placing the minute exit aperture of a tapered light guide or a minute pinhole closely adjacent to the specimen. By scanning such an aperture relative to the specimen, one obtains a proximity-scanned image whose resolution is no longer limited by the diffraction orders captured by the objective lens. Instead, only the size of the scanning pinhole and its proximity to the specimen limit the resolution.⁴⁵

For nonoptical microscopes, for example in scanning tunneling, force, and other proximity-scanning microscopes, resolution down to atomic dimensions can be obtained on images that reflect topological, electronic, ionic, and mechanical properties of the specimen surface.⁴⁶ In these types of proximity-scanning microscopes, a fine-tipped probe, mounted on a piezoelectric transducer that provides finely controlled x , y , and z displacements of the probe, interacts with specific properties of the specimen surface (alternatively, the probe may be fixed and the sample mounted to the transducer). The resulting interaction signal is detected and fed back to the z -axis transducer, which generally induces the probe tip to rise and fall with the surface contour (that reflects the particular electrical or mechanical property of the surface) as the probe is scanned in a raster fashion along the x and y directions over an area several tens of angstroms to several tens of micrometers wide. A highly magnified contour image of the atomic or molecular lattices is generated on a monitor that displays the z signal as a function of the x , y position.

28.4 CONTRAST AND IMAGING MODES

In microscopy, the generation of adequate and meaningful contrast is as important as providing the needed resolution. Many specimens are practically transparent and differ from their surroundings only by slight changes in refractive index, absorbance, reflectance, or optical anisotropy such as birefringence and dichroism. Most objects that are black or show clear color when reasonably thick become transparent or colorless when their thickness is reduced to a few tenths of a micrometer (since absorption varies exponentially with thickness). Additionally, in microscopy the specimen is often illuminated using a highly convergent beam to maximize resolution, thus reducing shadows and other contrast cues that aid detection of objects in macroscopic imaging. Furthermore, contrast is reduced at high spatial frequency because of an inherent fall-off of the contrast transfer function.

Many modes of contrast generation are used in microscopy partly to overcome these limitations and partly to measure, or detect, selected optical characteristics of the specimen. Thus, in addition to simply raising contrast to make an object visible, the introduction of contrast that reflects a specific physical or chemical characteristic of the specimen may impart particularly important information.

As a quantitative measure of expected contrast generation as functions of spatial frequencies, the modulation transfer functions (MTFs, of sinusoidal gratings) can be calculated theoretically for various contrast-generating modes assuming ideal lenses (Figs. 18 and 19),^{47,48} or on the basis of measured point or line spread functions.⁴⁹ Alternatively, the contrast transfer function (CTF, of square wave gratings) can be measured directly using test targets made by electron lithography (Fig. 20).⁵⁰

The rapid advance of electronic imaging and digital image processing in recent years made the quantitative evaluation of microscope images much more practical. Many computerized image-processing platforms provide standard functions to characterize the morphology and geometric

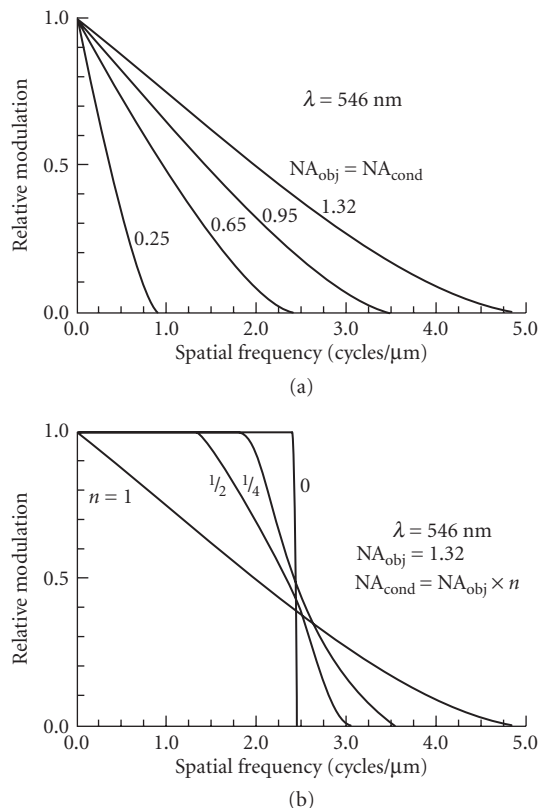


FIGURE 18 Modulation transfer function (MTF) curves for microscope lenses, calculated for periodic specimens in focus: (a) each curve represents a different numerical aperture (NA), which is the same for the objective and condenser lens in these curves. (b) These MTF curves all represent an objective lens of 1.32 NA, but with different condenser NAs; the conditions are otherwise the same as in (a). (Courtesy of Dr. G. W. Ellis.)²

relationship between image features. In addition, specialized systems that provide computer control of microscope components and settings in conjunction with quantitative image analysis provide advanced imaging modalities and new contrast modes that can no longer be viewed through the ocular, but can only be displayed on a computer screen. These hybrid contrast modes usually build on a traditional imaging mode and extend it through exact control and quantitation of image content. Therefore, in the following section we will present traditional imaging modes and give brief descriptions of related hybrid contrast modes.

Bright Field

Whether on an upright or inverted microscope, bright field is the prototypic illumination mode in microscopy (Fig. 4). In transmission bright-field illumination, image contrast commonly arises from absorption by stained objects, pigments, metal particles, etc., that possess exceptionally high extinction

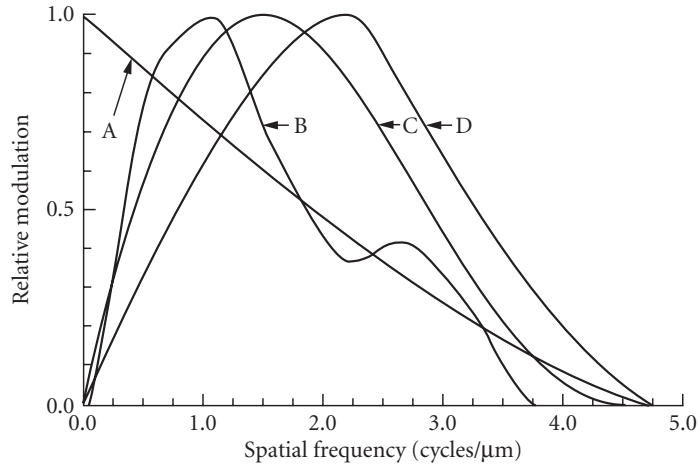


FIGURE 19 Modulation transfer function curves calculated for different modes of microscope contrast generation. A = bright field, B = phase contrast, C = differential interference contrast, and D = single-sideband edge enhancement. The curves are plotted with their peak modulation normalized to 1.0. (Courtesy of Dr. G. W. Ellis.)²

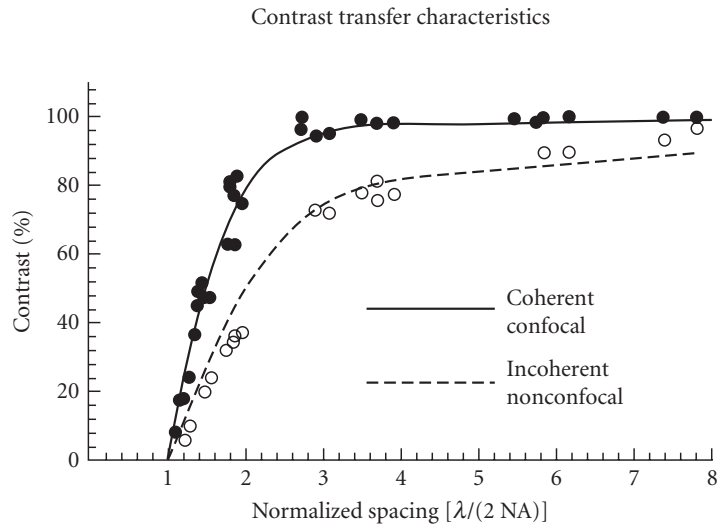


FIGURE 20 Measured contrast transfer values plotted as a function of spatial period in Airy disk diameter units, to normalize the values measured with different lenses and wavelengths. Data points were obtained with a laser spot scan microscope operating in the confocal reflection mode (*solid points*) and the nonconfocal transmission mode (*circles*). Curves are calculated contrast transfer values for the coherent confocal and the incoherent nonconfocal imaging mode.⁵⁰

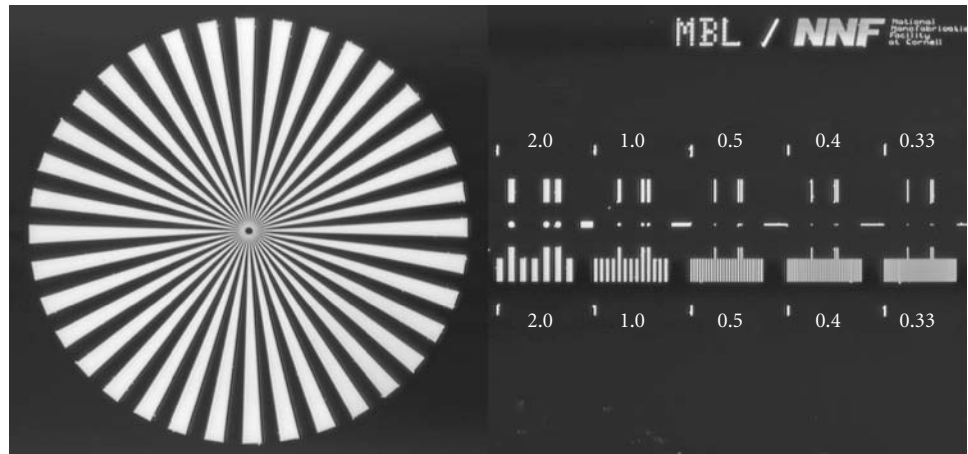


FIGURE 21 Siemens star, line and dot patterns that are part of the MBL/NNF test target imaged in bright field using transmitted light and a 60×/1.4 NA Plan Apo oil immersion objective lens (Nikon Inc.) and matching condenser. The dark background is due to the low transmittance of the 50-nm-thick aluminum film. Bright features were etched into the film using electron lithography. Numbers above and below bar gratings show period in microns. The Siemens star consists of 36 wedge pairs, with an outer diameter of 75 μm . The period near the outer edge is 6.5 μm , decreasing continuously toward the center. The smallest period is 0.1 μm near the inner black disk, which has a diameter of 1.2 μm .

coefficients (Fig. 21). Transparent objects only generate very weak contrast based on Becke lines introduced by refraction at object boundaries that are slightly out of focus. (The dark Becke line, which is used for immersion determination of refractive index of particles,⁵¹ surrounds, or lies just inside, a boundary with a sharp gradient of refractive index when the boundary is slightly above or below focus. The Becke line disappears altogether when a thin boundary is exactly in focus.)

To gain additional contrast, especially in bright-field microscopy, the condenser NA is commonly reduced by closing down its iris diaphragm. This practice results in loss of resolution and superimposition of diffraction rings, Becke lines, and other undesirable optical effects originating from regions of the specimen that are not exactly in focus. The various modes of optical contrast enhancement discussed in following sections obviate this limitation and provide images with improved lateral and axial resolution as well as improved contrast.

Before the advent of phase-contrast and differential interference-contrast (DIC) microscopy, oblique illumination (that can be attained by off-centering a partially closed condenser iris diaphragm) was used to generate contrast of transparent objects. While this particular approach suffered from the problems listed in the previous paragraph, combination of oblique illumination at large condenser NA with video contrast enhancement proves to be an effective method for generating DIC-like thin optical sections.⁵²

Recently, the optical phenomenon that leads to the formation of the Becke line has been explored more thoroughly, from a theoretical and an experimental point of view.^{53–56} The goal is to retrieve phase information from images of objects that affect the phase of transmitted or reflected light, but not necessarily its amplitude. Usually, phase information is gained from specially designed setups that enhance interference effects between light waves that have different optical paths through the specimen. The following sections on phase-contrast, polarized light, and interference microscopy give examples of these specialized imaging modes. Streibl,⁵³ on the other hand, proposed to use a regular bright field microscope and the phenomenon of the Becke line to retrieve phase information of weakly scattering objects. He presented a theoretical framework based on the intensity transport equation and demonstrated the enhancement of phase objects based on images that were recorded at slightly different focus positions. Nugent and collaborators^{55–57} have refined the theory and developed a practical implementation called *quantitative phase microscopy*.

In reflection bright-field microscopy, the image is formed by the reflected or backscattered light of the specimen, which is illuminated through the objective (see the section “Epi-illumination”). Reflection contrast is used primarily for opaque and thick samples, especially for metals and semiconductors. Reflection contrast is also finding increasing applications in autoradiography and in correlative light and electron microscopy for detecting the distribution of colloidal gold particles that are conjugated to antibodies and other selective indicators.

Total frustrated reflection microscopy⁵⁸ generates contrast due to objects that are present in a low-refractive-index medium located within the evanescent wave that extends over a distance only a fraction of a wavelength from the microscope coverslip surface. Regions of the specimen whose refractive index differs from its milieu produce interference fringes whose contrast sensitively reflects the refractive index difference and distance from the coverslip surface.

Dark Field

In dark field microscopy the illuminating beam is prevented from entering the image-forming ray paths. The background of the field is dark, and only light scattered by optical discontinuities in the specimen is designed to appear in the image as bright lines or dots. Thus, contrast can become extremely high, and diffraction images can be detected as bright points or lines even when the diameter of the scattering object becomes vanishingly small compared to the microscope’s limit of resolution.^{8,27,30,59}

For small objects that are not obscured by other light-scattering particles (a condition rather difficult to achieve) and are free in a fluid substrate, Brownian motion of the object and the time constant and sensitivity of the detector, rather than the object’s absolute size, are more likely to set a lower limit to the size of the object that can be clearly visualized with dark field microscopy.

Phase-Contrast and Other Aperture-Modifying Contrast Modes

Microscopic objects, distinguished from their surround only by a difference of refractive index, lose their Becke line and disappear altogether when brought exactly into focus. Nevertheless, light diffracted by the small object still suffers a $\lambda/4$ phase shift relative to the undeviated background wave by the very act of being scattered (by a nonabsorbing object; the phase shift upon scattering by an absorbing object is $\lambda/2$).⁶⁰ As shown in Fig. 22, light s scattered by the small object and the undeviated light u , both originating from a common small point A of the condenser aperture, traverse different regions of the objective lens aperture. At the objective aperture, the undeviated light traverses only point B that is conjugate to A , while the scattered light passes those regions of the aperture defined by the spatial periods of the object.

Since light waves s and u arise from the same points in object space but traverse regions that are spatially separated in the objective aperture plane, a *phase plate* introduced in that plane can be used to modify the relative phase and amplitudes of those two waves. The phase plate is configured to subtract (or add) a $\lambda/4$ phase to u relative to s so as to introduce a $\lambda/2$ (or zero) phase difference between the two and, in addition, to reduce the amplitude of the u wave so that it approximates that of the s wave. Thus, when the two waves come to focus together in the image plane, they interfere destructively or constructively to produce a darker or brighter in-focus image of the small, transparent object against a dark gray background (positive and negative phase contrast).

As generally implemented, an annulus replaces the pinhole in the condenser aperture, and a complementary phase ring in the objective aperture plane or its conjugates (covering a somewhat larger area than the undisturbed image of the annulus in order to handle the u waves displaced by out-of-focus irregularities in the specimen) replaces the simple phase disk. Figure 23 shows an example of a phase object that was imaged using phase-contrast optics as described above. The object is a Siemens star that was etched into a thin layer of silica and imaged using a Olympus $100 \times /1.3\text{NA}$ Plan Apo objective and condenser with complementary phase rings.

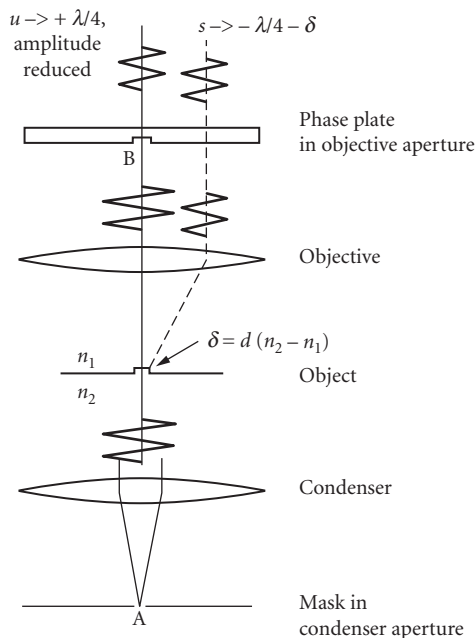


FIGURE 22 Optical principle of phase-contrast microscopy illustrating the phase relationships between waves of the light s scattered by the specimen and the undeviated light u (see text).

In the Polanret system, the phase retardation and effective absorbance of the phase ring can be modified by use of polarization optical components so that the optical path difference of a moderately small object can be measured by seeking the darkest setting of the object.^{61,62} Similarly, the Polanret system can be used to accentuate color or low contrast due to slight absorption by the object.

Several modes of microscopy, including phase contrast, take advantage of the facts that (1) the front condenser and back objective lens apertures are conjugate planes, (2) the illuminating beam arising out of each point of the condenser aperture is variously deviated by the specimen structure according to its spatial frequency, and (3) the back objective aperture is the Fourier plane of the specimen plane.

In Hoffman modulation contrast microscopy, the condenser aperture contains a slit mask with the slit placed toward the edge of the aperture. The objective aperture holds a second, complementary mask, called a modulator, which consists of two parts (Fig. 24).⁶³ The dark part covers the smaller sector to one side of the projected slit and the gray part covers the slit area. The objective mask thus attenuates the zero-order light undeviated by the specimen and removes the light diffracted by the specimen to one side of the zero-order beam. The light deviated by specimen structure away from the dark sector of the mask passes unchanged, while the light deviated toward the dark sector is blocked. Thus, the image becomes shadow-cast, similar in appearance to DIC that reflects gradients of refractive indices or of optical path differences in the specimen.

Developed by Gordon W. Ellis in 1978⁶⁴ single-sideband edge enhancement microscopy (SSEE) generates directional image contrast of phase objects, with greater modulation transfer than by phase-contrast or DIC microscopy at high spatial frequencies (Fig. 19). SSEE is also capable of generating exceptionally thin optical sections (Fig. 25). (In 1988, Ellis also devised aperture-scanning phase-contrast microscopy, a method which generates full resolution phase-contrast images with virtually no halos;⁶⁵ see Fig. 2-47 in Ref. 2.)

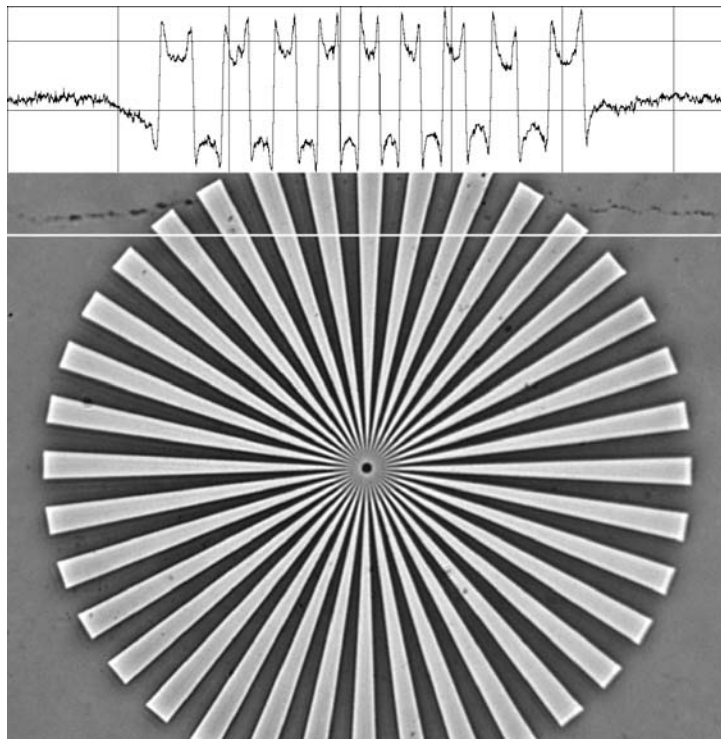


FIGURE 23 Siemens star etched into 90-nm-thick SiO_2 layer and imaged with phase contrast. The dimensions of the star pattern are the same as the one described in Fig. 21. The wedges that were etched away appear bright in this image. Light that has passed through the etched wedges is phase-advanced with respect to light that has passed through the rest of the pattern. (The SiO_2 layer was deposited on a 170- μm -thick coverglass, etched using electron lithography, and mounted on a microscope slide, leaving an air gap between slide and silica layer; 100 \times /1.3NA oil immersion Plan Apo objective.) The intensity profile along a horizontal line near the top illustrates deviations from the step function of the corresponding optical path difference. The accentuation of the edge contrast in this profile is an artifact of the phase-contrast method commonly implemented in form of an illumination ring in the condenser aperture and a complementary phase ring in the objective aperture.

SSEE takes advantage of the fact that illuminated by a condenser whose aperture is half masked, the two side bands (shifted by specimen diffraction to the left and right) are both phase shifted relative to the illuminating light (carrier wave) by $\lambda/4$, but with opposite signs. (As shown by Zernike,⁶⁰ the image contrast of a phase grating viewed with a bright field microscope disappears at exact focus, since the two side bands are in opposite phase.)

In the SSEE microscope, contrast is generated by interference between the attenuated carrier wave and one of the side bands (Fig. 26). Alternately, both side bands may be used with one of the side bands phase shifted by $\lambda/2$ (and appropriately attenuated) relative to the other. Interference between the attenuated carrier wave and the side band generates a high-contrast, high-resolution, in-focus image of the specimen's phase boundaries proportional to their orientation perpendicular to the straight edge of the half mask in the condenser.

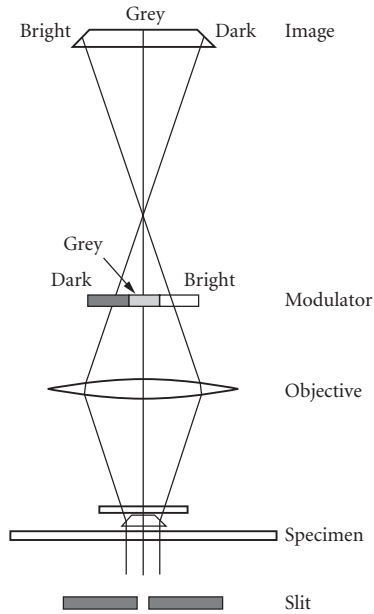


FIGURE 24 Schematic diagram indicating regions of the modulator that modify light from phase gradients in the object to enhance contrast.⁶³

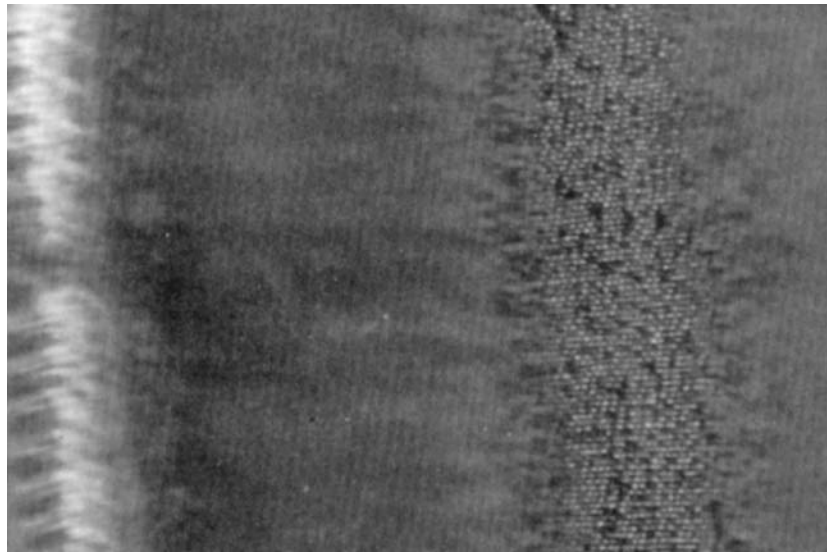


FIGURE 25 Optical section of the silicate shell of a diatom (*Surirella gemma*) observed with SSEE. The tiny pores are in focus over only a highly limited region of the shell due to the highly effective optical sectioning capability of SSEE. (Image copied and cropped from Fig. 2-50 in Ref. 2. Original image courtesy of Dr. Gordon W. Ellis, University of Pennsylvania.)

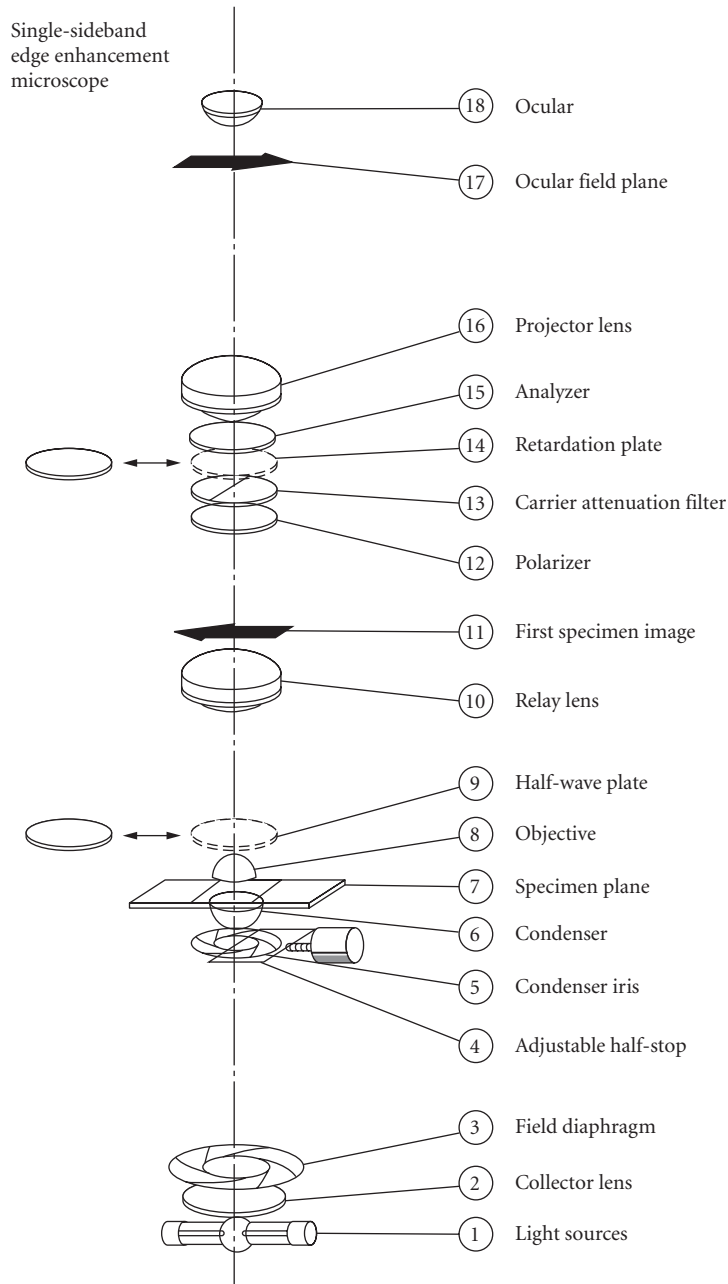


FIGURE 26 Schematic diagram of the edge enhancement single-sideband microscope (SSEE).⁶⁴

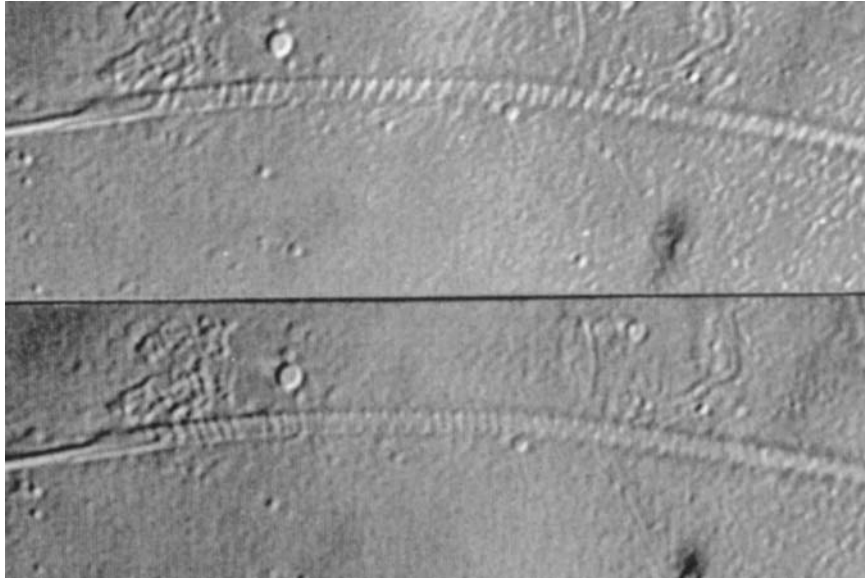


FIGURE 27 Gyres of chromosomes in live sperm head of cave cricket. The images were obtained with SSEE using selected e-vectors as described in the text. Besides rectified polarization microscopy (Fig. 36), few contrast-generating methods besides SSEE have been able to distinctly display these chromosome gyres. (Image copied from Fig. 2-51 in Ref. 2. Original image courtesy of Dr. Gordon W. Ellis, University of Pennsylvania.)

In SSEE, polarizing elements placed *after* the specimen attenuate and phase shift the carrier wave relative to the side bands (Fig. 26). Thus by adjusting the azimuth of the polarizer immediately following the specimen, one can capture exceptionally high resolution images reflecting the birefringence distribution and axes in the specimen (Fig. 27). Also, since the specimen is not sandwiched between crossed polarizers, image contrast in SSEE is not affected by birefringence of the specimen chamber as is the case with polarization and DIC microscopy.

Interference

While all modes of contrast generation in light microscopy in fact depend on interference phenomena, a group of instruments is nevertheless known separately as interference microscopes. These microscopes form part of an interferometer, or contain an interferometer, that allows direct measurements of optical path difference (or generation of contrast) based on interference between the waves passing the specimen and a reference wave. The interferometric and polarization microscopy techniques, which are considered below, generate complementary phase images of the specimen: distribution of refractive index and distribution of refractive index anisotropy, respectively.

Many interference microscopes employ amplitude-dividing beam splitters for setting up the two-beam interference scheme. Instead of amplitude division, division of wavefront can also be used to create both beam paths, especially when using a laser light source. Among the many designs that have been proposed and manufactured, amplitude division interference microscopes can be classified into three major groups: (1) the two-arm type with two separate beam paths, one containing the sample, the other for controlling the reference beam, with separate microscope optics in both arms or microscope optics only in the sample arm; (2) the beam-shearing type in which the reference wave is generated by displacing a beam laterally within the field of a single microscope; and

(3) the dual focus type in which the reference wave is focused to a different level than the specimen plane, again in a single microscope. All schemes can be implemented in transmission or reflection mode.^{66,67}

The image in an interferometric microscope is created by the superposition of a probe and a reference beam. We denote the intensities in the probe and reference beam as I_p and I_r , and their respective phases as ϕ_p and ϕ_r . The intensity that results from superimposing the probe and reference beam can be expressed as described in^{17,26}

$$I = I_p + I_r + 2|\gamma_{pr}|\sqrt{I_p I_r} \cos(\phi_p - \phi_r) \quad (11)$$

where $|\gamma_{pr}|$ is the modulus of the normalized mutual coherence function or the degree of coherence between the probe and reference image. This equation does not include polarization effects and assumes that both interfering beams have the same polarization. For quasi-monochromatic light the optical path difference (OPD) that is associated with the phase angle difference is given by

$$\text{OPD} = \frac{\bar{\lambda}}{2\pi}(\phi_p - \phi_r) \quad (12)$$

where $\bar{\lambda}$ is the center wavelength.

We note that in Eq. (11) I can stand for an array of intensity values representing the pixels of a digital image that was recorded with an appropriate camera attached to an interference microscope.

When using white light, each wavelength produces its own interference picture. White light interference pictures are only observed when the optical path difference between the probe and the reference beam is less than a few wavelengths. Let's assume that in a uniform image region the OPD is zero, hence the interference of each wavelength is constructive and the recorded spectrum in that region is white. However, if the OPD is finite, the wavelength that is twice the OPD is suppressed due to destructive interference and therefore that wavelength is missing from the spectrum recorded in the region. When systematically increasing the OPD from 0 to 2000 nm, for example, a characteristic change in spectrum is observed in the region, transitioning from white (OPD = 0), to blue (OPD = 300 nm), to yellow (OPD = 600 nm), to indigo (OPD = 900 nm), to a greenish yellow (OPD = 1600 nm), and bluish grey (OPD = 2000 nm).⁶⁸ As the OPD increases above 1000 nm, colors become less saturated and approach white again for OPDs of several thousand nanometers.

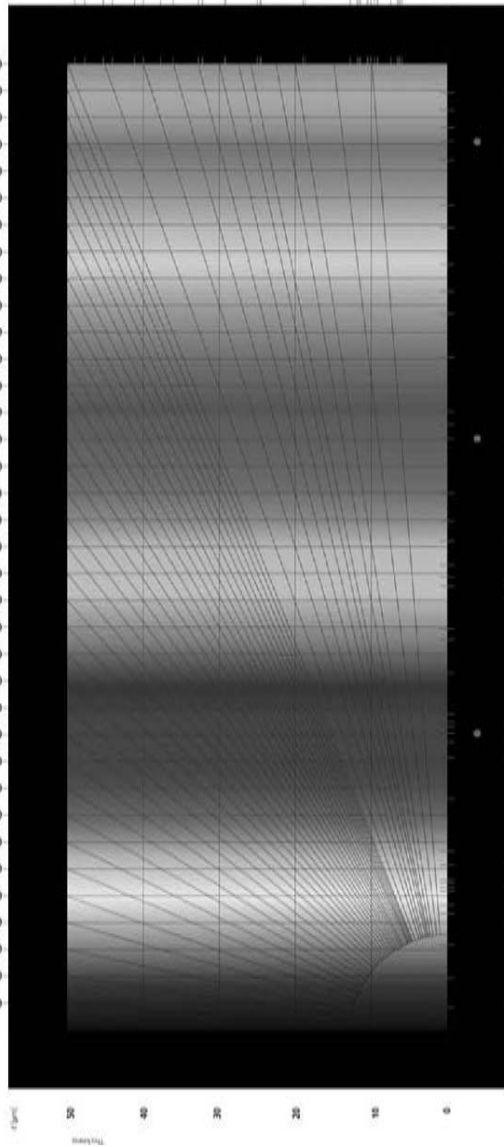
In some interferometric schemes there is an additional achromatic half-wave phase shift, for instance, due to polarization transformation, reflection, and the like. In this case, a zero optical path difference produces destructive interference at all wavelengths and a uniform image region with zero OPD appears black. For small OPDs (< 200 nm) the destructive interference is relaxed for all wavelengths simultaneously and the brightness of the region increases, first with a white spectral composition. With increasing OPD, the region becomes colored due to constructive and destructive interference of specific wavelengths leading to the following color sequence: light yellow (OPD = 300 nm), indigo (OPD = 600 nm), yellow (OPD = 900 nm), grey blue (OPD = 1600 nm), and whitish grey (OPD = 2000 nm). This sequence of interference colors is reproduced in the Michel-Lévy chart (see Fig. 28), which is used to rapidly estimate the OPD based on the observed color of a uniform region. When the OPD increases above 2000 nm, the interference colors turn white and can no longer be used to reliably determine the OPD.

Both interference schemes are implemented. The scheme with destructive interference at 0 OPD is more sensitive (higher signal to noise ratio) for measuring small OPDs, because the background of 0 OPD is black (ideally) and doesn't carry any shot noise, while the white light intensity of constructively interfering beams is subject to shot noise.

When using monochromatic light, the optical path difference between the probe and reference beam can be determined precisely by measuring the intensity in a uniform image region [see Eq. (11)]. However, measurements of OPDs that are larger than the wavelength λ of the monochromatic light result in an apparent OPD that is between 0 and λ . This ambiguity is often referred to as the order of the OPD. The order can be determined by making measurements with two or more wavelengths.

Michel Lévy Color Chart

0.001	Light	White
0.002	White	White
0.003	White	White
0.004	White	White
0.005	White	White
0.006	White	White
0.007	White	White
0.008	White	White
0.009	White	White
0.010	White	White
0.011	White	White
0.012	White	White
0.013	White	White
0.014	White	White
0.015	White	White
0.016	White	White
0.017	White	White
0.018	White	White
0.019	White	White
0.020	White	White
0.021	White	White
0.022	White	White
0.023	White	White
0.024	White	White
0.025	White	White
0.026	White	White
0.027	White	White
0.028	White	White
0.029	White	White
0.030	White	White
0.031	White	White
0.032	White	White
0.033	White	White
0.034	White	White
0.035	White	White
0.036	White	White



-0.040	White	White	0.001
-0.035	White	White	0.002
-0.030	White	White	0.003
-0.025	White	White	0.004
-0.020	White	White	0.005
-0.015	White	White	0.006
-0.010	White	White	0.007
-0.005	White	White	0.008
-0.000	White	White	0.009
0.005	White	White	0.010
0.010	White	White	0.011
0.015	White	White	0.012
0.020	White	White	0.013
0.025	White	White	0.014
0.030	White	White	0.015
0.035	White	White	0.016
0.040	White	White	0.017
0.045	White	White	0.018
0.050	White	White	0.019
0.055	White	White	0.020
0.060	White	White	0.021
0.065	White	White	0.022
0.070	White	White	0.023
0.075	White	White	0.024
0.080	White	White	0.025
0.085	White	White	0.026
0.090	White	White	0.027
0.095	White	White	0.028
0.100	White	White	0.029
0.105	White	White	0.030
0.110	White	White	0.031
0.115	White	White	0.032
0.120	White	White	0.033
0.125	White	White	0.034
0.130	White	White	0.035
0.135	White	White	0.036
0.140	White	White	0.037
0.145	White	White	0.038
0.150	White	White	0.039
0.155	White	White	0.040
0.160	White	White	0.041
0.165	White	White	0.042
0.170	White	White	0.043
0.175	White	White	0.044
0.180	White	White	0.045
0.185	White	White	0.046
0.190	White	White	0.047
0.195	White	White	0.048
0.200	White	White	0.049

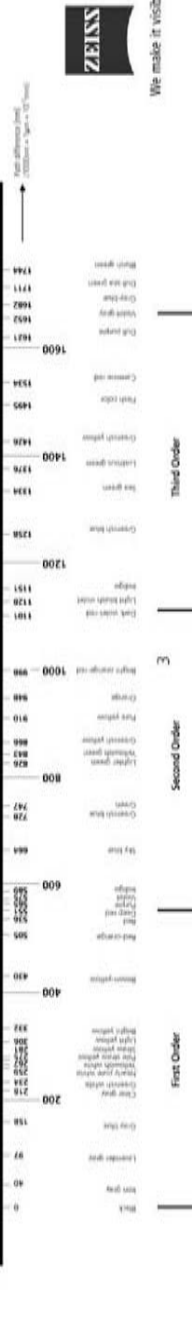


FIGURE 28 Michel Lévy Color Chart of interference colors. The horizontal sequence of colors is associated with the interference of two beams of white light whose mutual path difference increases from 0 (left, black for destructive interference) to more than 1700 nm (right, pale green). By comparing an experimentally observed color with the colors of this chart, one can estimate the path difference caused, for example, by the partial reflection off a thin dielectric film (e.g., soap bubble) or transmission through a thin birefringent sheet (e.g., mica) sandwiched between crossed polarizers. For birefringent materials, the path difference is the product of the birefringence (indicated along the upper and right edge) and the thickness (left edge) of the material. The diagonal lines assist in estimating one of the quantities (birefringence or thickness) from the observed color; if the other quantity is known. This brightness/color sequence is specific to interference phenomena that result in destructive interference for zero path difference (e.g., birefringent sheet between crossed polarizers). A complementary color sequence applies to interference phenomena that result in constructive interference at zero path difference (e.g., birefringent sheet between parallel polarizers). (See also color insert.) (The chart was generously provided by Rudi Rotterfusser and Becky Hohman of Carl Zeiss Microimaging Inc.)

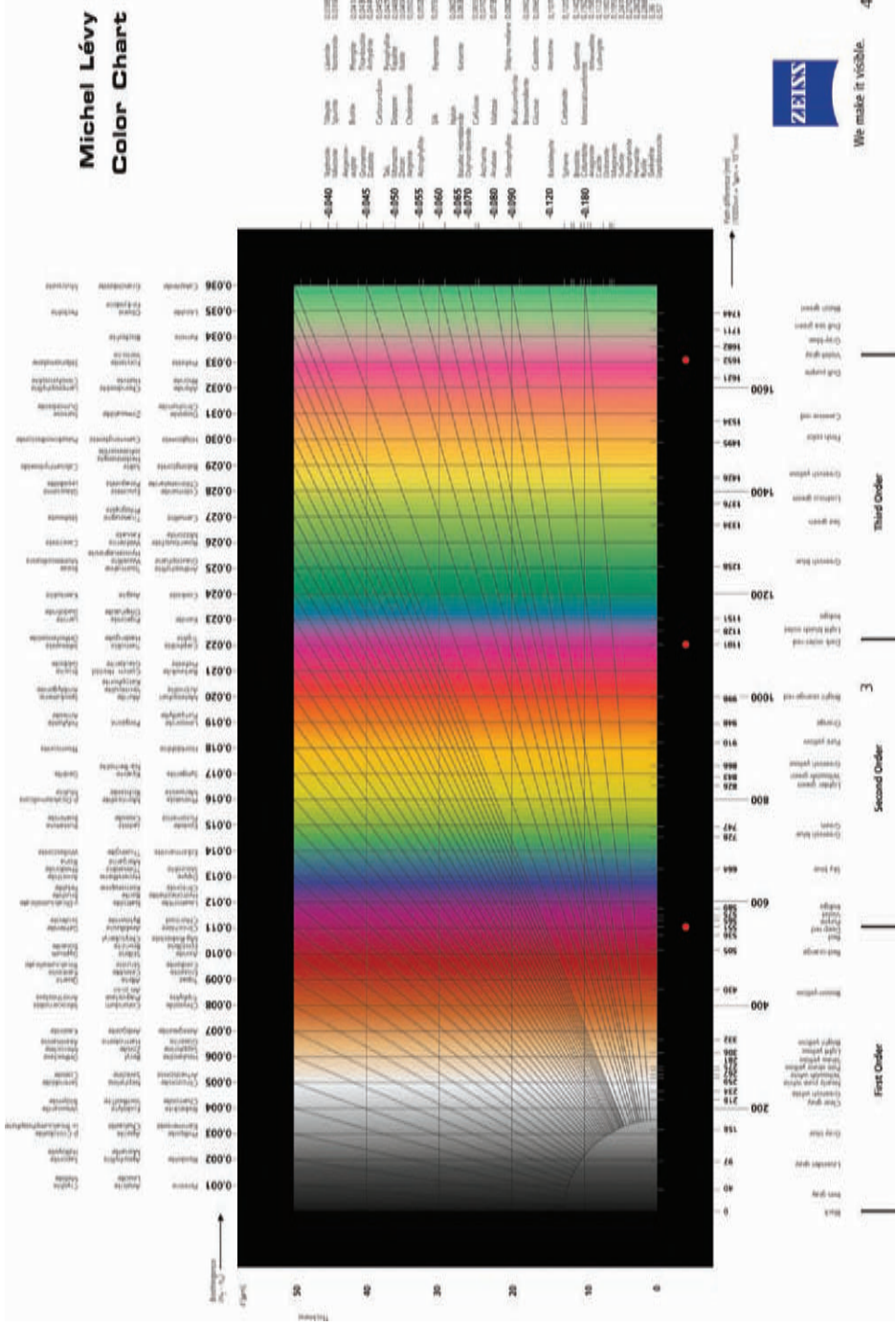


FIGURE 28.28 Michel Lévy Color Chart of interference colors. The horizontal sequence of colors is associated with the interference of two beams of white light whose mutual path difference increases from 0 (left, black for destructive interference) to more than 1700 nm (right, pale green). By comparing an experimentally observed color with the colors of this chart, one can estimate the path difference caused, for example, by the partial reflection off a thin dielectric film (e.g., soap bubble) or transmission through a thin birefringent sheet (e.g., mica) sandwiched between crossed polarizers. For birefringent materials, the path difference is the product of the birefringence (indicated along the upper and right edge) and the thickness (left edge) of the material. The diagonal lines assist in estimating one of the quantities (birefringence or thickness) from the observed color, if the other quantity is known. This brightness/color sequence is specific to interference phenomena that result in destructive interference (e.g., birefringent sheet between crossed polarizers.) A complementary color sequence applies to interference phenomena that result in constructive interference at zero path difference (e.g., birefringent sheet between parallel polarizers.)

Further improvement in measuring the OPD can be achieved by controlling the phase of the reference beam. For example, we can measure the probe plus reference image four times, each time changing the phase of the reference image by a quarter wavelength. According to Eqs. (11) and (12) we find

$$\begin{aligned}
 I &= I_p + I_r + 2|\gamma_{pr}|\sqrt{I_p I_r} \cos\left(\frac{2\pi}{\lambda} \text{OPD}\right) \\
 I &= I_p + I_r - 2|\gamma_{pr}|\sqrt{I_p I_r} \sin\left(\frac{2\pi}{\lambda} \text{OPD}\right) \\
 I &= I_p + I_r - 2|\gamma_{pr}|\sqrt{I_p I_r} \cos\left(\frac{2\pi}{\lambda} \text{OPD}\right) \\
 I &= I_p + I_r + 2|\gamma_{pr}|\sqrt{I_p I_r} \sin\left(\frac{2\pi}{\lambda} \text{OPD}\right)
 \end{aligned} \tag{13}$$

Assuming all other factors constant we can compute the OPD based on the four intensity measurements:

$$\text{OPD} = \frac{\lambda}{2\pi} \arctan\left(\frac{I_4 - I_2}{I_1 - I_3}\right) \tag{14}$$

The last expression relates the OPD to a ratio of intensity differences. Hence, the OPD is measured independent of an intensity offset (because only intensity differences are entered) and independent of a gain factor that is common to all four intensity values (because only an intensity ratio is entered).

As noted earlier, I_1, \dots, I_4 can be interpreted as arrays of intensity values representing the pixels of four digital images. In this case, the expression for OPD represents an image arithmetic operation that generates a map of the spatial variations of the measured optical path differences. This or similar image-processing schemes can be implemented using various interference microscope designs after adding appropriate equipment for electronic imaging and phase control.

Mach-Zehnder Interference Microscope The classical two-arm interference microscope with identical optics in both arms is the Mach-Zehnder interference microscope as designed by Horn (Leitz of Wetzlar) in the 1950s (Fig. 29). The intricate and sturdy design earned it the nickname “Rolls Royce of the microscopes,”⁶⁹ including its cost, which was comparable to that of an electron microscope of the time. The microscope, while straightforward in principle, requires close matching of the optics in the two interferometer arms and a mechanical design that provides exceptional precision and stability. Thus, in addition to using matched pairs of objectives and condensers and inserting a blank slide (that is similar to the specimen-containing slide) into the reference arm, one needs to carefully adjust the built-in beam deviators, path equalizers, and wedge components to reduce the difference in optical path length between the two arms to less than the coherence length of the quasi-monochromatic light. (The coherence length of light with a center wavelength $\bar{\lambda}$ and a bandwidth of $\Delta\lambda$ is $\bar{\lambda}^2/\Delta\lambda = 30 \mu\text{m}$ for $\bar{\lambda} = 550 \text{ nm}$, $\Delta\lambda = 10 \text{ nm}$.) While unfortunately no longer manufactured, this type of microscope permits precise interferometric measurements of microscopic objects both in the uniform field mode and the fringe displacement mode, and can even be used to generate holograms.²

Linnik Interference Microscope In 1933, V.P. Linnik proposed a two-arm reflective-type interference microscope with two matching objectives and a single ocular.⁷⁰ The optical scheme, also called the Linnik micointerferometer, is shown in Fig. 30a. The illumination is split and recombined by the same beam splitter before the microscope objective lens where the beam has low divergence. The probe beam and reference beam then pass through separate but matching objectives and reflect off the specimen and reference mirror, respectively. The objectives can have high NA and short working distance, but require close matching for efficient interference of the probe and reference beams in the common image plane or behind the ocular. Closely matched objectives reduce the influence

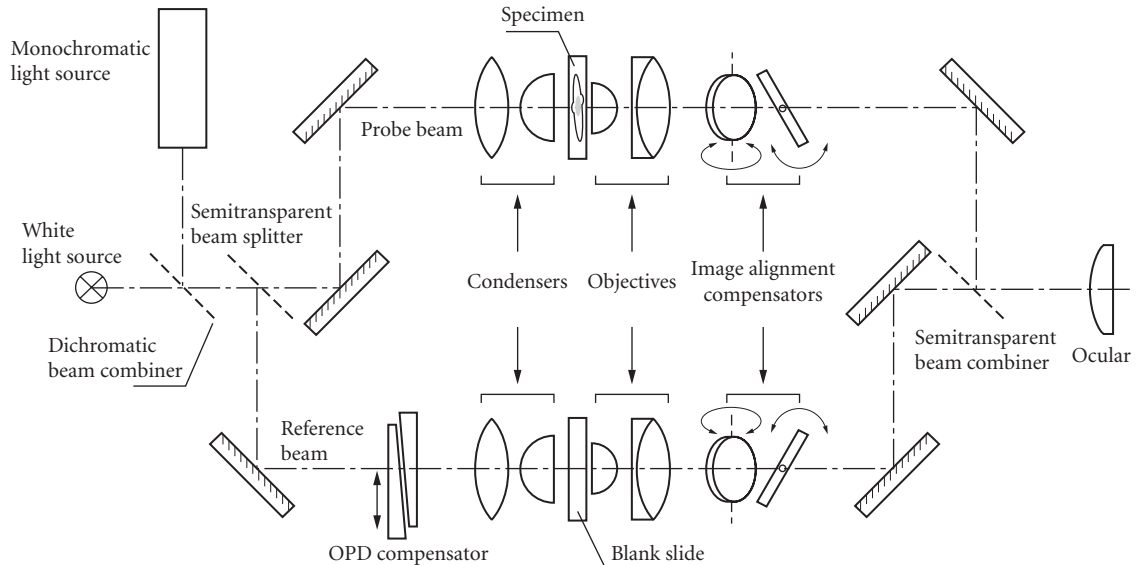


FIGURE 29 Designed by Horn the Mach-Zehnder-type interference microscope with two complete sets of microscope optics, one in each arm of a Mach-Zehnder interferometer.

of chromatic dispersion and other optical aberrations on the interference image. This is essential if a broad-band light source is used, because the dispersion and the optical path length must be closely matched across the entire useful field in each arm. Linnik type interference microscopes are still manufactured by LOMO, Russia.

The original Linnik design can be modified as proposed here by Michael Shribak and shown in Fig. 30*b*. The modification replaces the regular beam splitter with a polarizing one and adds

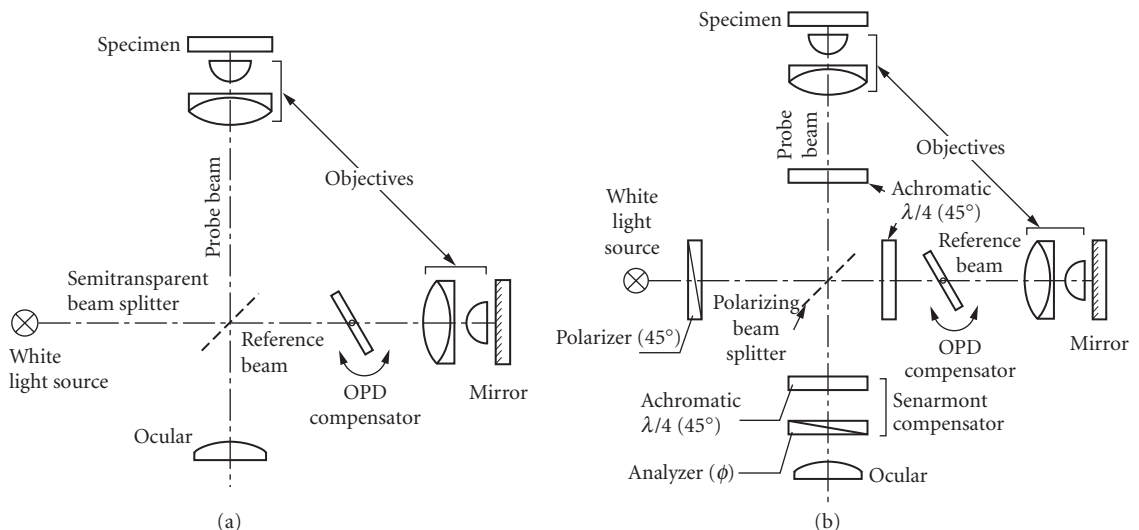


FIGURE 30 The Linnik-type interference microscope with two identical objectives, one in each arm.

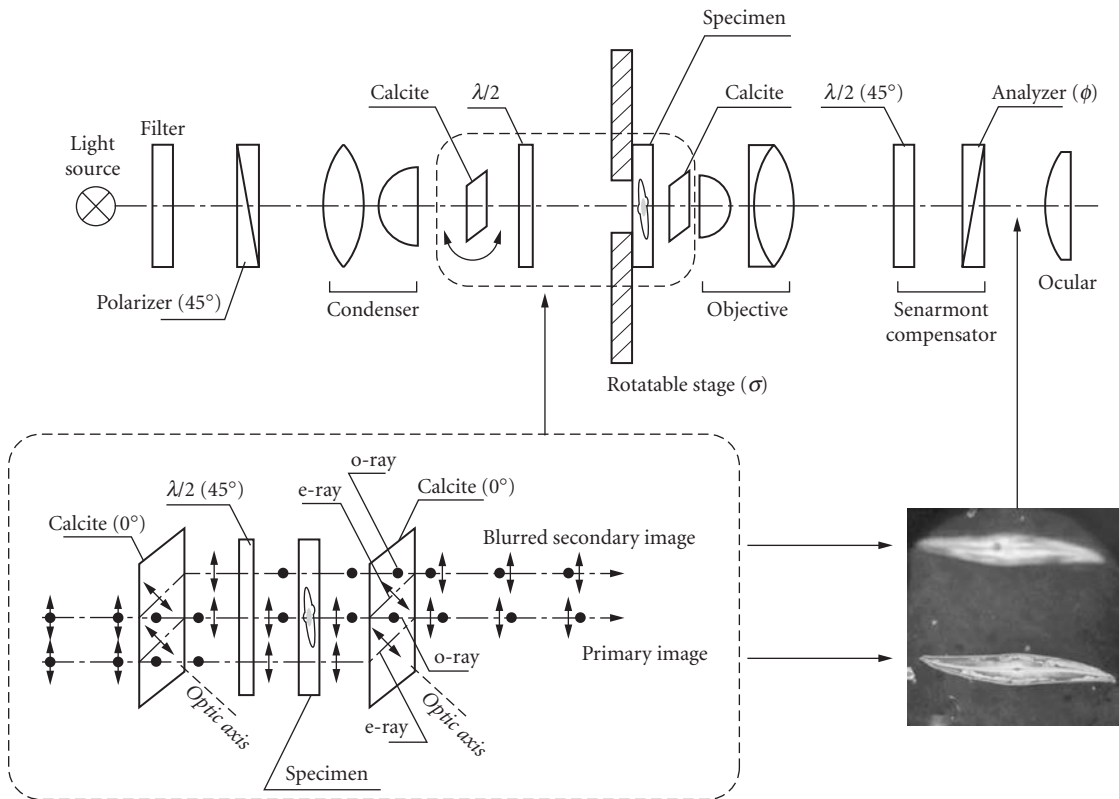


FIGURE 31 The Jamin-Lebedev type interference microscope.

quarter-wave plates to improve sensitivity and to provide a convenient way of measuring the phase. Its enhanced features include a rotatable polarizer, which is used to balance the intensities of the probe and reference beam. The quarter-wave plates following the beam splitter create circularly polarized light, which is reflected by the specimen/reference surface. The reflection induces an inversion of the circularity of the two beams, which causes them to be combined after the beam splitter in the arm with the Senarmont compensator and ocular. The compensator consists of a quarter-wave plate at azimuth 45° and a rotatable analyzer at azimuth ϕ . Image regions with different phase angles can be brought to extinction by rotating the analyzer to different angles. The phase difference Φ between two regions with extinction angles ϕ_1 and ϕ_2 is $\Phi = 2(\phi_2 - \phi_1)$. Other compensation schemes can be used, including liquid crystal devices, and a camera can be added for quantitative imaging.

Jamin-Lebedev Interference Microscope The first interference microscope was constructed by Lebedev in 1930⁷¹⁻⁷³ using a beam-shearing design based on the two-beam polarization interference scheme introduced by Jamin in 1868.⁷⁴ The optical scheme of the Jamin-Lebedev interference microscope is shown in Fig. 31.

In this instrument, a small plane-parallel plate of calcite is cut at 45° to the optic axis and cemented to the front of the objective lens. An identical calcite plate is cemented to the front of the condenser, with an additional half-wave plate facing the specimen. The axes of the two calcite plates are parallel, and at 45° to the axes of the half-wave plate. The specimen under investigation is placed between the half-wave plate and the calcite plate fixed to the objective. The plate fixed to the objective

produces the necessary lateral separation between the probe and reference beams in the intermediate image plane of the microscope. Thanks to the calcite and half-wave plate placed next to the condenser, the path difference of the interfering rays does not vary with the inclination of the rays. This compensation permits quite large openings of the substage condenser diaphragm.

In the beam-shearing Jamin-Lebedev microscope, the probe and reference beam travel a common physical path except along the short distance between the two calcite plates. Because of the common path many design criteria, including mechanical stability and duplication of optical components, can be significantly relaxed in this beam shearing microscope, compared to the dual-arm Mach-Zehnder design. The compromise lies in the lateral shear distance between probe and reference beam, which is limited by the field size and the requirement for telecentric paths for both probe and reference beam. Because both, the probe and reference beam pass through the same specimen slide, the observer has to be wary of ghost images introduced by the reference beam.

The design shown in Fig. 30 was manufactured in the 1960s by Carl Zeiss, Oberkochen, West Germany. The calcite plate next to the objective lens can be slightly rotated to align the shear planes of the two calcite plates. An additional calcite plate introduces a bias in the optical path difference adjusted by a small tilt of the plate. The microscope comes with three pairs of matched condenser and objective lenses, with the objectives designated as 10×/0.22NA, 40×/0.65NA, and 100×/1.0NA Oil. Their shear distances are 500, 170, and 50 μm, respectively. Optical path differences of less than one wavelength are measured using monochromatic light and a Senarmont compensator. For measuring higher path differences, white light and a Michel-Levy chart (Fig. 28) can be used.

Differential Interference-Contrast Microscope Differential interference-contrast (DIC) microscopy is used extensively in materials research and the life sciences for observing microscopic particles and structures that are associated with refractive index and thickness changes in the specimen. A DIC microscope is a beam-shearing interferometer in which the reference beam is sheared by only a small amount, generally by less than the diameter of the Airy disk that is associated with the imaging optics. The technique produces a shadow-cast image that displays the local gradients of the optical path length. A region of the specimen where the optical path length increases along a reference direction appears brighter (or darker), while a region where the optical path length decreases appears in reverse contrast. As the gradient of the optical path grows steeper, image contrast is increased. Another important feature of the DIC technique is that it produces effective optical sectioning. This is particularly obvious when high numerical aperture (NA) objectives are used together with high NA condenser illumination. The thin optical section is a consequence of the small shear between the interfering beams, which are appreciably separated only in a thin layer around the focal plane.

The DIC technique was invented by F. H. Smith in 1947.^{75,76} He placed between a pair of polarizers one Wollaston prism at the front focal plane of the condenser and a second one in the back focal plane of the objective lens (Fig. 32). The first Wollaston prism splits the linearly polarized input beam into two orthogonally polarized beams that are separated by a small angle ϵ_1 . The condenser lens converts the angular split in the focal plane into a small spatial shear in the object plane. The objective lens joins the two beams again in the back focal plane where the second Wollaston prism deviates the beams to form two parallel beams again. While parallel, the two beams are orthogonally polarized and therefore cannot interfere. Therefore, a linear analyzer is needed after the second Wollaston prism to create a common polarization and to enable the beams to interfere. The interference generates the typical relief image representing the optical path gradients in the specimen (see inset in Fig. 32).

The small angular split ϵ_1 and ϵ_2 in the condenser and objective focal planes are related to the shear amount d in the object plane and the focal lengths of the condenser (f_c) and objective (f_{ob}) lenses by

$$f_c \epsilon_1 = f_{ob} \epsilon_2 = d \quad (15)$$

This optical configuration creates a polarizing shearing interferometer, by which one visualizes optical path gradients of the specimen under investigation.

In conventional medium- to high-NA objective lenses, the back focal plane is located inside the lens system and therefore not available for insertion of a Wollaston prism. If the Wollaston prism

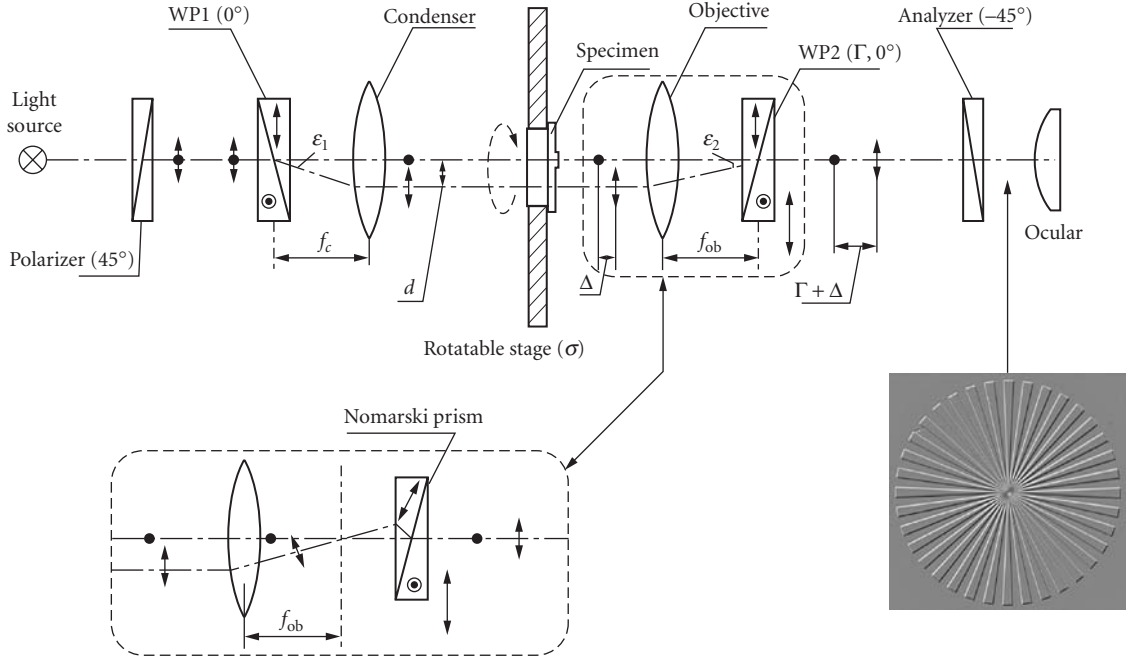


FIGURE 32 DIC microscope setup: polarizer at 45° azimuth; WP1: first Wollaston prism at 0° azimuth; ϵ_1 : splitting angle; f_c : condenser lens focal distance; d : shear amount; Δ : optical path difference introduced by specimen under investigation; σ : azimuth of rotatable stage; f_{ob} : objective lens focal distance; WP2: second Wollaston prism at 0° azimuth (the second prism introduces bias Γ); ϵ_2 : splitting angle; analyzer at -45° azimuth; Wollaston prism can be replaced by Nomarski prism.

is placed far from the back focal plane, the prism produces parallel beams, but the beams are spatially displaced and hence are not recombined. Therefore, the Smith DIC system requires specially designed objective lenses that allow the insertion of a Wollaston prism.

In 1952 G. Nomarski proposed a special prism, the Nomarski prism, which simultaneously introduced spatial displacement and angular deviation of two orthogonally polarized beams^{77,78} (see inset in Fig. 31). The prism can therefore be placed outside the objective lens. By using crystal wedges with appropriately oriented axes, the Nomarski prism recombines the two beams that were separated by the condenser Wollaston prism, as though a regular Wollaston prism were located in the back aperture plane of the objective lens. The Nomarski DIC scheme can therefore be used with regular high NA microscope objectives.

A DIC image can be modeled as the superposition of one image over an identical copy that is displaced by a small amount d and phase shifted by a bias Γ . The intensity distribution $I(x, y)$ of the combined image depends on the specimen orientation and varies proportionally with the cosine of the angle between the gradients azimuth θ and the relative direction of wavefront shear σ :⁷⁹

$$I(x, y) = \frac{1}{2} I_0 \left(1 - \cos \left(\frac{2\pi}{\lambda} (\Gamma + \gamma(x, y) d \cos(\theta(x, y) - \sigma)) \right) \right) \quad (16)$$

where I_0 is the initial beam intensity, $\gamma(x, y)$ and $\theta(x, y)$ are the gradient magnitude and azimuth. (For a theoretical framework of DIC imaging see Refs. 8, 79–81.)

Thus, regular DIC techniques show the two-dimensional distribution of optical path or phase gradients projected onto the shear direction. It is therefore prudent to examine unknown objects at several azimuth orientations.

Video-enhanced DIC (VE-DIC), in addition to providing images with improved contrast, allows the removal of unwanted background signal (such as shading and fixed image noise due to dust particles or other imperfections in the optical system) by subtraction of a reference image with no specimen.⁸² Salmon and Tran gave a comprehensive description of the VE-DIC method.⁸³ They indicate that the best optical contrast of microscopic, lowly refractile particles can be achieved with a bias of 1/15–1/20 the wavelength.

A further increase in sensitivity and sectioning capability was achieved by video-enhanced DIC microscopy with retardation modulation.^{84–87} By switching the polarization of the incident light in alternate video frames with a computer-controlled liquid crystal variable retarder, the contrast signal is increased by a factor of 2, relative to “standard” video-enhanced DIC. The modulator switches image highlights into shadows and vice versa. By subtracting alternate frames, a difference DIC image is created in which contrast is doubled while image defects and noise tend to be cancelled.

Recently, Carl Zeiss introduced a “C-DIC” technique for reflective-type microscopes, which avoids the need to rotate the specimen. Instead, the new system uses a single, mechanically rotatable Nomarski prism that is shared between the illumination and imaging path.⁸⁸

Even in a transmission-type microscope one can obtain a DIC image using only one Wollaston or Nomarski prism placed in the imaging path, if the illumination beam is made spatially coherent. Pluta described a DIC setup with a slit condenser diaphragm.⁸ A similar system is currently manufactured by Carl Zeiss called a “PlasDIC.” In the latter case the specimen is illuminated with unpolarized light using a condenser that has a slit in its aperture plane. Only a single polarizer is used and placed behind the Nomarski prism that follows the objective. The system is less sensitive to birefringence of the specimen, can be used with plastic dishes, and does not require strain-free optics. Disadvantages include a reduced illumination intensity caused by the slit (instead of a fully open aperture) and a deterioration of the optical sectioning capability.

The contrast in DIC images is proportional to the scalar product between the phase gradient in the specimen and the shear generated in the microscope’s prisms. Based on the phase gradient it is possible to restore the phase information using computational methods. The restored phase image shows the refractive index (dry mass) distribution within a thin layer of the specimen. Compared to a conventional phase-contrast image, the DIC-based phase image provides better sectioning due to the intrinsic sectioning capability of the DIC method.

The DIC phase image can be obtained by computing the line integral parallel to the shear direction.^{79,89} Other techniques use iterative phase computation,⁹⁰ noniterative Fourier phase integration,⁹¹ or nonlinear optimization using hierarchical representations.⁹² Axelrod et al. used two phase-shifted DIC images to reconstruct the phase based on linearized expressions of interference.⁹³ Biggs developed an iterative deconvolution approach for computation of phase images, based on the same principles as deconvolution techniques normally used to remove out-of-focus haze.⁹⁴

Dyson and Mirau Interference Microscopes A third group of interference microscopes, in which the reference wave is focused to a different level than the specimen plane, are represented by the Dyson and Mirau interference microscopes.

In 1950, J. Dyson designed a double-focus system for transmitted light (Fig. 33a).⁹⁵ In this system, the initial transparent beam-dividing surface is formed on the upper side of the first glass plate mounted normally to the optical axis of the microscope immediately beneath the specimen slide. The illuminating beam, convergently directed through this upper surface by the substage condenser, is then partially reflected back to the lower surface of the plate, which has a small opaquely silvered, reflecting central spot. The lower surface of the first plate therefore reflects this second beam back through the upper surface of the plate. As a result, the specimen area is illuminated by two beams, one of which is focused on the specimen after direct transmission through the plate while the other reaches the specimen in a defocused condition due to internal reflection within the plate. A similar plate between the specimen and the objective lens functions in much the same way, so that the portion of the second defocused beam, which passes directly through it becomes combined with a portion of the first focused beam internally reflected within it.

The image formed by the microscope objective consequently consists of a correctly focused image of the specimen area seen in interferometric comparison with a strongly defocused image of it.

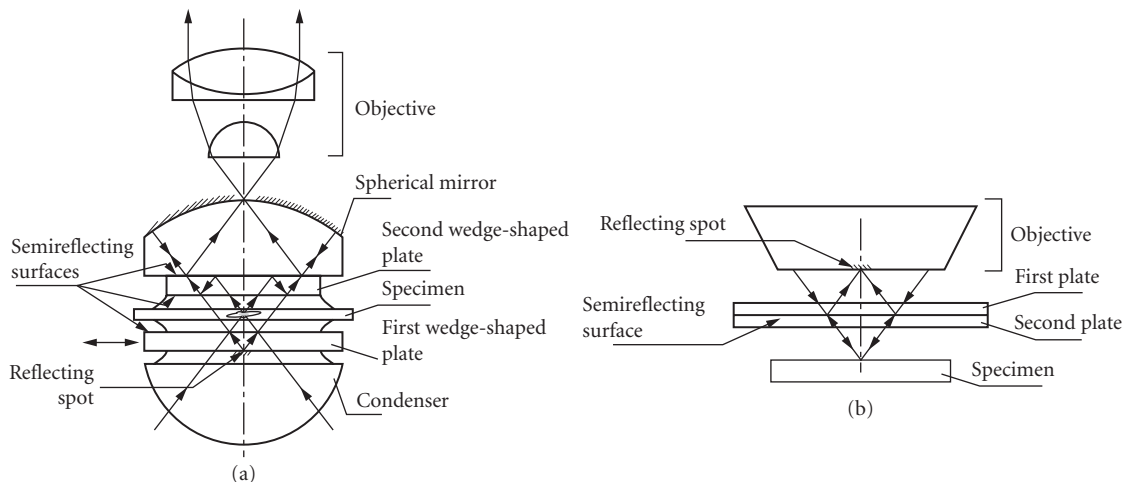


FIGURE 33 (a) Dyson and (b) Mirau's interference microscope. In (b), the incident light beam, emerging from the objective O_1 , is split in two parts in the semireflective surface. One part is transmitted to the object P and the other is reflected to the reference area R extending over a small portion of the objective front surface. The wavefronts reflected by R and P are recombined at G to produce the interference pattern.⁵

A glass block with an upper spherical surface, which is fully reflecting apart from a central totally transmitting spot is included between the second plate and the objective to allow medium- and high-power objective lenses to focus through to the specimen. The two plates are made slightly wedge-shaped so that the optical path difference can be manually adjusted by traversing the condenser plate in a direction parallel to the principal section of the wedge across the optical axis of the microscope. This operation varies the effective thickness difference between the two plates and thereby controls the optical path difference. By calibrating this movement the optical path difference can be determined.

Mirau introduced a single objective reflecting system.⁹⁶ In this design (Fig. 33b) a flat, semireflecting beam-dividing surface is placed midway between the front of the objective and the specimen surface. A small central area of the front surface of the objective is silvered to form a miniature mirror, a reflected image of which becomes superimposed on the normal image of the specimen surface by virtue of the intervening semireflecting beam divider. To maintain the required degree of optical path similarity, the beam-dividing surface is formed on the internal side of one of a pair of identical plates, which are cemented together.

Holographic Soon after its invention the laser was employed for holographic imaging in microscopy. In the early 1960s, Gordon Ellis built one of the first holographic microscopes.⁹⁷ He used a helium-neon laser as light source and photographic film for recording the hologram. After development of the film, the hologram allowed to reconstruct images using a divergent laser beam.

In digital holographic microscopy (DHM), the hologram of interfering wave fronts is recorded with an electronic sensor (e.g. CCD chip, Fig. 34)⁹⁸ and images are digitally reconstructed by a computer. A digitized hologram represents a three-dimensional record of the optical features of the specimen. Based on a single hologram, several images can be reconstructed that correspond to specific focus planes in the specimen. Furthermore, the digital reconstruction allows to simulate different contrast modes, such as phase contrast and dark field imaging.^{99–101} In addition to the specimen, the hologram can also contain information on the rest of the optical path, depending on the coherence length of the light source. For example, a hologram can provide the opportunity to correct for lens aberrations.¹⁰²

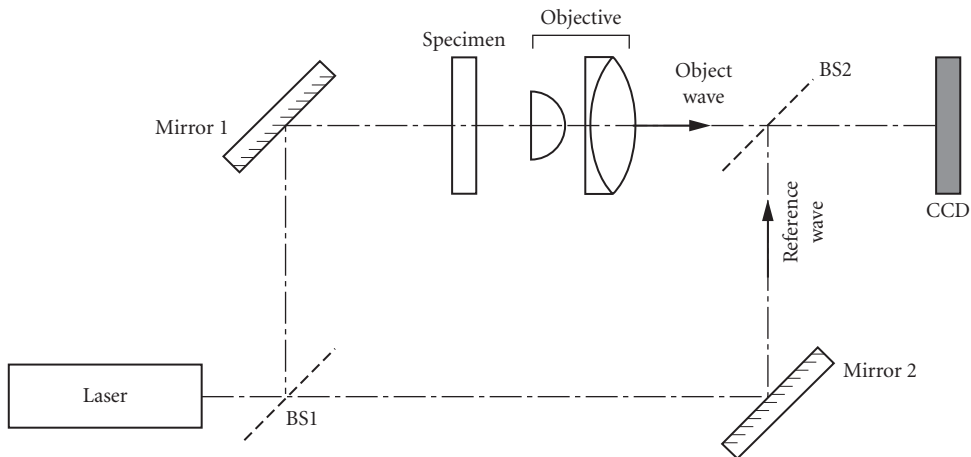


FIGURE 34 Optical principle of a holographic microscope. A collimated laser beam is divided by the beamsplitter BS1. One beam passes through the specimen and the microscope objective lens and forms the object wave. The second beam is the reference wave and is recombined on-axis with the first beam behind the objective lens. The interference pattern (hologram) of the object and reference wave is recorded by a CCD camera that is located near a conjugate plane of the backfocal plane of the objective lens. Other optical setups are possible, including for reflective-type specimens and for using an off-axis interference arrangement.⁹⁸

The digital analysis of a set of holograms, each recorded with a beam that illuminates the sample from a different direction, allows to emulate an objective with a larger numerical aperture than actually employed, leading to a corresponding enhancement in image resolution.¹⁰³

Optical Coherence Tomography Optical coherence tomography (OCT) is an imaging method that performs depth-resolved imaging of various turbid media. At the core of the OCT technique is a low-coherence, two-arm interferometer, which works in reflection mode.^{104,105} The low-coherence interferometer is used to select only a small volume named the “coherence gate” that determines the depth in the sample from where the back-reflected or back-scattered signal is processed. The depth of the coherence gate is defined and controlled by matching the optical path in the probe and reference interferometer arms. A variable delay line in one of the arms changes the gate position. In addition to its depth-selectivity feature, the low coherence interferometer is used to “amplify” very weak signals back-scattered by the sample.

In OCT, the coherence length is shortened to a distance of several micrometers, thanks to the use of a broadband light source. Light of appropriate bandwidth is typically generated by a superluminescent diode or laser with extremely short pulses. The spatial resolution of OCT in the axial direction is provided by the coherence gate, which selects signal light only from a cross-sectional volume of thickness defined by the coherence length of the illumination source. Superluminescent diodes typically provide 10- to 20- μm axial resolution. Higher resolution can be obtained with ultrashort pulsed lasers.

Interference of the light reflected by the sample and the reference mirror in the interferometer arms can occur only when the optical path lengths of the two arms match to within the coherence length of the optical source. Depth scanning can be performed in the time- or spectral domain. Time-domain OCT systems vary the reference arm path length, inducing changes in the depth from which the backscattered light of the sample is detected. In spectral-domain or Fourier-domain OCT, the axial signal intensity is calculated based on changes in the interference spectrum. The interference between probe and reference beam causes changes in the spectrum which is measured using a suitable spectrometer,¹⁰⁶ or by rapidly and repeatedly sweeping a narrow line width laser source in a mode called swept-source OCT.^{106–108}

In addition to amplitude and phase, OCT can also be used to analyze changes in polarization of the probe beam, revealing the polarization properties (birefringence, dichroism) of selected regions inside a turbid medium.¹⁰⁹

Optical coherence microscopy (OCM) combines the advantages of confocal microscopy with the principles of low-coherence interferometry.^{104,110,111} High contrast and detection sensitivity are achieved via rejection of out-of-focus light, resulting in improved optical sectioning capabilities deep within highly scattering media. Both OCT and OCM usually employ single-mode optical fibers for illuminating and collecting light from the sample. However, OCT uses a low NA objective lens with an extended depth of field, providing sectioning through coherence only. OCM, on the other hand, utilizes a high NA lens, providing sectioning through a combination of coherence and confocal effects.

Polarizing

The polarizing microscope (Fig. 35) generally differs from a standard transilluminating microscope by the addition of a polarizer before the condenser; a compensator slot and analyzer behind the objective lens; strain-free optics; a graduated, revolving stage; centrable lens mounts; cross-hairs in the ocular aligned parallel or at 45° to the polarizer axes; and a focusable Bertrand lens that can be inserted for conoscopic observation of interference patterns in the back aperture of the objective lens. In addition, the front element of the condenser can be swung into place for higher-NA conoscopic observations or swung out for low-NA orthoscopic observations of larger field areas.

The same components can be made to fit on an epi-illumination stand for observing opaque or reflective-type samples, such as in metallurgy. As outlined earlier, in epi-illumination a beam-splitting mirror separates the illumination and imaging light paths before the objective lens. In polarizing microscopy one needs to pay special attention to the beam-splitting mirror, which typically introduces polarization aberrations. The aberrations can be significantly reduced by a so-called Smith reflector replacing the regular dichromatic or half-shaded mirror. While a regular beam splitter reflects the incoming beam with a 45° angle of incidence, the Smith reflector uses two 22.5° reflections, first off a full mirror, followed by a second reflection off a 50/50 beam splitter. While the number of reflections has doubled, the steeper angle of incidence of 22.5° for both reflections reduces the overall polarization distortions compared to a regular beam splitter.

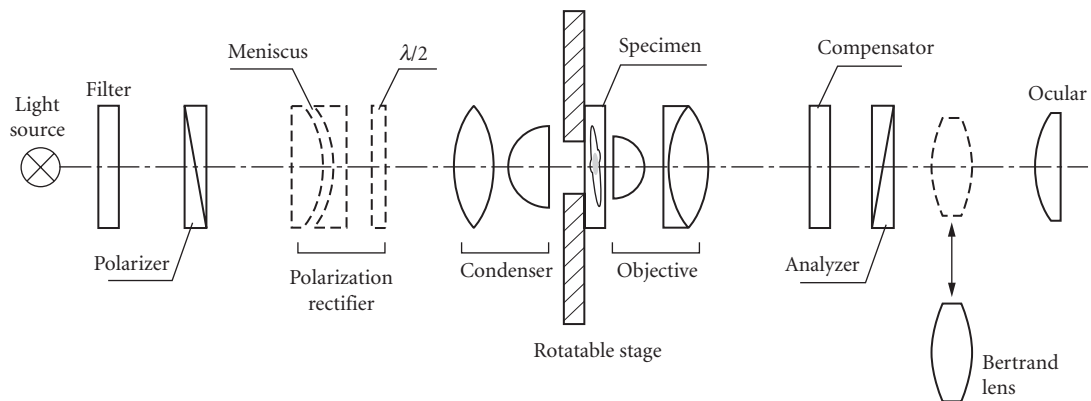


FIGURE 35 Optical train of a polarized light microscope with polarizer, analyzer, and compensator. An optional polarization rectifier can achieve improved sensitivity for low retardance measurements. With an optional Bertrand lens one examines the objective back focal plane for conoscopic interference figures.

Equipped with these standard components, the polarizing microscope represents a powerful analytical tool for the identification of crystals, fibers, and other optically anisotropic materials.^{51,68} With standard polarizing microscopes, one can image and measure polarization optical parameters on objects which are larger than a few micrometers and which introduce retardance values greater than several tens of nanometers. However, as the dimension of the object or magnitude of retardance decrease below these ranges, one needs to use special techniques or devices for detecting and measuring birefringence or even for generating a reliable image with high-NA lenses.

The basic ingredients that are needed to detect low levels of birefringence (retardance ≤ 10 nm) are high-extinction optics, use of low-retardance compensator, light source with high irradiance, and high-sensitivity detector (e.g., dark adaptation for visual observation and measurements). The need for high extinction optics applies to all components of the polarization optical train, which starts and ends with the polarizer and analyzer, respectively, and all optical components placed between them. Most manufacturers carry objective and condenser lenses that are either made or specially selected for polarized light observations. Such objectives typically carry the designation P, PO, or POL on their lens barrel and are designed to induce minimal polarization distortions (see Table 2).

Dichroic polarizing filters have replaced calcite prisms (which introduce astigmatism to all but collimated rays) as polarizer and analyzer in all but the most demanding applications. Modern dichroic polarizers are available with extinction factors better than 1000 and transmission better than 90 percent of the light that is fully polarized parallel to the transmission axis. These specs are satisfactory for most applications, in part because even POL-designated microscope lenses that are placed between the polarizer and analyzer cause polarization distortions that typically reduce the extinction of the polarization optical train significantly below 1000. The polarization distortions are typically caused by stress birefringence in the lens glass and by the differential transmission and phase shift of polarized light that passes through the peripheral regions of highly curved lens surfaces.¹¹² The latter distortions result in four bright quadrants separated by a dark cross (the Maltese cross) that is seen conoscopically for crossed linear polarizers in the absence of a birefringent specimen. These distortions also give rise to anomalous diffraction, based on a four-leaved clover pattern replacing the Airy disk or each weakly birefringent image point.^{113,114}

To counteract polarization distortions that occur at high NA lens surfaces, Inoué and colleagues have introduced polarization rectifiers^{115,116} made of a zero power lens with meniscus and a half-wave plate (Fig. 35). Using rectified optics Inoué and Sato¹¹⁷ were able to reveal the chromosome arrangement in living sperm based on high-contrast polarized light images (Fig. 36). Unfortunately, rectifiers are commercially not available for modern microscope objectives, which contain many lens elements and complex antireflection coatings, making the construction of a rectifier highly specific to each objective and condenser lens. However, some manufacturers have succeeded better than others in selecting antireflection coatings that minimize the polarization distortions. Therefore, it is advisable to carefully select microscope optics, testing the polarization performance of similar lenses from several manufacturers and even within the product range of the same manufacturer, before acquiring critical components.

The compensator is located between the polarizer and analyzer, either before or after the specimen. There are several types of compensators (often named after their inventors), which are typically made of birefringent plates or wedges that can be translated or rotated in fine increments while observing the specimen.¹¹⁸ The effect of the compensator on the polarization of the transmitted or reflected light either adds to or subtracts from (compensates) the effect caused by the specimen. While not absolutely necessary for some basic observations, the compensator (a) can significantly improve the detection and visibility of weakly birefringent objects, (b) is required to determine the slow and fast axis of specimen birefringence, and (c) is an indispensable tool for the quantitative measurement of object birefringence (see, e.g., Ref. 119); for a discussion of the Poincaré sphere as an analogue device to compute the effect of compensators, or of birefringent objects in general, on polarized light see Ref. 120).

Over the years several schemes have been proposed to automate the measurement process and exploit more fully the analytical power of the polarizing microscope. These schemes invariably involve the traditional compensator, which is either moved under computer control¹²¹ or replaced

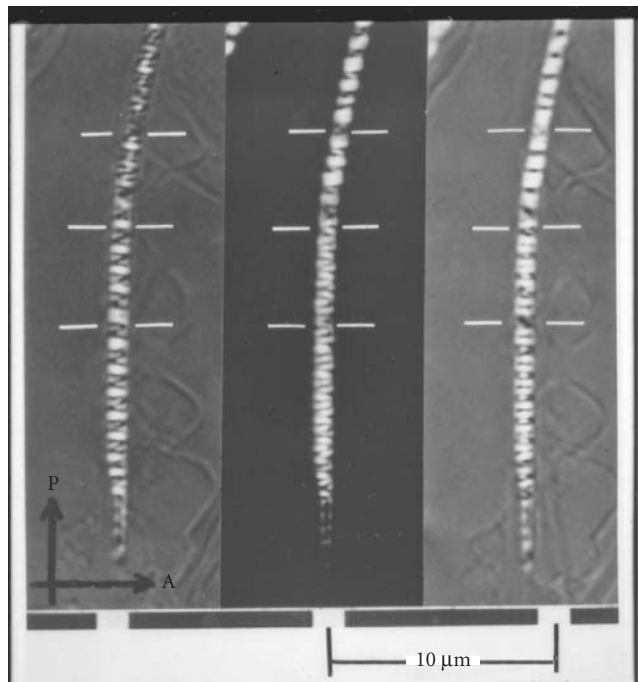


FIGURE 36 Sperm head observed with a rectified polarizing microscope at three different settings of mica compensator. Detailed distribution of birefringence in these chromosomes is shown with great clarity by immersion in dimethyl sulfoxide (refractive index 1.475). White bars: positions of chromosomal “breaks”; probably correspond to the end of each chromosome.¹¹⁷

by electro-optical modulators, such as Pockel-cells,¹²² Faraday rotators,¹²³ and liquid crystal variable retarders.¹²⁴ These schemes also involve quantitative intensity measurements using electronic light detectors, such as photomultipliers or charge-coupled device (CCD) cameras. For strictly quantitative measurements, acquisition and processing algorithms relate measured image intensities and compensator settings to optical characteristics of the specimen (see, e.g., Ref. 125). As an example of a quantitative, high-resolution birefringence map, we show in Fig. 37 the retardance image of a Siemens star that was etched into a thin silica layer.⁵⁰ The image was recorded using the LC-PolScope equipped with a liquid-crystal universal compensator.¹²⁶

Polarized light microscopy is usually practiced in two, mutually exclusive observation modes, called orthoscopy and conoscopy. In orthoscopy, the specimen is viewed directly, while in conoscopy the ocular is replaced by a telescope lens that lets one observe conoscopic interference figures formed in the back focal plane of the objective lens.⁶⁸ In conoscopy, the sample birefringence is measured as a function of the tilt angle of rays passing through the specimen. Hence, this observation mode reveals the inclination angle of the optic axis of a uniformly birefringent specimen region, in addition to the azimuth of the optic axis. In orthoscopy, the inclination angle, which is the angle between the optic axis and the plane of observation, is usually not evident. Recently, orthoscopic and conoscopic views were combined in a single, so-called polarized light field image recorded with a microlens array in the intermediate image plane of an LC-PolScope.²¹

Another approach to measuring the three-dimensional birefringence properties of small birefringent objects uses a so-called universal stage, invented by E.S. Fedorov more than 100 years ago, in

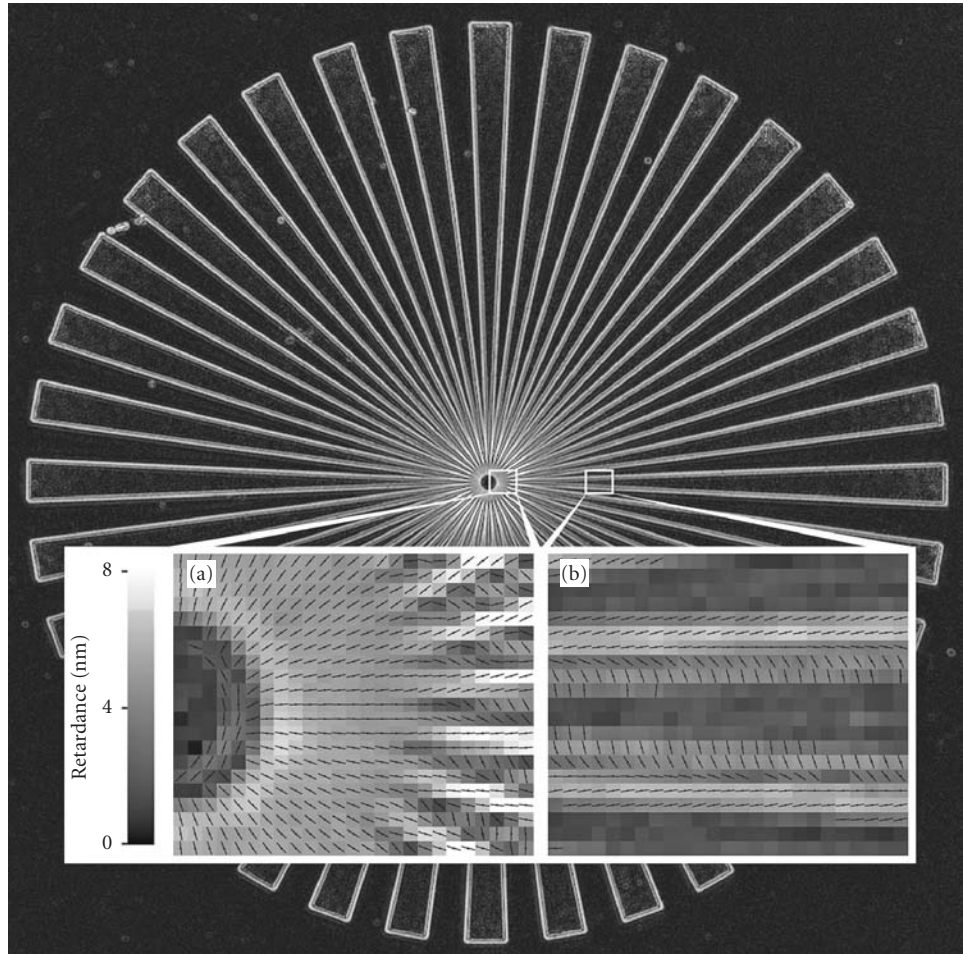


FIGURE 37 Siemens star etched into 90-nm-thick SiO_2 layer and imaged with the LC-PolScope. The dimensions of the star pattern are the same as the one described in Fig. 21. Image brightness is linearly proportional to the retardance measured at all pixel locations. Insets show magnified portions of the pattern with lines indicating the measured slow axis orientation. (a) In the central region birefringence is observed all the way to the inner black disk. Unresolved wedge tips generate form birefringence with the slow axes parallel to the wedge orientations. (b) Edges of a well-resolved wedge portion display edge birefringence, which is composed of two birefringent layers flanking each edge.¹²⁷ ($60\times/1.4$ NA PlanApo oil objective lens and oil condenser with aperture diaphragm reduced to 0.9 NA.)

which the specimen is mounted between two glass hemispheres.²² Rotation of the specimen through measured angles around two or more axes allows one to explore the three-dimensional birefringence patterns of a small specimen region that is located in the common center of rotation. Alternatives to the universal stage include the spindle stage by Bloss¹²⁸ and motorized goniometric stages by Glazer and collaborators.^{129,130}

Instead of rotating the specimen under a stationary optical system, Shribak and Oldenbourg implemented a scheme involving a high numerical aperture imaging system and oblique illumination with varying tilt angle of the illuminating beam.¹³¹ For each angle a high-resolution retardance map

is generated representing the polarization properties of the sample as projected along the tilted axis of illumination. Four such maps, each generated with a different tilt angle, are combined to produce a three-dimensional birefringence map. The system is called *Scanned Aperture LC-PolScope* and is described here in more detail in the section “Aperture Scanning.”

Fluorescence

Fluorescence microscopy is one of the few modes of microscopy in which the illuminating wavelength differs from that of the emitted. In early designs, the exciting waves were prevented from contaminating the fluorescence image by a combination of (1) special illumination (such as the use of a dark-field condenser) that prevented the direct rays from entering the objective lens, and (2) the use of a barrier filter. The barrier filter absorbs the exciting light while transmitting much of the longer fluorescence wavelengths.

Today most fluorescence microscopes (or attachments) use epi-illumination incorporating interchangeable filter cubes (after Ploem, see Fig. 6) that are matched to the fluorochrome. The filter cube is placed in the collimated beam between the objective and a tube lens, at the intersection of the microscope axis and that of the excitation illuminator located on a side arm. The objective lens serves both as the condenser and the objective. A field diaphragm, and sometimes an aperture iris, is placed in the illuminating side arm together with the source collector at appropriate conjugate planes. The illuminating beam, commonly emitted by a xenon or mercury arc lamp, is filtered through a narrow band path interference filter and reflected down into the objective by a dichromatic beam splitter. The fluorescence imaging beam originating from the specimen passes straight through the dichromatic beam splitter and associated barrier filter and reaches the ocular or camera. Each fluorescence cube contains the appropriate excitation interference filter, dichromatic beam splitter, and barrier filter so that they can be switched as a group, for example, to rapidly inspect specimens containing (or stained with) multiple fluorochromes.

For fluorochromes requiring shorter-wave UV excitation, objective lenses must be designed for greater short-wavelength transmission and low autofluorescence. While aberrations for the shorter-UV exciting wavelengths are generally not as well-corrected as for the imaging wavelengths, it should be noted that such aberrations, or lack of parfocality, directly affect the resolution and efficiency in the case of confocal fluorescence microscopes.

Also, it should be noted that, while little effort is commonly made to fill the objective aperture with the illuminating beam (presumably with the rationale that this should not affect image resolution because each fluorescent object is emitting incoherently relative to its close neighbor), one finds that in practice the fluorescent image is much improved by filling the aperture, for example, by use of an optical fiber light scrambler. While the reasons for this improvement are not fully understood, one explanation might lie in the more efficient excitation of randomly oriented fluorophores by a high-NA illumination beam, which excites even those fluorophores that have their linear transition moment aligned parallel to the microscope axis.

While most fluorescence microscopes today use epi-illumination (since epi-illumination provides advantages such as avoiding loss of excitation by self-absorption by underlying fluorochrome layers, generating an image that more closely approximates an intuitive one when reconstructed in three dimensions, etc.), improvements in interference filters open up new opportunities for fluorescence microscopy using transillumination. New interference filters are available with exceptionally high extinction ($>10^5$) and sharp cutoff of the excitation wavelengths, coupled with high transmission of the pass band. With transillumination, one can more reliably combine fluorescence with polarization-based microscopy or carry out polarized fluorescence measurements with greater accuracy, since one can avoid the use of dichromatic beam splitters, which tend to be optically anisotropic.

Fluorescence microscopy particularly benefits from electronic imaging, especially with the use of low-noise, chilled CCDs as imaging detectors, digital computers to enhance and rapidly process the signal (such as in ratio imaging), and the new fluorescence-conjugated chemical probes that provide incredible sensitivity and selectivity.^{11,12,132-135}

For imaging specimens that are labeled with more than two or three types of spectrally distinct fluorophores, a technique known as spectral imaging is becoming available. Spectral imaging combines spectroscopy and imaging, measuring the spectral composition of the light recorded at each point of the image. When spectral imaging is applied to fluorescence microscopy, the filter cube is modified as to transmit a broad range of emission wavelengths. A spectrometer placed before the detector samples the emission spectrum at appropriate resolution and intervals (channels) for wavelengths longer than the excitation wavelength. Spectral imaging systems can either be integrated into the microscope (manufacturers include Leica, Nikon, Zeiss) or can be added to an existing stand (manufacturers include Cambridge Research and Instrumentation Inc., Lightform Inc.). Datasets are typically stored as stacks of images, in which each slice corresponds to a wavelength channel. Powerful algorithms reduce an experimental dataset to indicate for each image point the weighted contributions of pure fluorophores whose spectra are stored in a library.^{136,137}

Confocal Microscopy

In confocal microscopy, the specimen is scanned point by point either by displacing the specimen (stage scanning) or by scanning a minute illuminating spot (beam scanning), generally in a TV-raster fashion. In either case, the scanning spot is an Airy disk formed by a high-NA objective lens. An exit pinhole is placed conjugate to the spot being scanned so that only the light originating from the scanned spot is transmitted through the exit pinhole. Thus, light originating from other regions of the specimen or optical system is prevented from reaching the photo detector (Fig. 38).^{138,139}

This optical arrangement reduces blurring of the image from out-of-focus light scattering, fluorescence, and the like, and yields exceptionally clear, thin optical sections. The optical sections can then be processed and assembled electronically to yield three-dimensional displays or tilted plane projections. Alternatively, the specimen itself can be scanned through a tilted plane (e.g., by implementing a series of x scans with y, z incremented) to yield a section viewed from any desired orientation, including that normal to the microscope axis.

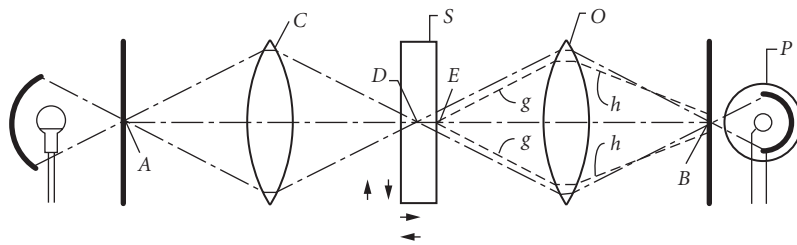


FIGURE 38 Optical path in simple confocal microscope. The condenser lens C forms an image of the first pinhole A onto a confocal spot D in the specimen S . The objective lens O forms an image of D into the second (exit) pinhole B which is confocal with D and A . Another point, such as E in the specimen, would not be focused at A or B , so that the illumination would be less and, in addition, most of the light $g-h$ scattered from E would not pass the exit pinhole. The light reaching the phototube P from E is thus greatly attenuated compared to that from the confocal point D . In addition, the exit pinhole could be made small enough to exclude the diffraction rings in the image of D , so that the resolving power of the microscope is improved. The phototube provides a signal of the light passing through points D_1, D_2, D_3 , etc. (*not shown*), as the specimen is scanned. D_1, D_2, D_3 , etc. can lie in a plane normal to the optical axis of the microscope (as in conventional microscopy), or parallel to it, or at any angle defined by the scanning pattern, so that optical sections can be made at angles tilted from the conventional image plane. Since, in the stage-scanning system, D is a small spot that lies on the axis of the microscope, lenses C and O can be considerably simpler than conventional microscope lenses.^{138,139}

The stage-scanning confocal microscope can yield vastly expanded fields of view. Here the image area is not limited by the field of view of the optics but only by the range of movement of the specimen and ability of the photo detector and processor to handle the vast information generated at high speed. Furthermore, the objective lens needs only to be corrected for a narrow field of view on axis.^{6,138} Laser disk recorders are a form of application that takes advantage of these attributes.

The beam-scanning confocal microscope is typically implemented in the reflective or epi-illumination mode. This mode has the advantage that the illuminating beam and the returning light scattered back by the sample pass through the same objective lens and beam-steering devices needed for scanning the sample. The prototype of a modern beam-scanning confocal microscope uses two galvanometric mirrors (one for each dimension of a two-dimensional image) that scan a focused laser beam across a stationary sample field. The backscattered light is collected by the objective and bounces off the same mirrors which “descan” the returning light before it passes through a stationary beamsplitter (to separate the backscattered light from the incoming beam) and a stationary exit pinhole. The exit pinhole is located in a conjugate image plane, while the scanning mirrors are located in positions that are conjugate to the back focal plane of the objective lens. By (indirectly) placing the mirrors into the objective back focal plane, the angular scan of the mirrors is translated into a positional scan of the focused laser beam in the specimen. Beam-scanning microscopes typically require additional relay optics that project the objective back focal plane into the mirror locations.

The laser-scanning, epi-illuminating confocal microscope was developed into a practical instrument in the late 1980s and immediately adopted with great enthusiasm for fluorescence imaging in the life sciences. Because laser beams are typically highly collimated, a source or entrance pinhole is commonly omitted in this instrument. The beam splitter combining and separating the illumination and imaging paths is implemented as a dichroic (also called dichromatic) mirror providing high reflectivity at short wavelengths and high transmissivity at longer wavelengths (or vice versa, depending on the particular optical design). A whole industry has evolved around designing and manufacturing dichromatic mirrors that are appropriate for specific fluorescent dyes and combination of dyes.

For direct viewing of confocal images in reflective mode a Nipkow disk is used for scanning multiple beams across a stationary sample field. The multiple beams originate in many thousands of pinholes arranged helically on a modified Nipkow disk that is located in the image plane of the objective lens. Thus, a single spinning disk can be made to provide synchronously scanning entrance and exit pinholes.^{140,141} To overcome the considerable light loss associated with the original designs by Petrán and Kino, Yokogawa Electric Corp. employed a second, coaxially aligned Nipkow disk containing microlenses in its CSU-10 disk confocal scanner (Fig. 39). Each pinhole on the first Nipkow disk has a corresponding microlens on the second Nipkow disk that focuses the laser light into the pinhole. Thus, the light efficiency is increased by a factor equal to the ratio of the microlens to pinhole area. Instead of the 1 percent or so found with conventional Nipkow disk systems, some 40 to 60 percent of the light impinging on the disk containing the microlenses becomes transmitted through the pinholes to illuminate the specimen. Accordingly, the CSU-10 provides a light efficient scan unit that permits direct visual viewing of the confocal image, a great advantage when studying moving objects such as living cells.^{142,143}

In a confocal microscope, the exit pinhole can be made smaller than the diameter of the Airy diffraction image formed by the objective lens so that the Airy disk is trimmed down to regions near its central peak. With this optical arrangement, the unit diffraction pattern that makes up the image turns out to be the square of the Airy pattern given in Eq. (2). Thus, the radius at half maximum of the central bright area (Airy disk) is reduced by a factor of 1.36. (The radial position of the first minimum in both patterns is still equal to r_{Airy} .) The shape of the unit diffraction pattern is thus sharpened so that, compared to nonconfocal imaging, two points which radiate incoherently (as in fluorescence microscopy) can be expected to approach each other by up to a factor of $\sqrt{2}$ closer to each other before their diffraction patterns encounter the Rayleigh limit. In Fig. 20 the contrast transfer characteristics of a confocal microscope in the coherent imaging mode is compared with the nonconfocal, incoherent imaging mode using the same lenses. Note that the limiting resolution is the same for both imaging modes, while the contrast transfer of the confocal mode increase more steeply for increasing grating periods.

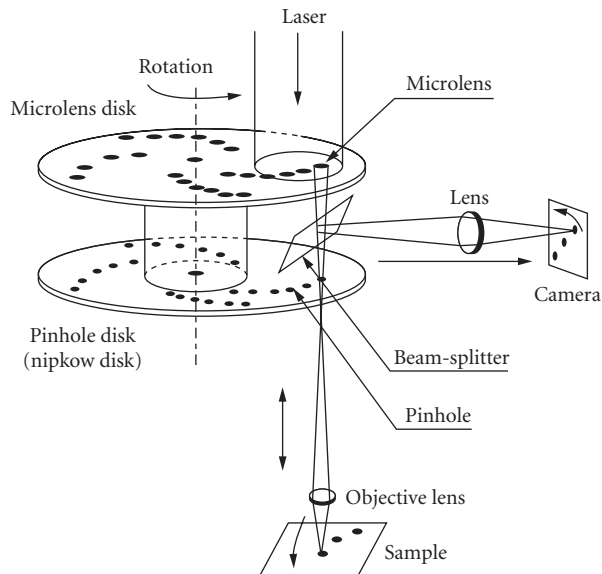


FIGURE 39 Schematic of the Yokogawa CSU-10 confocal disk scanner. The expanded and collimated laser beam illuminates the upper Nipkow disk containing some 20,000 microlenses. Each microlens focuses the laser beam onto its corresponding pinhole, thus significantly raising the fraction of the illuminating beam that is transmitted by the main Nipkow disk containing the pinhole array. The backscattered or fluorescent light is collected by the objective lens and focused back onto the Nipkow disk containing the array of pinholes, which now act as confocal exit pinholes. A beam splitter located between the first and second Nipkow disk reflects the light toward a camera. A lens projects an image of the pinhole array onto the camera, that acquires a confocal image while the Nipkow disk rotates with high speed. After carefully designing the array pattern and implementing a precise and vibration-free rotation of the Nipkow disks, the confocal disk scanner can produce clean, high-resolution images free of fixed pattern noise. In fluorescence imaging, the camera can be replaced by an ocular for direct viewing of the confocal image. (Schematic provided by Yokogawa Electric Corporation.)

Rather than using confocal optics to eliminate image blurring from out-of-focus planes, one can achieve the same end by computational deconvolution of a stack of serial optical sections obtained by wide field microscopy.^{49,144,145} While computationally intensive and time consuming, this image restoration method allows one to isolate clean optical sections from a stack of images that can be acquired at higher speed and higher efficiency than with laser-scanning confocal microscopy and in modes of contrast generation typically not accessible to confocal imaging.

Alternatively, thin optical sections can be obtained directly with digital enhanced video microscopy using high-NA condenser and objective lenses. Requiring little processing, this approach is especially convenient when many stacks of optical sections have to be acquired at high rates in succession, for example in order to record rapid, three-dimensional changes in microscopic domains over time.

Structured Illumination

The quest for improved resolution beyond the diffraction limit has led to the development of several methods that modify the illumination pattern in wide-field microscopy. In standard wide field microscopy, the specimen is illuminated using condenser optics that ideally projects a uniform field of light into the specimen. In structured illumination setups, however, a finely patterned illuminating field is projected into the specimen, providing a means for generating optical sections similar to confocal microscopy and for improving resolution.

Wilson and colleagues¹⁴⁶ first described a simple method of obtaining optical sectioning in a conventional wide-field microscope by projecting a single-spatial-frequency grid pattern onto the object. Images taken at three spatial positions of the grid were processed in real time to produce optically sectioned images that are substantially similar to those obtained with confocal microscopes. The sectioning capability is achieved by superimposing an illumination pattern that is only in focus at a thin section through the specimen, while all other sections of the specimen are illuminated with a more or less blurred version of the pattern. The specimen with the superimposed grid pattern is then imaged with regular wide field optics focused on the grid pattern inside the specimen. Hence, all image features that have the grid pattern imposed on them are located in this specimen section, while image features from other sections of the specimen appear nearly uniformly illuminated. For removing those out-of-focus features and removing the intruding effect of the illumination pattern on the specimen image, three raw sample images are recorded, each with the illumination pattern slightly shifted in position. Subsequently, the raw images are computationally combined to generate an optical section of the sample without the grid pattern noticeable in the image. The company Carl Zeiss has adopted this strategy in its ApoTome slider module for generating optical sections using epi-illumination.

Instead with a regular grid pattern, the sample can also be illuminated with a random speckle pattern to provide depth discrimination in thick, fluorescently labeled tissues.^{147,148} The technique consists of illuminating a sample with a sequence of speckle patterns and displaying the differential intensity variance of the resultant sequence of fluorescence images. The advantage of speckle illumination is that it provides diffraction-limited illumination granularity that is highly contrasted even in scattering media.

Structured illumination strategies that go beyond optical sections and provide lateral resolution that exceeds the classical diffraction limit by a factor of 2 or more have been devised by Gustafsson.¹⁴⁹ The sample is illuminated with a series of excitation light patterns, which cause normally inaccessible high-resolution information to be encoded into the observed image. The recorded images are linearly processed to extract the new information and produce a reconstruction with twice the normal resolution. Unlike confocal microscopy, the resolution improvement is achieved with no need to discard any of the light arriving from the specimen.

In addition to improving the lateral resolution this method can be applied in three dimensions to double the axial as well as the lateral resolution, with true optical sectioning.¹⁵⁰ A grating is used to generate three mutually coherent light beams, which interfere in the specimen to form an illumination pattern that varies both laterally and axially. The spatially structured excitation intensity causes normally unreachable high-resolution information to become encoded into the observed images through spatial frequency mixing. This new information is computationally extracted and used to generate a three-dimensional reconstruction with twice as high resolution, in all three dimensions, as is possible in a conventional wide-field microscope.

Structured illumination is primarily used in fluorescence microscopy, where in principle it is capable of unlimited resolution. To achieve unlimited resolution, structured illumination has to be combined with a nonlinear dependence of the fluorescence emission rate on the illumination intensity.^{151,152} As an example of this concept, Gustafsson experimentally demonstrated saturated structured-illumination microscopy, in which the nonlinearity arises from saturation of the excited state. This method can be used in a simple, wide-field (non-scanning) microscope, which uses only a single, inexpensive laser, and requires no unusual photophysical properties of the fluorophore. The practical resolving power is determined by the signal-to-noise ratio, which in turn is limited by photobleaching. Experimental results show that a two-dimensional point resolution of < 50 nm is possible on sufficiently bright and photostable samples.

Light Field

Instead of increasing resolution in a single image plane, it is sometimes desirable to trade lateral resolution for axial resolution in a three-dimensional image stack. To this end, Marc Levoy and colleagues²⁰ have replaced the regular camera on a standard, wide-field microscope by a camera with microlens array, a so-called light field camera or plenoptic camera.¹⁵³ The array consists of a hundred thousand or more microlenses arranged in a square up to the size of the microscope's field number. The array is placed in the intermediate image plane of the objective lens. Behind the array the sensor chip is located in the backfocal plane of the microlenses. In other words, the light field camera samples the specimen image on a regular grid at intervals that corresponds to the pitch of the microlens array. At each grid point the camera captures a small subimage of the objective's back focal plane. Hence, the camera captures a hybrid image of the specimen that is sampled not only in space but also along different directions through the specimen.

The raw light field image, when presented to the eye, cannot be directly interpreted since it consists of a multitude of small disk-shaped images (of the objective's back focal plane) arranged on a regular grid. However, a single light field image is used to reconstruct a multitude of conventional images of a specimen that is viewed along different directions or focused to different object planes.²⁰ These differing views are all based on a single light field image that was captured by a single camera exposure. Hence light field microscopy can be especially useful when imaging three-dimensional structures that change rapidly in time, such as living cells and tissues. Based on a single snapshot one can reconstruct a stack of optical sections that were all recorded at the same point in time, thus avoiding registration problems between sections.

However, the versatility of generating different views and optical sections from a single light field image comes at a price. The sacrifice one makes is a reduction in image size. Specifically, if each microlens subimage contains $N \times N$ pixels, then the computed images will contain N^2 fewer pixels than if the microlenses were not present. In return, we can compute N^2 unique oblique views of the specimen, and we can generate a focal stack containing N slices with nonoverlapping depths of field.²⁰

The recording of light field images is compatible with several contrast modes, including fluorescence and polarized light microscopy. One of the first areas to take advantage of simultaneous optical sections was fluorescence microscopy of functional neuronal tissues and the recording of three-dimensional excitation patterns. In polarized light field microscopy, the microlens array generates a hybrid image consisting of an array of small conoscopic images, each sampling a different object area.²¹ Analysis of the array of conoscopic images reveals the birefringence of each object area as a function of the propagation direction of transmitted light rays. Compared to traditional conoscopy and related methods, the vastly improved throughput and quantitative analysis afforded by the light field LC-PolScope, for example, make it the instrument of choice for measuring three-dimensional birefringence parameters of complex structures. Since light field microscopy was implemented only a few years ago, additional application areas of this new method are likely to emerge in the future.

Aperture Scanning

In the aperture-scanning microscope devised by Ellis for phase-contrast microscopy, the tip of a flexible signal optical fiber, illuminated by an Hg arc, makes rapid circular sweeps at the periphery of the condenser aperture.⁶⁵ This circular, scanning illumination spot replaces the conventional phase annulus in the condenser aperture plane. A quarter-wave plate and absorber, both covering only a small area conjugate to the illuminating spot, spins in synchrony with the fiber at the objective back aperture (or its projected conjugate). Thus, the specimen is illuminated by a narrow, coherent beam that enters the specimen obliquely at high NA, with the azimuth orientation of the beam swinging around and around to generate a full cone of illumination within the integration time of the detector. With this aperture-scanning approach, the specimen is illuminated by a large-NA cone of light which is temporally incoherent, with the phase disk covering only a small fraction of the area normally occupied by the phase ring in conventional phase-contrast systems. The small size of the phase

disk, while appropriately reducing the amplitude and introducing the requisite $\lambda/4$ wave phase retardation to the rays not scattered by the specimen, allows the transmission of a much larger fraction of the scattered rays that carry the high spatial frequency information. The aperture-scanning phase-contrast microscope thus provides a very thin optical section. The image is also virtually free of the phase halo that obscures image detail adjacent to refractile boundaries in conventional phase-contrast microscopy.

For polarized light microscopy an aperture scanning scheme was designed and built by Shribak and Oldenbourg using a liquid crystal device in the front focal plane of the condenser lens.^{131,154} The liquid crystal device was designed for two functions: (1) to create oblique illumination of the specimen, and (2) to measure the birefringence parameters of microscopic objects for each of four oblique tilt angles of illumination. By measuring the object retardance along each of the four tilted projections, the inclination angle of the optic axis of birefringent objects was revealed, in addition to the orientation or azimuth angle in the plane of focus. The inclination angle of the optic axis is usually not evident from traditional polarized light images (see section on polarized light).

Extending this concept, modulation of the transfer functions of the condenser and objective apertures with electro-optical devices should open up intriguing new opportunities. Such modulation eliminates the need for mechanical scanning devices, the spatial distribution of the modulation function can be altered at will, and the amplitude and phase of light passing each point in the aperture can be adjusted rapidly, even coupled dynamically to the image signal through a feedback loop to generate dynamic spatial filters that enhance or select desired features in the image.

28.5 MANIPULATION OF SPECIMEN

In addition to viewing microscopic specimens, the light microscope and microscope objectives are also used to project reduced high-intensity images of source patterns into the object plane in order to optically manipulate minute regions of the specimen. Photolithography and laser disk recorders are examples of important industrial applications, which have prompted the design of specially modified objective lenses for such purposes.

Microbeam Irradiation, Ablation

Many applications are also found in the biomedical field, initially using UV-transmitting, moderately high NA objectives that are parfocalized for visible light and UV down to approximately 250 nm (Zeiss Ultrafluor, also quartz monochromats from Leitz). In its extreme form, a concentrated image of a circular- or slit-shaped UV or laser source of selected wavelengths is imaged onto a biological specimen to locally ablate a small targeted organelle; for example, a part of a chromosome, the microtubules attached thereto, or tiny segments of cross-striated muscle, are irradiated with the microbeam in order to sever their mechanical connections and, for example, to analyze force transduction mechanisms.^{155,156} In other cases, oriented chromophores can be selectively altered at the submolecular level, for example, by polarized UV microbeam irradiation. The stacking arrangement of the DNA nucleotide bases (which exhibit a strong UV dichroism, as well as birefringence in visible light) can be selectively altered and disclose the coiling arrangement of DNA molecules within each diffraction-limited spot in the nucleus of living sperm.¹¹⁷ Brief microirradiation of slit- or grid-shaped patterns of UV are used to bleach fluorescent dyes incorporated into membranes of living cells. The time course of recovery of fluorescence into the bleached zone measures the rate of diffusion of the fluorescently tagged molecules in the membrane and reveals unexpected mobility patterns of cell membrane components.^{157,158}

Lasers have become the dominant source for microbeam irradiation experiments in cell and developmental biology and in other application areas. Laser sources can have a wide range of tunable wavelengths (217 to 800 nm), energies, and exposure durations (down to 25×10^{-12}).¹⁵⁹ They are often used together with sensitizing dyes or fluorescent markers to target specific organelles.¹⁶⁰ They can be used in conjunction with versatile beam-shaping optics such as spatial light modulators.¹⁶¹

Photosensitive and Caged Compounds

Selected target molecules within minute regions in living cells can be modified, tagged, or activated by focused beams of light. The target molecules can be naturally photosensitive species such as chlorophyll (which produces oxygen where illuminated with the appropriate visible wavelengths), rhodopsin (which isomerizes and triggers the release of calcium ions and action potentials in retinal cells), or artificially introduced photosensitive reagents such as the drug colchicine (whose antimetabolic activity is abolished locally with 366-nm irradiation).

Of the photosensitive compounds, the *caged compounds* have a far-reaching potential. These are compounds that are synthesized so as to “cage” and hide the active chemical group until a photosensitive part of the compound is altered (e.g., by long-wavelength UV irradiation) and unmasks the hidden active group. Thus, by preloading with the appropriate caged compound and irradiating the cell selectively in the region of interest, one can test the role of the uncaged compound. For example, the role of ATP can be tested using caged ATP and ATP analogs; response to subtle increase in calcium ions can be seen using caged calcium or caged calcium chelators.^{162,163} Likewise, caged fluorescent dyes are irradiated to locally label and follow the transport of subunits within macromolecular filaments in a dividing cell.¹⁶⁴ Caged glutamate in brain slices was photolyzed using a holographically generated illumination pattern for simultaneous multispot activation of different dendrites.¹⁶¹

Optical Tweezers

Intense laser beams concentrated into a diffraction spot can generate a photon-driven force great enough to capture and suspend small particles whose refractive index differs from its surrounding.^{165,166} Applied to microscopy, a single swimming bacterium or micrometer-sized organelles in live cells can be trapped and moved about at will at the focus of a near-infrared laser beam focused by an objective lens of high NA. While the energy density concentrated at the laser focus is very high, the temperature of the trapped object remains within a degree or so of its environment; biological targets typically exhibit low absorbance at near-infrared wavelengths and thermal diffusion through water from such minute bodies turns out to be highly effective. Thus, the bacterium continues to multiply while still trapped in the focused spot, and it swims away freely when the laser beam is interrupted.

The ability to use “optical tweezers,” not only to capture and move about minute objects but to be able to instantly release the object, provides the microscopist with a unique form of noninvasive, quick-release micromanipulator.¹⁶⁷

Optical tweezers are now being used in the investigation of an increasing number of biochemical and biophysical processes, from the basic mechanical properties of biological polymers to the multitude of molecular machines that drive the internal dynamics of the cell. Innovation continues in all areas of instrumentation and technique, with much of this work focusing on the refinement of established methods and on the integration of this tool with other forms of single-molecule manipulation or detection. These developments have important implications for the expanded use of optical tweezers in biochemical research.¹⁶⁸

28.6 ACKNOWLEDGMENTS

Shinya Inoué was the principal author of the chapter on microscopes in the previous edition of the *Handbook of Optics*. The authors wish to thank Dr. Inoué for his many suggestions regarding the reorganization of the content, for a new contribution on the single-sideband edge enhancement (SSEE) technique, and for his consent to use much of the previous text and figures for the new edition. In acknowledging contributions to both editions, the authors also wish to thank Gordon W. Ellis of the University of Pennsylvania, late Katsuji Rikukawa, Yoshiyuki Shimizu, and Hiroohei Takenaka from Nikon K. K., Japan, Ernst Keller and Rudi Rottenfusser of Carl Zeiss, Inc., Jan Hinsch

of Leica, Inc., Mortimer Abramovitz of Olympus, Inc., and Lee Shuett and Mel Brenner of Nikon, Inc., who all provided helpful information and insights into microscope design.

The preparation of this chapter was supported in part by the National Institutes of Health grants R01 EB002583 awarded to R.O. and R01 EB005710 awarded to M.S.

28.7 REFERENCES

1. L. C. Martin, (1966) *The Theory of the Microscope*, Blackie, London.
2. S. Inoué and K. R. Spring, (1997) *Video Microscopy the Fundamentals*, Plenum Press, New York.
3. F. Zernike, (1942) "Phase Contrast, a New Method for the Microscopic Observation of Transparent Objects," *Physica* **9**:686–693.
4. D. Gabor, (1949) "Microscopy by Reconstructed Wavefronts," *Proc. Roy. Soc. London ser A* **197**:454–487.
5. M. Françon, (1961) *Progress in Microscopy*, Row, Peterson, Evanston, Ill.
6. T. Wilson and C. Sheppard, (1984) *Theory and Practice of Scanning Optical Microscopy*, Academic Press, London.
7. M. Pluta, (1988) *Advanced Light Microscopy Vol. I: Principles and Basic Properties*, Elsevier Science Publishing Co., Amsterdam.
8. M. Pluta, (1989a) *Advanced Light Microscopy Vol. II: Specialized Methods*, Elsevier Science Publishing Co., Amsterdam.
9. M. Pluta, (1993) *Advanced Light Microscopy Vol. III: Measuring Techniques*, Elsevier Science Publishing Co., Amsterdam.
10. G. Sluder and D. E. Wolf, (1998) Video Microscopy. In: *Methods Cell Biol.* (eds. L. Wilson and P. Matsudaira). Academic Press, San Diego.
11. Y.-L. Wang and D. L. Taylor, (1989) *Fluorescence Microscopy of Living Cells in Culture. Part A*, Academic Press, San Diego.
12. D. L. Taylor and Y.-L. Wang, (1989) *Fluorescence Microscopy of Living Cells in Culture. Part B*, Academic Press, San Diego.
13. J. B. Pawley, (2006) *Handbook of Biological Confocal Microscopy*, 3d ed. Springer, New York.
14. B. R. Masters and P. T. C. So, (2008) *Handbook of Biomedical Nonlinear Optical Microscopy*, Oxford University Press, Oxford.
15. S. Bradbury, P. J. Evennett, H. Haselmann and H. Piller, (1989) *Dictionary of Light Microscopy*, Oxford University Press, Oxford.
16. H. H. Hopkins and P. M. Barham, (1950) "The Influence of the Condenser on Microscopic Resolution," *Proc. Phys. Soc. London* **63 B**:737–744.
17. M. Born and E. Wolf, (2002) *Principles of Optics: Electromagnetic Theory of Propagation, Interference and Diffraction of Light*, Cambridge University Press, Cambridge.
18. G. W. Ellis, (1985) "Microscope Illuminator with Fiber Optic Source Integrator," *J. Cell Biol.* **101**:83a.
19. E. Becker, (1985) *Fluorescence Microscopy*, Ernst Leitz Wetzlar GmbH, Wetzlar, Germany.
20. M. Levoy, R. Ng, A. Adams, M. Footer and M. Horowitz, (2006) "Light Field Microscopy," *Acm. T. Graphic* **25**:924–934.
21. R. Oldenbourg, (2008) "Polarized Light Field Microscopy: An Analytical Method Using a Microlens Array to Simultaneously Capture both Conoscopic and Orthoscopic Views of Birefringent Objects," *J. Microsc.* **231**:419–432.
22. N. H. Hartshorne and A. Stuart, (1964) *Practical Optical Crystallography*, American Elsevier Publishing Co., Inc., New York, NY.
23. H. E. Keller, (1995) Objective Lenses for Confocal Microscopy. In: *Handbook of Biological Confocal Microscopy* (ed. J. B. Pawley). 2d ed. Plenum Publ. Corp., New York.
24. Y. Shimizu and H. Takenaka, (1994) "Microscope Objective Design," *Adv. Opt. Electron Microsc.* **14**:249–334.
25. R. Kingslake, (1978) *Lens Design Fundamentals*, Academic Press, San Diego.

26. E. Hecht, (2002) *Optics*, Pearson/Addison-Wesley, San Francisco, CA.
27. L. W. Smith and H. Osterberg, (1961) "Diffraction Images of Circular Self-Radiant Disks," *J. Opt. Soc. Am.* **51**:412–414.
28. M. Cagnet, M. Françon and J. C. Thrierr, (1962) *Atlas of Optical Phenomena*, Springer Verlag, Berlin.
29. E. H. Linfoot and E. Wolf (1956) "Phase Distribution Near Focus in an Aberration-Free Diffraction Image," *Proc. Phys. Soc.* **B69**:823–832.
30. S. Inoué, (1989) Imaging of Unresolved Objects, Superresolution and Precision of Distance Measurement with Video Microscopy. In: *Methods Cell Biol.* (eds. D. L. Taylor and Y.-L. Wang). Academic Press, New York.
31. R. E. Thompson, D. R. Larson and W. W. Webb, (2002) "Precise Nanometer Localization Analysis for Individual Fluorescent Probes," *Biophys. J.* **82**:2775–2783.
32. R. J. Ober, S. Ram and E. S. Ward, (2004) "Localization Accuracy in Single-Molecule Microscopy," *Biophys. J.* **86**:1185–1200.
33. Y. Garini, B. J. Vermolen and I. T. Young, (2005) "From Micro to Nano: Recent Advances in High-Resolution Microscopy," *Curr. Opin. Biotechnol.* **16**:3–12.
34. S. W. Hell, (2007) "Far-Field Optical Nanoscopy," *Science* **316**:1153–1158.
35. H. Park, E. Toprak and P. R. Selvin, (2007) "Single-Molecule Fluorescence to Study Molecular Motors," *Q. Rev. Biophys.* **40**:87–111.
36. R. Heintzmann and G. Ficz, (2007) "Breaking the Resolution Limit in Light Microscopy," *Methods Cell Biol.* **81**:561–580.
37. A. Yildiz, J. N. Forkey, S. A. McKinney, T. Ha, Y. E. Goldman and P. R. Selvin, (2003) "Myosin V Walks Hand-Over-Hand: Single Fluorophore Imaging with 1.5-nm Localization," *Science* **300**:2061–2065.
38. E. Betzig, G. H. Patterson, R. Sougrat, O. W. Lindwasser, S. Olenych, J. S. Bonifacino, M. W. Davidson, J. Lippincott-Schwartz and H. F. Hess, (2006) "Imaging Intracellular Fluorescent Proteins at Nanometer Resolution," *Science* **313**:1642–1645.
39. M. J. Rust, M. Bates and X. Zhuang, (2006) "Sub-Diffraction-Limit Imaging by Stochastic Optical Reconstruction Microscopy (STORM)," *Nat. Methods* **3**:793–795.
40. L. S. Churchman, Z. Okten, R. S. Rock, J. F. Dawson and J. A. Spudich, (2005) "Single Molecule High-Resolution Colocalization of Cy3 and Cy5 Attached to Macromolecules Measures Intramolecular Distances through Time," *Proc. Natl. Acad. Sci. U S A*, **102**:1419–1423.
41. R. Roy, S. Hohng and T. Ha, (2008) "A Practical Guide to Single-Molecule FRET," *Nat. Methods* **5**:507–516.
42. D. W. Piston and G. J. Kremers, (2007) "Fluorescent Protein FRET: The Good, the Bad and the Ugly," *Trends Biochem. Sci.* **32**:407–414.
43. S. W. Hell and J. Wichmann, (1994) "Breaking the Diffraction Resolution Limit by Stimulated-Emission—Stimulated-Emission-Depletion Fluorescence Microscopy," *Opt. Lett.* **19**:780–782.
44. J. L. Harris, (1964) "Diffraction and Resolving Power," *J. Opt. Soc. Am.* **54**:931–936.
45. E. Betzig, A. Lewis, A. Harootunian, M. Isaacson and E. Kratschmer, (1986) "Near-Field Scanning Optical Microscopy (NSOM); Development and Biophysical Applications," *Biophys. J.* **49**:269–279.
46. H. K. Wickramasinghe, (1989) "Scanned-Probe Microscopes," *Sci. Am.* **261**:98–105.
47. I. T. Young, (1989) Image Fidelity: Characterizing the Imaging Transfer Function. In: *Methods Cell Biol.* (eds. D. L. Taylor and Y.-L. Wang). Academic Press, New York.
48. C. J. Sheppard, (2004) "Defocused Transfer Function for a Partially Coherent Microscope and Application to Phase Retrieval," *J. Opt. Soc. Am. A. Opt. Image Sci. Vis.* **21**:828–831.
49. D. A. Agard, Y. Hiraoka, P. Shaw and J. W. Sedat, (1989) "Fluorescence Microscopy in Three Dimensions," *Methods Cell Biol.* **30**:353–377.
50. R. Oldenbourg, S. Inoué, R. Tiberio, A. Stemmer, G. Mei and M. Skvarla, (1996) Standard Test Targets for High Resolution Light Microscopy. In: *Nanofabrication and Biosystems: Integrating Material Science, Engineering and Biology* (eds. H. C. Hoch, L. W. Jelinsky and H. Craighead). Cambridge University Press, Cambridge, England.
51. E. M. Chamot and C. W. Mason, (1958) *Handbook of Chemical Microscopy*, John Wiley & Sons, New York.
52. B. Kachar, (1985) "Asymmetric Illumination Contrast: A Method of Image Formation for Video Microscopy," *Science* **227**:766–768.
53. N. Streibl, (1984) "Phase Imaging by the Transport-Equation of Intensity," *Opt. Commun.* **49**:6–10.

54. C. J. R. Sheppard, (2002) "Three-Dimensional Phase Imaging with the Intensity Transport Equation," *Appl. Opt.* **41**:5951–5955.
55. E. D. Barone-Nugent, A. Barty and K. A. Nugent, (2002) "Quantitative Phase-Amplitude Microscopy I: Optical Microscopy," *J. Microsc.* **206**:194–203.
56. D. Paganin, A. Barty, P. J. McMahon and K. A. Nugent, (2004) "Quantitative Phase-Amplitude Microscopy. III. The Effects of Noise," *J. Microsc.* **214**:51–61.
57. K. A. Nugent, D. Paganin and A. Barty, (2006) Phase Determination of a Radiation Wave Field. In: *U.S. Patent, Number 7,039,553*. University of Melbourne, Australia, USA.
58. C. S. Izzard and L. R. Lochner, (1980) "Formation of Cell-to-Substrate Contacts During Fibroblast Motility: An Interference-Reflection Study," *J. Cell Sci.* **42**:81–116.
59. N. Noda and S. Kamimura, (2008) "A New Microscope Optics for Laser Dark-Field Illumination Applied to High Precision Two Dimensional Measurement of Specimen Displacement," *Rev. Sci. Instrum.* **79**:023704.
60. F. Zernike, (1958) The Wave Theory of Microscopic Image Formation. In: *Concepts of Classical Optics* (ed. J. Strong). W.H. Freeman and Co., San Francisco.
61. A. H. Bennett, H. Osterberg, H. Jupnik and O. W. Richards, (1951) *Phase Microscopy, Principles and Applications*, John Wiley & Sons, Inc., New York.
62. M. Pluta, (1989b) "Simplified Polanret System for Microscopy," *Appl. Opt.* **28**:1453–1466.
63. R. Hoffman and L. Gross, (1975) "Modulation Contrast Microscopy," *Appl. Opt.* **14**:1169–1176.
64. G. W. Ellis, (1978) Advances in Visualization of Mitosis In Vivo. In: *Cell Reproduction: In Honor of Daniel Mazia*, (eds. E. Dirksen, D. Prescott and C. F. Fox). Academic Press, New York, pp. 465–476.
65. G. W. Ellis, (1988) Scanned Aperture Light Microscopy," *Proc. 46th Annual Meeting of the Electron Microscopy Society of America*, 48–49.
66. J. Dyson, (1961) "Instrument Classification and Applications," In: *The Encyclopedia of Microscopy* (ed. G.L. Clark) Reinhold Pub. Corp., New York, 412–420
67. C. J. Koester, (1961) "Theory and Techniques," In: *The Encyclopedia of Microscopy* (ed. G.L. Clark) Reinhold Pub. Corp., New York, 420–434
68. N. H. Hartshorne and A. Stuart, (1960) *Crystals and the Polarising Microscope: A Handbook for Chemists and Others*, Arnold, London.
69. G. A. Dunn, (1998) "Transmitted-Light Interference Microscopy: A Technique Born before Its Time," *Proc. RMS* **33**:189–196.
70. W. P. Linnik, (1933) "Apparatus for Interferometric Study of Reflective Specimens with a Microscope ("Microinterferometer")," *C. R. Acad. Sci. USSR* **1**:18–23 (in Russian and German).
71. A. A. Lebedeff, (1930) "Polarization Interferometer and Its Applications," *Rev. Opt.* **9**:385.
72. G. V. Rozenberg, (1953) "Interference Microscopy," *Uspekhi Fizicheskikh Nauk* **50**:271–302 (in Russian).
73. M. Françon, (1964) "Polarization Interference Microscopes," *Appl. Opt.* **3**:1033–1036.
74. M. J. Jamin, (1868) "Sur un réfracteur différentiel pour la lumière polarisée," *C. R. Acad. Sci. (Paris)* **67**:814.
75. F. H. Smith, (1952) Interference Microscope. In: *U.S. Patent, Number 2,601,175*. Francis Hugh Smith, USA.
76. F. H. Smith, (1955) "Microscopic Interferometry," *Research (London)*, **8**:385–395.
77. G. Nomarski, (1960) Interferential Polarizing Device for Study of Phase Objects. In: *U.S. Patent, Number 2,924,142*. Centre National de la Recherche Scientifique, Paris, France, USA.
78. R. D. Allen, G. B. David and G. Nomarski, (1969) "The Zeiss-Nomarski Differential Interference Equipment for Transmitted Light Microscopy," *Zeitschrift für wissenschaftliche Mikroskopie* **69**:193–221.
79. M. Shribak and S. Inoue, (2006) "Orientation-Independent Differential Interference Contrast Microscopy," *Appl. Opt.* **45**:460–469.
80. C. J. Cogswell and C. J. R. Sheppard, (1992) "Confocal Differential Interference Contrast (DIC) Microscopy: Including a Theoretical Analysis of Conventional and Confocal DIC Imaging," *J. Microscopy* **165**:81–101.
81. C. Preza, D. L. Snyder and J. A. Conchello, (1999) "Theoretical Development and Experimental Evaluation of Imaging Models for Differential-Interference-Contrast Microscopy," *J. Opt. Soc. Am. A. Opt. Image Sci. Vis.* **16**:185–2199.

82. R. D. Allen, J. L. Travis, N. S. Allen and H. Yilmaz, (1981) "Video-Enhanced Contrast Polarization (AVEC-POL) Microscopy: A New Method Applied to the Detection of Birefringence in the Motile Reticulopodial Network *Allogromia laticollaris*," *Cell Motil.* **1**:275–289.
83. E. D. Salmon and P. T. Tran, (1998) "High-Resolution Video-Enhanced Differential Interference Contrast (VE-DIC) Light Microscopy," *Methods Cell Biol.*, **56**:153–184.
84. H. Ishiwata, M. Itoh and T. Yatagai, (1996) "Retardation-Modulated Differential Interference Microscope and its Application to 3D Shape Measurement," *Proc.* **2873**:21–24.
85. G. Holzwarth, S. C. Webb, D. J. Kubinski and N. S. Allen, (1997) "Improving DIC Microscopy with Polarization Modulation," *J. Microsc.* **188**:249–254.
86. G. M. Holzwarth, D. B. Hill and E. B. McLaughlin, (2000) "Polarization-Modulated Differential-Interference Contrast Microscopy with a Variable Retarder," *Appl. Opt.* **39**:6288–6294.
87. H. Ishiwata, M. Itoh and T. Yatagai, (2006) "A New Method of Three-Dimensional Measurement by Differential Interference Contrast Microscope," *Opt. Commun.* **260**:117–126.
88. R. P. Danz, A. Dietrich, C. Soell, Hoyer and M. Wager, (2006) Arrangement and Method for Polarization-optical Interference Contrast. In: *U.S. Patent, Number 7,046,436*. Carl Zeiss Jena GmbH (Jena, DE).
89. B. Heise, A. Sonnleitner and E. P. Klement, (2005) "DIC Image Reconstruction on Large Cell Scans," *Microsc. Res. Tech.* **66**:312–320.
90. C. Preza, (2000) "Rotational-Diversity Phase Estimation from Differential-Interference—Contrast Microscopy Images," *J. Opt. Soc. Am. A-Opt. Image Sci. Vis.* **17**:415–424.
91. M. R. Arnison, K. G. Larkin, C. J. R. Sheppard, N. I. Smith and C. J. Cogswell, (2004) "Linear Phase Imaging Using Differential Interference Contrast Microscopy," *J. Microsc.-Oxford*, **214**:7–12.
92. F. Kagalwala and T. Kanade, (2003) "Reconstructing Specimens Using DIC Microscope Images," *IEEE Transactions on Systems Man and Cybernetics Part B-Cybernetics* **33**:728–737.
93. N. Axelrod, A. Radko, A. Lewis and N. Ben-Yosef, (2004) "Topographic Profiling and Refractive-Index Analysis by Use of Differential Interference Contrast with Bright-Field Intensity and Atomic Force Imaging," *Appl. Opt.* **43**:2272–2284.
94. M. Shribak, J. LaFountain, D. Biggs and S. Inoue, (2008) "Orientation-Independent Differential Interference Contrast Microscopy and Its Combination with an Orientation-Independent Polarization System," *J Biomed. Opt.* **13**:014011.
95. J. Dyson, (1950) "An Interferometer Microscope," *Proc. Roy. Soc. London. Series A, Mathematical and Physical Sciences* **204**:170–187.
96. G. Delaunay, (1953) "Microscope interférentiel A. Mirau pour la mesure du fini des surfaces," *Rev. Optique* **32**:610–614.
97. G. W. Ellis, (1966) "Holomicrography: Transformation of Image During Reconstruction of a Posteriori," *Science* **154**:1195–1197.
98. P. Marquet, B. Rappaz, P. J. Magistretti, E. Cuche, Y. Emery, T. Colomb and C. Depeursing, (2005) "Digital Holographic Microscopy: A Noninvasive Contrast Imaging Technique Allowing Quantitative Visualization of Living Cells with Subwavelength Axial Accuracy," *Opt. Lett.* **30**:468–470.
99. B. Kemper, D. Carl, J. Schneckeburger, I. Bredebusch, M. Schafer, W. Domschke and G. von Bally, (2006) "Investigation of Living Pancreas Tumor Cells by Digital Holographic Microscopy," *J. Biomed. Opt.* **11**.
100. A. Stern and B. Lavid, (2007) "Theoretical Analysis of Three-Dimensional Imaging and Recognition of Micro-Organisms with a Single-Exposure On-line Holographic Microscope," *J. Opt. Soc. Am. A-Opt. Image Sci. Vis.* **24**:163–168.
101. A. Stadelmaier and J. H. Massig, (2000) "Compensation of Lens Aberrations in Digital Holography," *Opt. Lett.* **25**:1630–1632.
102. S. S. Kou and C. J. R. Sheppard, (2007) "Imaging in Digital Holographic Microscopy," *Opt. Exp.* **15**:13640–13648.
103. Y. Kuznetsova, A. Neumann and S. R. J. Brueck, (2007) "Imaging Interferometric Microscopy—Approaching the Linear Systems Limits of Optical Resolution," *Opt. Exp.* **15**:6651–6663.
104. C. J. R. Sheppard and M. Roy, (2007) Low-Coherence Interference Microscopy. In: *Optical Imaging and Microscopy* (eds. P. Török and F. J. Kao). 2d ed. Springer-Verlag, Berlin, Heidelberg, New York.

105. A. M. Zysk and S. A. Boppart, (2007) Optical Coherence Tomography. In: *Optical Imaging and Microscopy* (eds. P. Török and F. J. Kao). 2d ed. Springer-Verlag, Berlin, Heidelberg, New York.
106. M. Wojtkowski, R. Leitgeb, A. Kowalczyk, T. Bajraszewski and A. F. Fercher, (2002) "In Vivo Human Retinal Imaging by Fourier Domain Optical Coherence Tomography," *J. Biomed. Opt.* **7**:457–463.
107. S. R. Chinn, E. A. Swanson and J. G. Fujimoto, (1997) "Optical Coherence Tomography Using a Frequency-Tunable Optical Source," *Opt. Lett.* **22**:340–342.
108. F. Lexer, C. K. Hitznerberger, A. F. Fercher and M. Kulhavy, (1997) "Wavelength-Tuning Interferometry of Intraocular Distances," *Appl. Opt.* **36**:6548–6553.
109. V. V. Tuchin, L. V. Wang and D. A. Zimnyakov, (2006) *Optical Polarization in Biomedical Applications*, Springer-Verlag, Berlin, Heidelberg, New York.
110. J. A. Izatt, M. R. Hee, G. M. Owen, E. A. Swanson and J. G. Fujimoto, (1994) "Optical Coherence Microscopy in Scattering Media," *Opt. Lett.* **19**:590–592.
111. B. M. Hoeling, A. D. Fernandez, R. C. Haskell, E. Huang, W. R. Myers, D. C. Petersen, S. E. Ungersma, R. Y. Wang, M. E. Williams and S. E. Fraser, (2000) "An Optical Coherence Microscope for 3-Dimensional Imaging in Developmental Biology," *Opt. Exp.* **6**:136–146.
112. S. Inoué, (1952) "Studies on Depolarization of Light at Microscope Lens Surfaces. I. The Origin of Stray Light by Rotation at the Lens Surfaces," *Exp. Cell Res.* **3**:199–208.
113. S. Inoué and H. Kubota, (1958) "Diffraction Anomaly in Polarizing Microscopes," *Nature* **182**:1725–1726.
114. H. Kubota and S. Inoué, (1959) "Diffraction Images in the Polarizing Microscope," *J. Opt. Soc. Am.* **49**:191–198.
115. S. Inoué and W. L. Hyde, (1957) "Studies on Depolarization of Light at Microscope Lens Surfaces II. The Simultaneous Realization of High Resolution and High Sensitivity with the Polarizing Microscope," *J. Biophys. Biochem. Cytol.* **3**:831–838.
116. M. Shribak, S. Inoué and R. Oldenbourg, (2002) "Polarization Aberrations Caused by Differential Transmission and Phase Shift in High NA Lenses: Theory, Measurement and Rectification," *Opt. Eng.* **41**:943–954.
117. S. Inoué and H. Sato, (1966) Deoxyribonucleic acid Arrangement in Living Sperm. In: *Molecular Architecture in Cell Physiology* (eds. T. Hayashi and A. G. Szent-Gyorgyi). Prentice Hall, Englewood Cliffs, NJ.
118. H. G. Jerrard, (1948) "Optical Compensators for Measurement of Elliptical Polarization," *J. Opt. Soc. Am.* **38**:35–59.
119. R. Oldenbourg, (1999) "Polarized Light Microscopy of Spindles," *Methods Cell Biol.* **61**:175–208.
120. H. G. Jerrard, (1954) Transmission of Light through Birefringent and Optically Active Media: The Poincaré sphere," *J. Opt. Soc. Am.* **44**:634–640.
121. A. M. Glazer, J. G. Lewis and W. Kaminsky, (1996) "An Automatic Optical Imaging System for Birefringent Media," *Proc. R. Soc. London A* **452**:2751–2765.
122. R. D. Allen, J. Brault and R. D. Moore, (1963) "A New Method of Polarization Microscopic Analysis I. Scanning with a Birefringence Detection System," *J. Cell Biol.* **18**:223–235.
123. J. R. Kuhn, Z. Wu and M. Poenie, (2001) "Modulated Polarization Microscopy: A Promising New Approach to Visualizing Cytoskeletal Dynamics in Living Cells," *Biophys. J.* **80**:972–985.
124. R. Oldenbourg and G. Mei, (1995) "New Polarized Light Microscope with Precision Universal Compensator," *J. Microsc.* **180**:140–147.
125. M. Shribak and R. Oldenbourg, (2003a) "Techniques for Fast and Sensitive Measurements of Two-Dimensional Birefringence Distributions," *Appl. Opt.* **42**:3009–3017.
126. R. Oldenbourg, (2005) Polarization Microscopy with the LC-PolScope. In: *Live Cell Imaging: A Laboratory Manual* (eds. R. D. Goldman and D. L. Spector). Cold Spring Harbor Laboratory Press, Cold Spring Harbor, NY.
127. R. Oldenbourg, (1991) "Analysis of Edge Birefringence," *Biophys. J.* **60**:629–641.
128. F. D. Bloss, (1981) *The Spindle Stage Principles and Practice*, Cambridge University Press, Cambridge.
129. W. Kaminsky and A. M. Glazer, (1996) "Measurement of Optical Rotation in Crystals," *Ferroelectrics* **183**:133–141.
130. L. A. Pajdzik and A. M. Glazer, (2006) "Three-Dimensional Birefringence Imaging with a Microscope Tilting-Stage. I. Uniaxial Crystals," *J. Appl. Crystallogr.* **39**:326–337.

131. M. Shribak and R. Oldenbourg, (2004) "Mapping Polymer Birefringence in Three Dimensions Using a Polarizing Microscope with Oblique Illumination," *SPIE Proc. (Proc. Biophotonics Micro- and Nano-Imaging)* **5462**:57–67.
132. D. L. Taylor, M. Nederlof, F. Lanni and A. S. Waggoner, (1992) "The New Vision of Light Microscopy," *Am. Sci.* **80**:322–335.
133. R. Y. Tsien, (1989) Fluorescent Probes of Cell Signaling. In: *Annu. Rev. Neurosci.* (eds. W. M. Cowas, E. M. Shooter, C. F. Stevens, and R. F. Thompson). Annual Reviews, Inc., Palo Alto.
134. R. Y. Tsien, (1998) "The Green Fluorescent Protein," *Annu. Rev. Biochem.* **67**:509–544.
135. J. W. Lichtman and J. A. Conchello, (2005) "Fluorescence Microscopy," *Nat. Methods* **2**:910–919.
136. R. Neher and E. Neher, (2004) "Optimizing Imaging Parameters for the Separation of Multiple Labels in a Fluorescence Image," *J. Microsc.* **213**:46–62.
137. Y. Garini, I. T. Young and G. McNamara, (2006) Spectral Imaging: Principles and Applications," *Cytometry Part A* **69**:735–747.
138. M. Minsky, (1957) Microscopy Apparatus. In: *U.S. Patent #3013467* (ed. U. S. P. a. T. Office). USA.
139. S. Inoué, (1990) Foundations of Confocal Scanned Imaging in Light Microscopy. In: *Handbook of Biological Confocal Microscopy* (ed. J. B. Pawley). Plenum Publ. Corp., New York.
140. G. S. Kino, (1990) Intermediate Optics in Nipkow Disk Microscopes. In: *Handbook of Biological Confocal Microscopy* (ed. J. B. Pawley). Plenum Press, New York.
141. M. Petráň, M. Hadravsky, D. Egger and R. Galambos, (1968) "Tandem-Scanning Reflected-Light Microscope," *J. Opt. Soc. Am.* **58**:661–664.
142. S. Inoue and T. Inoue, (2002) "Direct-View High-Speed Confocal Scanner: The CSU-10," *Methods Cell Biol.* **70**:87–127.
143. E. Wang, C. M. Babbey and K. W. Dunn, (2005) "Performance Comparison between the High-Speed Yokogawa Spinning Disc Confocal System and Single-Point Scanning Confocal Systems," *J. Microsc.* **218**:148–159.
144. W. A. Carrington, R. M. Lynch, E. D. W. Moore, G. Isenberg, K. E. Fogarty and F. S. Fay, (1995) "Superresolution Three-Dimensional Images of Fluorescence in Cells with Minimal Light Exposure," *Science* **268**:1483–1487.
145. J. A. Conchello and J. W. Lichtman, (2005) "Optical Sectioning Microscopy," *Nat. Methods* **2**:920–931.
146. M. A. Neil, R. Juskaitis and T. Wilson, (1997) "Method of Obtaining Optical Sectioning by Using Structured Light in a Conventional Microscope," *Opt. Lett.* **22**:1905–1907.
147. C. Ventalon and J. Mertz, (2005) "Quasi-Confocal Fluorescence Sectioning with Dynamic Speckle Illumination," *Opt. Lett.* **30**:3350–3352.
148. C. Ventalon and J. Mertz, (2006) "Dynamic Speckle Illumination Microscopy with Translated versus Randomized Speckle Patterns," *Opt. Exp.* **14**:7198–7209.
149. M. G. Gustafsson, (2000) "Surpassing the Lateral Resolution Limit by a Factor of Two Using Structured Illumination Microscopy," *J. Microsc.* **198**:82–87.
150. M. G. Gustafsson, L. Shao, P. M. Carlton, C. J. Wang, I. N. Golubovskaya, W. Z. Cande, D. A. Agard and J. W. Sedat, (2008) "Three-Dimensional Resolution Doubling in Wide-Field Fluorescence Microscopy by Structured Illumination," *Biophys. J.* **94**:4957–4970.
151. R. Heintzmann, T. M. Jovin and C. Cremer, (2002) "Saturated Patterned Excitation Microscopy—a Concept for Optical Resolution Improvement," *J. Opt. Soc. Am. A-Opt. Image Sci. Vis.* **19**:1599–1609.
152. M. G. Gustafsson, (2005) "Nonlinear Structured-Illumination Microscopy: Wide-Field Fluorescence Imaging with Theoretically Unlimited Resolution," *Proc. Natl. Acad. Sci. U S A* **102**:13081–13086.
153. R. Ng, M. Levoy, M. Bredif, G. Duval, M. Horowitz and P. Hanrahan, (2005) Light Field Photography with a Hand-Held Plenoptic Camera. *Stanford Tech. Report, CTSR 2005-02*.
154. M. Shribak and R. Oldenbourg, (2003b) "Three-Dimensional Birefringence Distribution in Reconstituted Asters of *Spisula* Oocytes Revealed by Scanned Aperture Polarized Light Microscopy," *Biol. Bull.* **205**:194–195.
155. R. E. Stephens, (1965) "Analysis of Muscle Contraction by Ultraviolet Microbeam Disruption of Sarcomere Structure," *J. Cell Biol.* **25**:129–139.
156. M. W. Berns, (1974) *Biological Microirradiation, Classical and Laser Sources*, Prentice-Hall, Englewood Cliffs.

157. D. E. Koppel, D. Axelrod, J. Schlessinger, E. L. Elson and W. W. Webb, (1976) "Dynamics of Fluorescence Marker Concentration as a Probe of Mobility," *Biophys. J.* **16**:1315–1329.
158. H. G. Kapitza, G. McGregor and K. A. Jacobson, (1985) "Direct Measurement of Lateral Transport in Membranes by Using Time-Resolved Spatial Photometry," *Proc. Natl. Acad. Sci. (USA)* **82**:4122–4126.
159. M. W. Berns, J. Aist, J. Edwards, K. Strahs, J. Girton, P. McNeill, J. B. Rattner, et al., (1981) "Laser Microsurgery in Cell and Developmental Biology," *Science* **213**:505–513.
160. V. Magidson, J. Loncarek, P. Hergert, C. L. Rieder and A. Khodjakov, (2007) Laser Microsurgery in the GFP Era: A Cell Biologist's Perspective," *Methods Cell Biol.* **82**:239–266.
161. C. Lutz, T. S. Otis, V. Desars, S. Charpak, D. A. Digregorio and V. Emiliani, (2008) "Holographic Photolysis of Caged Neurotransmitters," *Nat. Methods* **5**:821–827.
162. J. H. Kaplan and G. C. Ellis-Davies, (1988) "Photolabile Chelators for the Rapid Photorelease of Divalent Cations," *Proc. Natl. Acad. Sci. (USA)* **85**:6571–6575.
163. J. A. Dantzig, M. G. Hibberd, D. R. Trentham and Y. E. Goldman, (1991) Cross-Bridge Kinetics in the Presence of MgADP Investigated by Photolysis of Caged ATP in Rabbit Psoas Muscle Fibres," *J. Physiol. (London)* **432**:639–680.
164. T. J. Mitchison and E. D. Salmon, (1992) "Poleward Kinetochore Fiber Movement Occurs during Both Metaphase and Anaphase—A in Newt Lung Cell Mitosis," *J. Cell Biol.* **119**:569–582.
165. A. Ashkin, J. M. Dziedzic, J. E. Bjorkholm and S. Chu, (1986) "Observation of a Single-Beam Gradient Force Optical Trap for Dielectric Particles," *Opt. Lett.* **11**:288–290.
166. K. Svoboda and S. M. Block, (1994) "Biological Applications of Optical Forces," *Annu. Rev. Biophys. Biomol. Struct.* **23**:247–285.
167. S. M. Block, (1990) "Optical Tweezers: A New Tool for Biophysics," In: *Noninvasive Techniques in Cell Biology* (eds. J. K. Foskett and S. Grinstein). Wiley-Liss, New York.
168. J. R. Moffitt, Y. R. Chemla, S. B. Smith and C. Bustamante, (2008) "Recent Advances in Optical Tweezers," *Annu. Rev. Biochem.* **77**:205–228.